UNIVERSITY OF CALIFORNIA
Los Angeles

Very-High-Energy Astrophysical Processes in the Cygnus Region of the Milky Way

A dissertation submitted in partial satisfaction
of the requirements for the degree
Doctor of Philosophy in Physics

by

Alexis G. Popkow

2017

ABSTRACT OF THE DISSERTATION

Very-High-Energy Astrophysical Processes in the Cygnus Region of the Milky Way

by

Alexis G. Popkow
Doctor of Philosophy in Physics
University of California, Los Angeles, 2017
Professor Rene A. Ong, Chair

Very-high-energy (VHE) gamma-ray astronomy can provide insight in to the origin of cosmic rays. The Cygnus arm of the Galaxy is a well studied region and has been shown to have active sources of particle acceleration. VERITAS (Very Energetic Radiation Imaging Telescope Array System) is an array of four 12 meter diameter imaging atmospheric Cherenkov telescopes located at the Fred Lawrence Whipple Observatory in southern Arizona. From 2007 through 2012 VERITAS observed the Cygnus region for nearly 300 hours from 67° to 82° in Galactic longitude and from -1° to 4° in Galactic latitude. The survey and followup observations detected four sources: VER J2031+415, VER J2019+407, VER J2016+317, and VER J2019+368. The *Fermi* Large Area Telescope (*Fermi*-LAT) is a satellite gamma-ray telescope operating in the high-energy gamma-ray regime. The emission detected by the *Fermi*-LAT can provide insight into the nature of these sources and guide targeted followup observations in the region. We have reanalyzed the VERITAS data with updated VERITAS analysis and completed an analysis of over seven years of *Fermi*-LAT data in the region. We have discovered *Fermi*-LAT emission associated with VER J2031+415 strengthening its interpretation as a pulsar wind nebula, the SNR nature of VER J2019+407 has been confirmed by this study, and VER J2016+317 has been confirmed to be associated with the pulsar wind nebula CTB 87 rather than with a blazar source located at the same position. The Cygnus region is observed to be a particularly bright region of the Galaxy with both very-high-energy and high-energy gamma-ray experiments. These results motivate continued study of the region with VERITAS, as well as with current and future experiments such

as HAWC and CTA.

The dissertation of Alexis G. Popkow is approved.

John B. Garnett

Mark R. Morris

Rene A. Ong, Committee Chair

University of California, Los Angeles

2017

For my mom

TABLE OF CONTENTS

List of Figures

List of Tables

ACKNOWLEDGMENTS

I would first like to thank my adviser Prof. Rene Ong for guiding me to this thesis and gave me the opportunity to be involved with the VERITAS collaboration. He provided the support necessary for my travel and professional development. He furthermore helped to guide this thesis to its completion.

Thank you to the high energy group at UCLA who helped at all stages and with many aspects of my research: Tim Arlen and Julien Rouselle for their support with getting started with the *Fermi* and Eventdisplay analysis on the UCLA computers, Amanda and Pratik for giving insight into the early , Isaac Mognet for supporting gamma-ray astronomy outreach at EYU, Taylor Aune for helping with the numerous analysis crosschecks. Ralph Bird was instrumental to pushing the completion of the work in this thesis, got me going with the fermipy analysis and using Python as an analysis tool, and has provided invaluable guidance as we work on the paper.

I would like to thank many supportive members of the VERITAS collaboration: Maria Krause (for being a great collaborator), Gernot Meier (for support with the Eventdisplay analysis package), members of the Galactic science VERITAS group and Pascal Fortin (for helping out on every observing shift). A special thanks to Reshmi Mukherjee and Jamie Holder for their support in helping me embark on the next step of my career with countless recommendation letters.

Thank you to the Physics and Astronomy department at UCLA, for providing a great support network of staff and fellow students: Breann, Fred, Shane, Nate, Eric, Siyi, Robin, Thomas, Tom, Bijan, Ivan, Josh, Kevin, Billy, Anna and Emily. And especially Sean Litsey, thank you for reading and improving my thesis and supporting me through the long job search.

I appreciate the support of my family: my mom, my dad, my step-mom, my sisters, and my brother. Home cooked meals and trips to Disneyland gave me much needed relaxation time. Thank you mom for helping me feel like I can achieve anything.

VITA

2010	B.A. (Physics) and B.A. (Astrophysics), University of California, Berkeley.
2010-2012	Teaching Assistant, Physics and Astronomy Department, UCLA.
2011-2016	Research Assistant, Physics and Astronomy Department, UCLA.
2012	M.S. (Physics), UCLA.

PUBLICATIONS AND PRESENTATIONS

Alexis Popkow for the VERITAS Collaboration, "The VERITAS Survey of the Cygnus Region of the Galaxy", (Talk), International Cosmic Ray Conference (ICRC), The Hague, The Netherlands, August 2015

Alexis Popkow for the VERITAS Collaboration, "The VERITAS Survey of the Cygnus Region of the Galaxy", (poster), American Astronomical Society, High Energy Astro- physics Division Meeting, Chicago, Illinois, August 2014

Alexis Popkow for the VERITAS Collaboration, "The VERITAS Sky Survey Results and Futrue Plans", (poster), American Astronomical Society Meeting, Long Beach, California, January 2013

CHAPTER 1

Introduction

Cosmic rays are energetic particles (protons, electrons, nuclei, and photons) from space. Understanding the mechanisms of their origin is an active topic in physics and astrophysics research. Gamma-ray studies of highly energetic sources can reveal details of processes at work in cosmic-ray acceleration. Within our Galaxy, the Cygnus region is rich in HE and VHE gamma-ray radiation. This dissertation presents work using the VERITAS and *Fermi*-LAT telescopes to study the gamma-ray sources in the Cygnus region and to understand their connection to cosmic-ray acceleration.

1.1 Very-High-Energy and High-Energy Gamma-Ray Astronomy

Cosmic rays were first discovered in 1912 by Victor Hess using an electroscope on a series of balloon flights [1]. Those experiments determined that the high-energy particles continuously measured in experiments on the ground originated in outer space. Since that time, our understanding of what cosmic rays are has expanded considerably. Cosmic rays are primarily protons (about 90%) and alpha particles (^{4}He nuclei), with contributions from electrons, positrons, and heavier nuclei. Their angular distribution is nearly isotropic, and their energy spectrum follows a power-law distribution spanning nearly twelve orders of magnitude; see Figure 1.1. There are two features to their power-law spectrum: the *knee* (at about 10 PeV, or 10×10^{15} eV), where the spectrum steepens and the *ankle* (at a few 10^{18} eV, or about 1 EeV), where the spectrum flattens. It is believed that most of the cosmic rays with energies up to the *knee* are accelerated by sources within the Milky Way Galaxy. At energies beyond the *knee*, cosmic rays are thought to be accelerated in extragalactic sources such as active galactic nuclei (AGN).

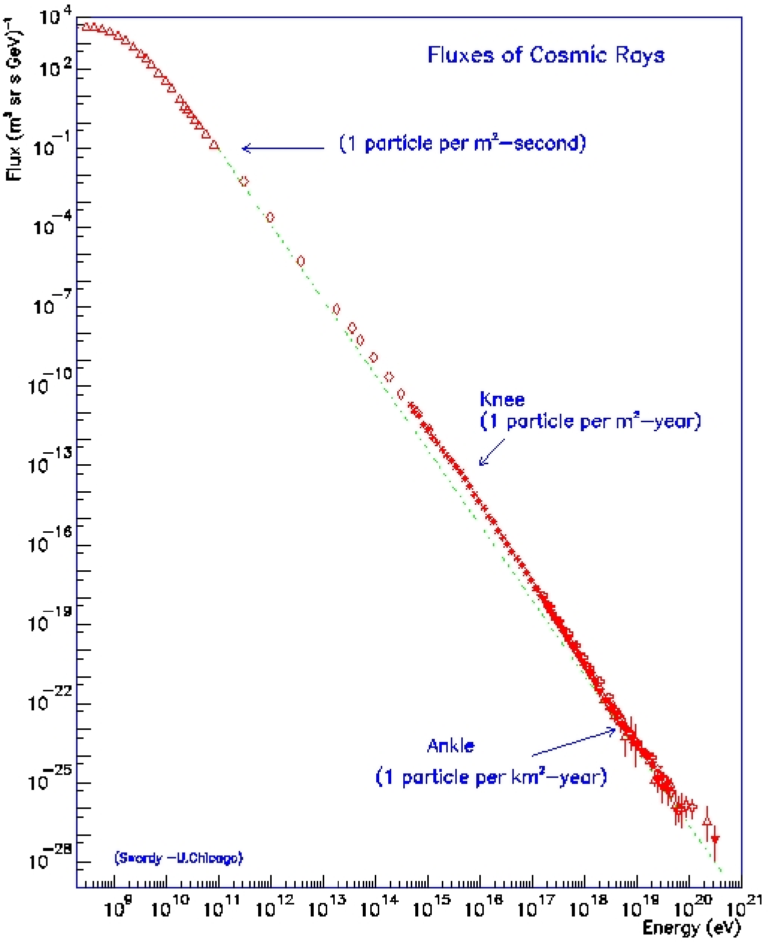

Figure 1.1: The measured cosmic-ray spectrum [2], which spans over twelve orders of magnitude in energy. Particles up to the *knee* are thought to be accelerated by sources within the Galaxy, and while particles up to the *ankle* and beyond are thought to be accelerated by extragalactic sources, such as active galaxies. This is discussed in further detail in Chapter 2.

The details by which astrophysical sources accelerate these particles are not yet fully understood, but there has been significant progress in understanding the details of cosmic-ray acceleration in recent years. In particular, the majority of cosmic rays are believed to be accelerated in supernova remnants (SNRs). SNRs are thought to primarily accelerate particles within the interaction of the shock front with material in our Galaxy (such as gas clouds, interstellar material, or even other remnants). There have been recent astrophysical clues that protons are accelerated in SNRs [3]. Any directional information from charged cosmic-ray particles is lost because they get deflected by Galactic magnetic fields. We must use gamma rays (or neutrinos), which point back to their sources, for observations to study the acceleration processes that create cosmic rays.

The primary sources that are believed to contribute to the Galactic cosmic-ray nuclei population are SNRs. Acceleration in pulsar wind nebulae (PWNe) is thought to contribute to the cosmic-ray electron spectrum [4]. These sources produce gamma rays with energies greater than 10^{12} eV (or 1 TeV); for comparison, optical astronomy is typically undertaken using photons in the eV energy range. High-energy (HE) gamma-ray studies are undertaken at energies greater than about 100 MeV and very-high-energy (VHE) gamma-ray studies at energies greater than about 100 GeV.

Methods of gamma-ray production depend on the particles being accelerated by astrophysical sources. In the case of proton acceleration, those protons interact with material in the Galaxy to create pions, including neutral neutral pions (π^0), which immediately decay into gamma rays. When electrons are the primary accelerated particle, they can create gamma rays through inverse Compton scattering and bremsstrahlung radiation.

Other classes of gamma-ray sources in the Galaxy can also be used to probe the acceleration of high-energy particles. These include: binary systems (particularly high-mass x-ray binaries), star forming regions, and unidentified sources that could be identified to be either of these other source types, or provide a new class of Galactic source for TeV astronomy. Searches for VHE gamma-ray sources in our Galaxy have proven to be fruitful over the last decade, with a wide variety of sources detected. Further detail about cosmic rays is provided in Chapter 2, and details about sources in the Cygnus region of the Galaxy are provided in Chapter 3

1.2 Gamma-ray Observatories

Gamma rays, along with other high-energy particles, interact with our atmosphere when they reach Earth, primarily through pair production. These interactions result in air showers of particles (typically electrons and positrons with smaller contributions from muons, pions, and kaons), as well as visible-light Cherenkov radiation and radio emission. Therefore, the three primary ways of detecting astrophysical gamma rays are by: placing the detector in space in orbit above the atmosphere, detecting the Cherenkov light produced by the air showers, or directly detecting the particles of the air shower.

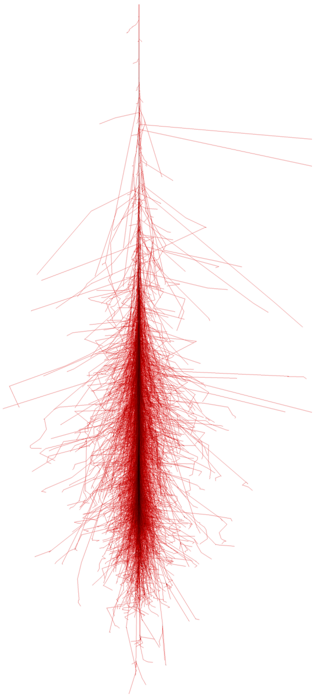

Figure 1.2: An example of a gamma-ray-initiated air shower from simulations. The red lines represent electrons and positrons. Image from [5], based on CORSIKA simulations [6].

HE gamma-ray studies are typically done in space and detect gamma rays with energies of 10^6–10^9 eV (MeV to GeV) through their interactions directly in the detector medium. The number of gamma rays from space decreases rapidly at higher energies due to their power-law spectrum. At TeV energies, a large collection area is needed to detect gamma rays. VHE gamma-ray studies are ground-based and detect gamma rays with energies of 100 GeV to 100 TeV, either by Cherenkov light or air-shower particle detection.

1.2.1 Space-Based Observatories

An early satellite designed to study gamma-ray sources was COS-B, launched in 1975 [7]. It observed gamma rays with energies of 50 MeV to 5 GeV for over 6 years and detected numerous sources, as well as the diffuse gamma-ray emission from the Milky Way. The

Energetic Gamma Ray Experiment Telescope (EGRET) [8] on the Compton Gamma-ray Observatory followed from 1991-2000; it confirmed the findings of COS-B while expanding the catalog of gamma-ray sources to over one hundred point sources.

The Large Area Telescope (LAT) is the primary instrument on the *Fermi Gamma-ray Space Telescope*; it was developed by an international collaboration. *Fermi* was launched by NASA in June 2008 and began observations in August 2008. The LAT images gamma rays with energies from 20 MeV to greater than 500 GeV. It primarily operates in all-sky observation mode, completing an orbit in about 96 minutes and covering the entire sky in two orbits. The LAT is a pair-conversion telescope, and the details of the instrument and its scientific goals are described in [9]. The five-year all-sky view of the sky with the *Fermi*-LAT is presented in Figure 1.3, and a quick overview of the instrument and the general data analysis procedure are presented in Chapter 6.

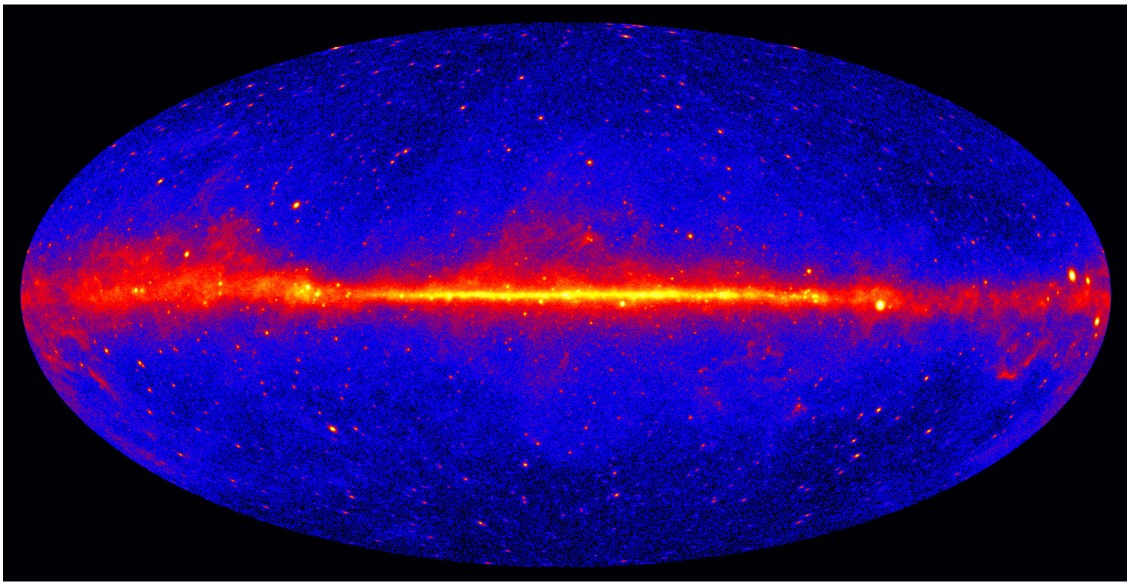

Figure 1.3: The *Fermi*-LAT all sky view from five years of observations of photons with energies greater than 1 GeV. Image Credit: NASA/DOE/Fermi LAT Collaboration.

1.2.2 Imaging Atmospheric Cherenkov Telescopes

For VHE gamma rays, the detector size of satellites is too small to effectively detect gamma rays, but the atmosphere provides a large collection area for gamma rays. One strategy to detect gamma rays at these higher energies is via imaging atmospheric Cherenkov telescopes (IACTs). These telescopes image Cherenkov light emitted by the particles in the air shower. The High-Energy Gamma-Ray Astronomy (HEGRA) experiment was a stereoscopic Cherenkov array which was operated in the Canary Islands from 1987 to 2002 [10]. Whipple was a single imaging atmospheric Cherenkov telescope that operated on Mt. Hopkins from 1968–2008 which detected the first VHE gamma-ray source, the Crab Nebula, in 1989 [11].

Currently there are three operating IACTs: VERITAS (Very Energetic Radiation Imaging Telescope Array System) in southern Arizona [12], MAGIC (Major Atmospheric Gamma Imaging Cherenkov) in the Canary Islands [13], and H.E.S.S. (High-Energy Stereoscopic System) in Namibia [14]. They each operate on clear, dark nights and have fruitfully observed a large range of TeV sources. The current (as of August 2016) catalog of TeV gamma-ray sources includes 179 sources [15]. Figure 1.4 shows the distribution of these sources, which include: 37 pulsar wind nebulae, 29 supernova remnants, 6 pulsars, and 9 binaries concentrated along the Galactic plane. There are 43 dark or unidentified sources; many of them are along the Galactic plane. Numerous active galaxies contribute away from the Galactic plane.

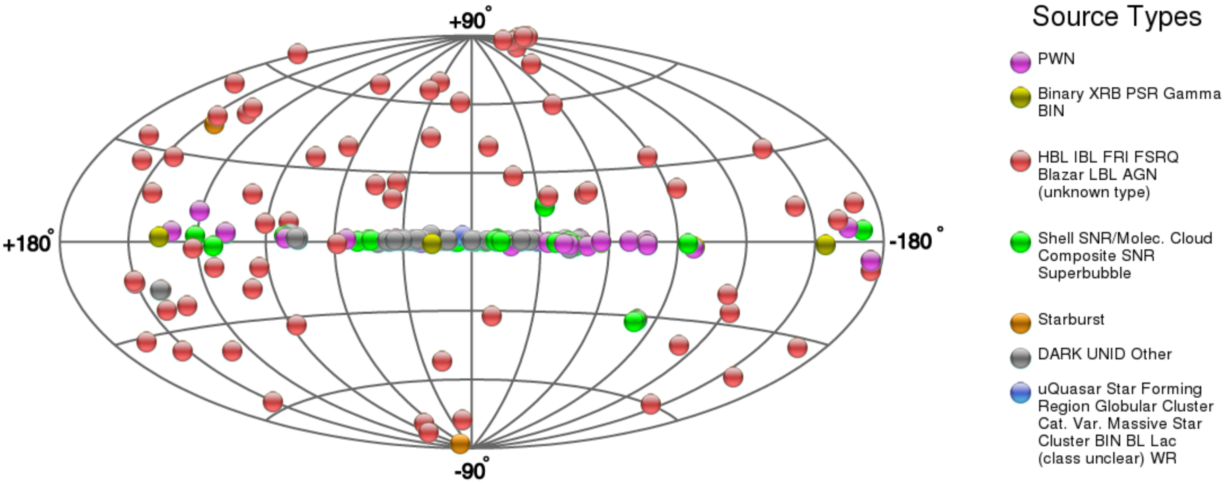

(a) TeVcat (b) Legend

Figure 1.4: Current (August 2016) known VHE sources, from TeVCat [15], plotted in Galactic coordinates. Clear from this map is the concentration of sources in the Galactic plane, including a large number of unidentified sources (gray). AGN, in red, dominate the source type outside of the Galaxy.

The successor to these experiments, CTA (the Cherenkov Telescope Array) [16] is being designed to improve over the current generation by a factor of 5–10 in sensitivity and to operate over an extended energy range. It will have a northern site in the Canary Islands and southern site in Chile. CTA is currently in the prototype stage of development, with pre-production expected to begin in 2017.

The IACT method is detailed in Chapter 4, and the VERITAS experiment and analysis procedure are discussed in Chapter 5

1.2.3 Air Shower Detectors

At the highest energies, the particles in the air shower resulting from the gamma ray interacting with the atmosphere reach the ground at high enough densities to be detected either directly, or through their Cherenkov radiation in water.

Direct Shower Detectors

Experiments can directly detect the particles of the air shower through a number of methods, such as using arrays of scintillators or resistive plate counters (RPCs). The ARGO-YBJ array in Tibet uses RPCs to continuously detect gamma rays with energies greater than about 100 GeV [17].

Water Cherenkov Observatories

Water Cherenkov observatories sample air-shower particles by measuring the Cherenkov light that results from the particles interacting in water. The first major water Cherenkov experiment was Milagro [18] (now disassembled); it operated from 1999 to 2008. Located in the mountains near Los Alamos, New Mexico, it was capable of detecting TeV gamma rays (with energies from 1 TeV to greater than 100 TeV) with a nearly 24 hour duty cycle. The High-Altitude Water Cherenkov (HAWC) gamma-ray observatory is a currently operating array of 300 water tanks near Puebla, Mexico [19]. It is capable of detecting gamma rays over a wider range of energies from 0.1–100 TeV with a 24 hour cycle, surveying two thirds of the sky each day. Full array observations began in 2015.

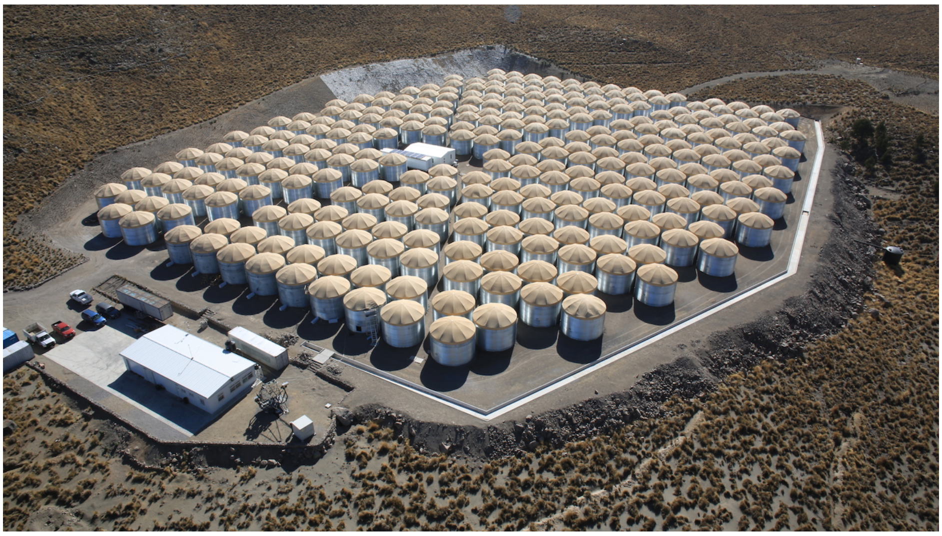

Figure 1.5: The HAWC Gamma-Ray Observatory site near Puebla, Mexico. Visible are the array of 300 water tanks.

Table 1.1: Comparison of the capabilities of current gamma-ray observatories. The *Fermi*-LAT represents a space-based mission, VERITAS an IACT, and HAWC a water Cherenkov array. Each method has its strengths and interesting studies can now be undertaken with their complementarity.

Experiment:	*Fermi*-LAT	VERITAS	HAWC
Energy Range:	20 MeV to $>$ 500 GeV	85 GeV to $>$ 35 TeV	100 GeV to 100 TeV
Energy Resolution:	$<$ 10%	15-50%	50%
Field-of-View:	$7875^{\circ 2}$	$10^{\circ 2}$	$6187^{\circ 2}$
Angular Resolution:	0.5° at 1 GeV	$<$ 0.1° at 1 TeV	0.5° at 1 TeV
Duty Cycle:	nearly 100%	$\sim$ 10%	nearly 100%
Effective Area:	7000 cm^2	$\sim$ 100,000 m^2	$>$ 10,000 m^2

Each method of detecting astrophysical sources at gamma-ray energies has its strengths. Space-based detectors are capable of large field-of-view observations, but at relatively low energies. IACTs are very sensitive with excellent angular resolution and energy resolution, but have limited observing windows. Water Cherenkov and air-shower arrays are less sensitive than IACTs, but are capable of wide field-of-view observations over a higher energy range. Complementary studies with each method would be ideal – the work presented here uses *Fermi*-LAT and VERITAS observations. The VERITAS collaboration has plans to follow up on interesting results from HAWC in the coming years.

1.3 The Cygnus Region

The Cygnus region of the Milky Way Galaxy is a uniquely bright region in non-thermal emission, and it is also much closer to observers on Earth than the Galactic center (about 1.7 kpc away versus about 8 kpc away). As a region with both active star formation and the largest clusters of the largest stars in our Galaxy, it has numerous sources of interest to HE and VHE gamma-ray studies. Further details about the Cygnus region and its sources in other wavelengths are detailed in Chapter 3.

1.3.1 HE View of Cygnus Region

A number of sources and a large amount of diffuse HE gamma-ray emission have been seen in the Cygnus region of the Galaxy. Beginning with the EGRET satellite, Cygnus has been a region of interest for further study. EGRET detected individual sources in the region with spectral signatures consistent with that expected from pulsars; these have since been confirmed by *Fermi*-LAT and radio pulsation searches. The superior resolution and sensitivity of *Fermi*-LAT have expanded the view of the region considerably. It is by far the brightest region seen by *Fermi*-LAT outside of the Galactic center.

1.3.2 VHE View of Cygnus Region

The Cygnus region is also where the first unidentified source of VHE emission was detected, TeV J2032+4130, by the HEGRA experiment. The Milagro experiment detected numerous areas bright in multi-TeV emission [18]. Since then, VERITAS observations have proven fruitful for detecting new sources, as well as for placing limits on VHE emission from sources that have HE spectral parameters that make them seem promising as potential VHE sources.

1.3.3 Observations of the Cygnus Region with VERITAS

From 2007 to 2009, VERITAS undertook a survey of the Cygnus region of the Galaxy. Previous analyses of the survey data hinted at new sources, which received follow-up observations through 2012. Initial studies undertaken with the survey and follow-up data have resulted in publications on four sources (including the known source TeV J2032+4126); these publications are detailed in Section 7.3. The survey observations, data set, an updated analysis, and results are presented in Chapter 7.

1.4 Dissertation Outline

This dissertation presents a study of the VHE and HE gamma-ray emission in the Cygnus region of the Galaxy using VERITAS and *Fermi*-LAT observations. The next chapter begins with an overview of the current knowledge of cosmic-ray acceleration in the Galaxy and the links to VHE gamma-ray sources. Chapter 3 provides an overview of the multiwavelength perspective of the Cygnus region. Chapter 4 introduces the atmospheric detection of cosmic rays, utilized by the VERITAS experiment (described in Chapter 5), and Chapter 6 discusses space-based gamma-ray astronomy with *Fermi*-LAT. The survey of the Cygnus region undertaken by VERITAS and the results of the VERITAS and *Fermi*-LAT analyses are presented in Chapter 7. Chapter 8 presents the interpretations and multiwavelength perspective, as well as summarizing the work of this dissertation.

CHAPTER 2

Cosmic Rays and the Production of Gamma Rays in the Galaxy

The mystery of the origin of the highly-energetic charged particles that constantly interact with our atmosphere is over a century old, and it is only recently that direct links to astrophysical objects have been verified.

This chapter begins with a quick overview of the current observations of cosmic rays in Section 2.1, including the details of cosmic-ray composition (Section 2.1.1), and Galactic cosmic ray production and confinement (Section 2.1.2). Then, Section 2.2 details the methods by which accelerated particles produce gamma rays. This chapter concludes with a look at recent gamma-ray observations, which have started to confirm the favored theories of cosmic ray acceleration in supernova remnants (SNRs) in Section 2.3.

2.1 Cosmic Rays

Cosmic rays follow a nearly power-law energy distribution over a wide energy range, as shown in Figure 1.1. For cosmic rays with less than about 1 GeV of energy, solar modulation affects the spectrum. At about 10^{15} eV (1 PeV) the spectrum steepens, this feature is referred to as the *knee*, and at 10^{18} eV the spectrum flattens at the *ankle*. Furthermore, there is evidence of a cutoff at 3×10^{19} eV, a possible sign of attenuation by cosmic microwave background photons in the process that causes the GZK limit [20]. At the highest energies, the distribution of cosmic-ray arrival directions suggests an extragalactic source population, such as active galactic nuclei, so this discussion of cosmic rays will focus on the energy range of those thought to be accelerated within the Galaxy (up to 10^{15} eV).

2.1.1 Cosmic Ray Composition

Cosmic rays are largely protons and nuclei, 98% of the total, with the next largest contribution from electrons, almost 2%. Of the protons and nuclei 90% are protons, 9% are helium (alpha particles), and 1% are heavier nuclei. There are further contributions from photons and neutrinos. The power-law energy spectrum holds for cosmic rays of varying composition, as seen in Figure 2.1. The cosmic-ray spectrum is flatter for primary particles, those that are accelerated at an astronomical source, than for the secondary species. Secondary species are largely produced by spallation of primary particle species off interstellar material.

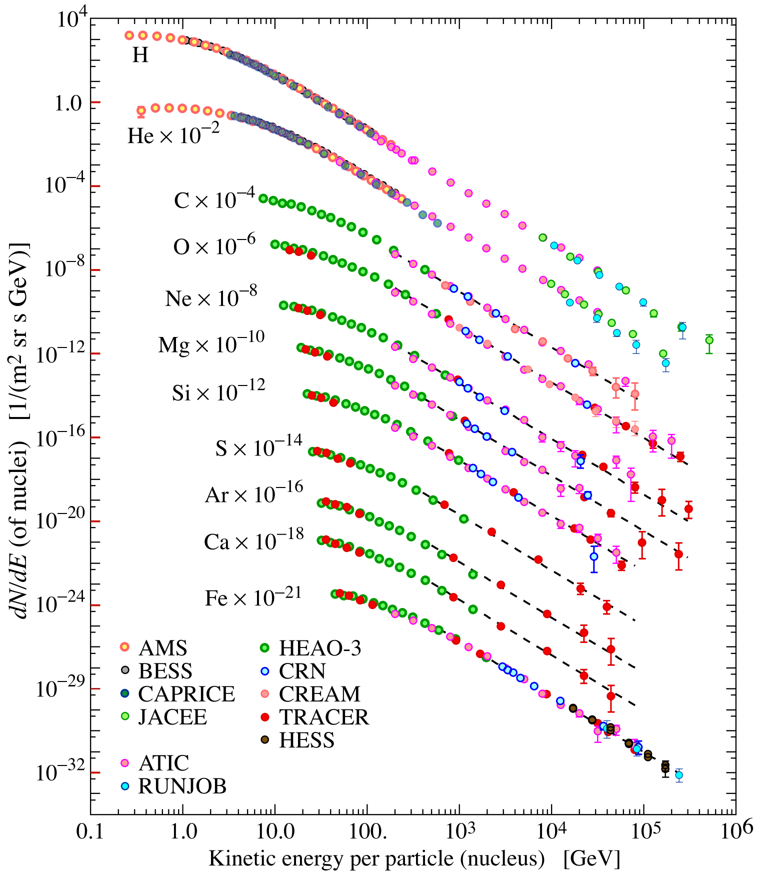

Figure 2.1: Differential flux (dN/dE) as a function of energy-per-nucleus are plotted vs energy-per-nucleus [21].

Variations in the cosmic-ray composition with energy, as seen in Figure 2.1, are due to differences in production between primary particles, produced at the source, and secondary particles, produced through spallation and other processes. A large number of cosmic-ray

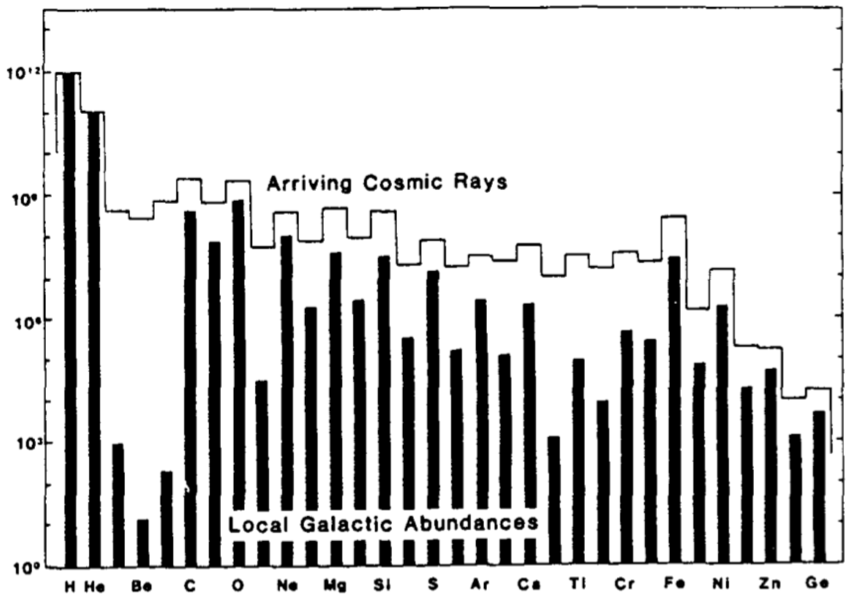

Figure 2.2: The abundances of cosmic ray elements detected at the Earth are indicated by the line. The bars represent the relative local Galactic element abundances. The two distributions are normalized to hydrogen. From [22].

isotopes and elements have relative abundances similar to interstellar abundances, but a few are over-represented due to heavier elements undergoing spallation. The relative element abundances are shown in Figure 2.2. For example, the elements right below iron and the light elements right above hydrogen and helium, produced by spallation processes, are over-abundant. These data can provide information about the origin and propagation of cosmic rays. The ratios of specific isotopes produced in spallation, such as ^{10}Be (half life 1.5×10^6 years) to ^{9}Be, can give information about the travel time of cosmic rays within the Galaxy.

2.1.2 Galactic Cosmic Rays

The measured local energy density of cosmic rays is about 1 MeV/m^3 for particles with energies above 10 GeV. Because particles of this energy are largely uniform and unaffected by magnetic fields in the solar system, that density is assumed to represent the energy density of cosmic rays throughout the Galaxy. The spectrum of cosmic rays at the lowest energies is modulated by solar winds, and so it changes with the solar cycle.

Cosmic-Ray Confinement

The escape time for Galactic cosmic rays is 10^6-10^7 years. Measurement of ^{10}Be, a radioactive byproduct of spallation by cosmic rays in the Galaxy have been used as a lower bound on cosmic-ray confinement. The expected production ratio of ^{9}Be to ^{10}Be is 2:1. Experiments measure a local ratio of 10:1. This means that the ^{10}Be produced by spallation has time to decay while trapped in the Galaxy and the cosmic rays are trapped for over 10^6 years. The details of this measurement can be found in [4]. Furthermore, if the cosmic rays were not trapped, but streamed freely from the Galaxy, the expected lifetime is only 10^3–10^4 years, and the measured cosmic ray distribution on the sky would be anisotropic. Therefore cosmic rays from Galactic sources are confined in the Galactic disk.

Due to magnetic fields in the Galaxy, the escape time of cosmic rays is energy-dependent. This can be seen in the energy dependence of spallation products. There are fewer at higher energies due to the higher-energy primaries escaping from the Galaxy. At the highest energies, protons can easily escape the magnetic fields in the Galaxy. The equation for the gyroradius is

$$r = \frac{\gamma m v_\perp}{\mid q \mid B}, \tag{2.1}$$

where γ is the Lorentz factor, m is the mass of the particle, $v_\perp$ is the perpendicular velocity, q is the charge of the particle, and B is the strength of magnetic field the particle is traveling through. For example, the gyroradius for protons with energies of 10^{18} eV is about the size of the Galactic disk. A heavier element like iron has a smaller radius, and is thus more confined. It is measured that there is a higher abundance of the heavier elements produced in the Galaxy at higher energies as a result of their longer escape time [4].

Cosmic-Ray Acceleration in the Galaxy

An acceleration process for charged particles in the Galaxy must account for measured cosmic-ray features, such as: particles with a power-law spectrum with a differential spectral index between negative two and three, particles with energies up to 10^{20} eV, and particles with the chemical abundances of the primary cosmic rays. The favored mechanism for accelerating cosmic rays is Fermi acceleration. It is a stochastic process in which particles are accelerated by colliding with clouds of material in the interstellar medium; it was first proposed in 1949 [23]. The original version is a process that accelerates particles by reflection among magnetic mirrors, and is only second order in V/c, where V is the velocity of the cloud relative to the shock front, and c is the speed of light. The particles are assumed to be in the region for some time, t_{esc}, and gain an average energy per interaction of:

$$\left\langle \frac{\Delta E}{E} \right\rangle = \frac{8}{3}\left(\frac{V}{c}\right)^2 \tag{2.2}$$

where $\Delta E = E'' - E$, where E'' is the energy after the increase from the interaction. This process has only a second-order energy increase, but the energy does increase exponentially with time due to particles getting accelerated in each interaction. However there are a few problems with the basic Fermi acceleration model. There are only a few collisions per year, and so the process is slow. Low energy particles need to quickly gain enough energy to overcome ionization losses. Finally, it ignores spectral broadening that occurs for a collection of particles injected with the same energy.

Diffusive shock acceleration (DSA) is a method for accelerating protons to energies of 10^{15} eV in strong shocks (such as those of SNRs). It was discussed independently by a number of researchers in the late 1970s (see for example [24]). Its key success has been to recreate a power-law spectrum from the physical interactions. Following the derivation in Longair [4], with N_0 the initial number of particles, $E = \beta E_0$, with β as the average energy increase per collision, and P, as the probability particles remain in the acceleration region after one collision, then after k collisions, the remaining number of particles N is

$$N = N_0 P^k \tag{2.3}$$

with energies

$$E = E_0 \beta^k. \tag{2.4}$$

Eliminating k between these quantities and considering that a fraction of the particles continue to be accelerated to higher energies, we get:

$$N(E)dE = \mathrm{const} \times E^{-1+\ln(P)/\ln(\beta)} dE. \tag{2.5}$$

This is a power-law energy distribution. It is then possible to derive β and P by examining the dynamics of the strong shock. It is convenient to work in the frame in which the shock (moving at a velocity U) is at rest. Figure 2.3 shows the appropriate reference frame. The gas flows into the shock with a velocity V_1 and out with a velocity V_2. The two velocities are related by the equation of continuity requiring mass is conserved across the shock

$$\rho_1 v_1 = \rho_1 U = \rho_2 v_2. \tag{2.6}$$

For a strong shock the ratio $\rho_2/\rho_1 = 4$ [4]. Then in the appropriate frame the gas approaches a high energy particle at $V = (3/4)U$.

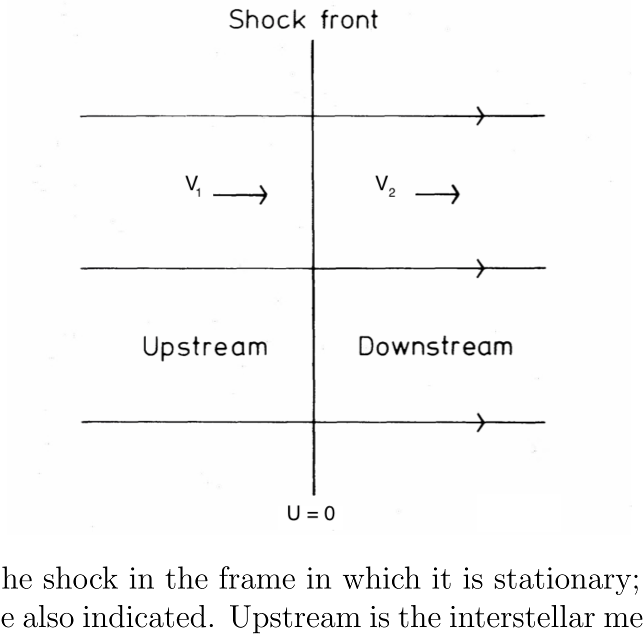

Figure 2.3: Figure of the shock in the frame in which it is stationary; adapted from [24]. v_1 and v_2 from the text are also indicated. Upstream is the interstellar medium and downstream is within the shock material.

With a Lorentz transformation, the particle's energy for one transition, for example upstream to downstream is,

$$E' = \gamma_V (E + p_x V), \tag{2.7}$$

with the x direction perpendicular to the shock. For a non-relativistic shock with relativistic particles: $V \ll c$, $\gamma_V = 1$, $E = pc$, and $p_x = E/c \cos\theta$. Therefore the energy increase per interaction is

$$\left\langle \frac{\Delta E}{E} \right\rangle = \frac{V}{c} \cos\theta. \tag{2.8}$$

We can then average over all angles to get

$$\left\langle \frac{\Delta E}{E} \right\rangle = \frac{2}{3}\frac{V}{c}. \tag{2.9}$$

Then we double this to account for the particles crossing both up- and down- stream and use the definition of β to find:

$$\beta = \frac{E}{E_0} = 1 + \frac{4}{3}\frac{V}{c} \tag{2.10}$$

for one round trip. The probability, P, can be found to be $P = 1 - U/c$, so

$$\frac{\ln P}{\ln \beta} = -1 \tag{2.11}$$

and

$$N(E)dE = const E^{-2} dE. \tag{2.12}$$

This process is equivalent to first-order Fermi acceleration (V/c) and it provides a physically motivated result for why different astrophysical environments with strong shocks accelerate particles with the same power-law spectrum. There are still some limits to this model: it requires the strong shocks of SNRs and because the process is not very rapid, the acceleration takes place in the first 10^3 years[1], there is an upper limit to the energy reached ($\sim 10^5$ GeV per nucleon). Modern models for acceleration in shock fronts include a number of extensions, such as: accounting for induced magnetic fields and other shock orientations (parallel shocks, perpendicular shocks, weak shocks, and relativistic shocks). DSA is shown to be up to 50% effective at converting the kinetic energy of the shock to the high-energy particles in modern numerical models [25]. Nonlinear models can furthermore accelerate particles to 10^{16}–10^{17} eV and, with the same energy being deposited per nucleon, higher mass nuclei undergo acceleration to higher energies. The *knee* for higher mass nuclei is at higher energies, and a superposition of these particles can account for the total spectrum up to energies of 10^{18} eV.

In summary, DSA is able to produce high-energy particles with properties that match the measured properties of cosmic rays. Supernova remnants (SNRs) are the astrophysical sources that can provide the power to accelerate cosmic-ray protons up to energies of 10^{15} eV, and contribute heavier nuclei to energies of 10^{18} eV by DSA.

Supernova Remnants

We can consider the volume of the Galaxy (V_{Gal}) to be that of a disk with a radius of 15 kpc and a height of 200 pc, use the escape time of cosmic rays (t_{esc}) of 2×10^7 years, and use the local cosmic ray energy density of 1 ev/cm^3 to estimate the cosmic-ray luminosity:

$$L_{CR} \sim (1\ \mathrm{eV/cm}^3)\frac{V_{gal}}{t_{esc}} \sim 10^{40}\ \mathrm{erg/s}. \tag{2.13}$$

Suppose one SN explosion occurs every 30 years or so and releases 10^{51} erg of energy, with a reasonable efficiency of converting energy to cosmic rays of $\sim 10\%$. Then SNRs would provide $\sim 10^{41}$ erg/s in cosmic-ray luminosity. While this is within the capabilities of the DSA process, we have not seen that high of a rate of SN explosions, and the efficiency of acceleration is more like a few percent. Other possible sources for proton acceleration include

---

[1] SNRs dissolve in $\sim 10^5$–10^6 years, with most of the acceleration in the first thousand years

massive stars, stellar winds, and superbubbles from merging SNRs. A better understanding of SNRs and other possible sources of cosmic-ray acceleration in the Galaxy is needed to determine if SNRs are the primary acceleration source for cosmic-ray protons.

2.2 Gamma-Ray Production in Galactic Sources

Gamma rays from astrophysical objects are a byproduct of a number of processes between primary protons and electrons, and material in the Galaxy. These processes include pion production and decay, inverse Compton scattering, and bremsstrahlung radiation. These mechanisms are summarized here, and are discussed in further detail in [4, 21, 26] and other papers.

2.2.1 Pion Production and Decay

Accelerated protons interact with the protons and nuclei in the interstellar medium. These interactions can produce a variety of particles. In particular, they produce neutral pions (π^0), which then decay into two gamma rays ($\pi^0 \rightarrow \gamma + \gamma$, with a lifetime of 8.52×10^{-17} s [21]). For a relativistic pion, the two gamma rays from the decay are beamed along the direction of travel. This means that the pion decay signature is a signature of accelerated hadronic particles interacting with matter at an astrophysical source. This process is diagrammed in Figure 2.4.

In order to produce π^0 particles, the interacting particles must have a kinetic energy greater than the rest-mass energy of the π^0. The π^0 mass is 134.97 MeV, so the threshold for π^0 production only is

$$E_{th} = 2m_\pi c^2(1 + m_\pi/m_p) \approx 280\text{MeV}, \tag{2.14}$$

where m_π is the π^0 mass and m_p is the proton rest mass. This is an important signature of pion production and decay in the pion-bump signature in the spectrum of astrophysical sources. Below about 70 MeV the production of gamma rays by this method is suppressed.

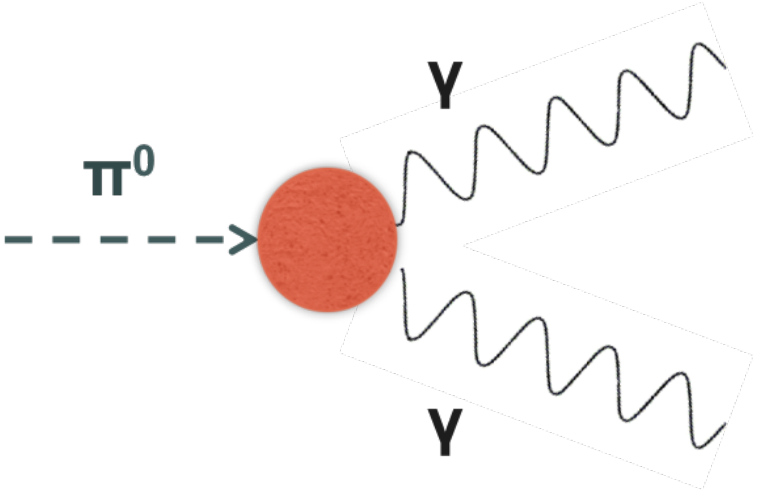

Figure 2.4: A diagram of a neutral pion (π^0) decaying into a pair of gamma rays (γ).

2.2.2 Inverse Compton Scattering

Compton scattering is the scattering of photons off free electrons, and the inverse process is the scattering of electrons off photons. Inverse Compton scattering by a cosmic-ray electron off an ambient photon (infrared radiation from dust, cosmic ray-background, etc.) will boost the photon energy up to gamma-ray energies. This process is diagrammed in Figure 2.5. For relativistic electrons (the Klein-Nishina regime), the maximum photon energy from a head-on collision is derived in [4] to be:

$$(\hbar\omega)_{max} \approx 4\gamma^2\hbar\omega_0. \tag{2.15}$$

Therefore electrons with Lorentz factors of $\gamma \sim 100$-1000 are capable of scattering optical photons to gamma rays. Inverse Compton scattering is an effective way to produce gamma rays. It also affects the cosmic-ray electron spectrum: whenever electrons pass through regions of high radiation density, they lose energy.

2.2.3 Bremsstrahlung

High-energy electrons also produce gamma rays through bremsstrahlung radiation. As a free electron passes near an atomic nucleus, its motion is deflected. The electron is decelerated

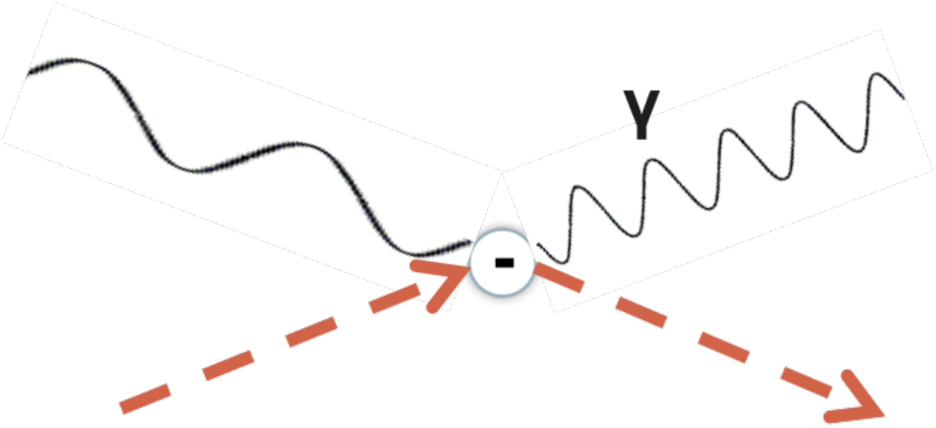

Figure 2.5: Diagram of Inverse Compton scattering, in which a low energy photon interacts with a high-energy electron and is scattered to gamma-ray energies.

and a photon is emitted, as shown in Figure 2.6. The rate of bremsstrahlung photon production is affected by the medium through which the electrons are streaming. In a region with higher interstellar medium density, the electron lifetime is expected to be shorter. The probability of emitting a photon decreases with higher energy. Therefore the probability of emitting a high-energy gamma-ray is low, but this process still contributes to the gamma-ray sky.

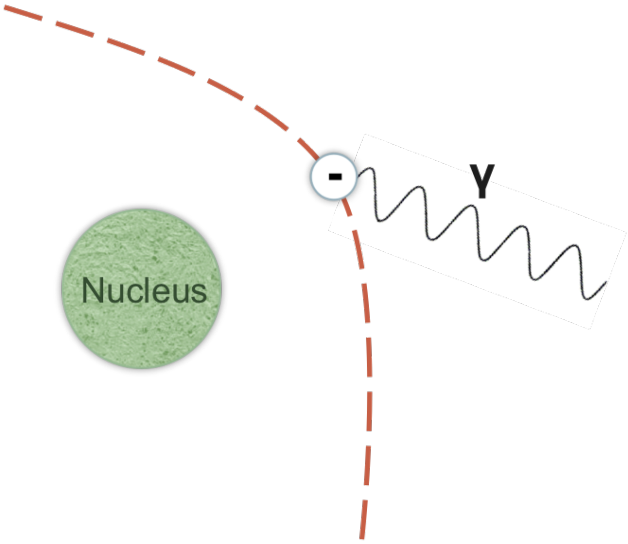

Figure 2.6: Diagram of emission of a high-energy photon by bremsstrahlung radiation.

2.3 Gamma-Ray Signatures of Cosmic-Ray Acceleration

The distribution of diffuse gamma rays in the Galaxy provides information about the distribution of protons and interstellar gas. They are produced by the pion production and decay mechanism discussed in Section 2.2.1. This process results in diffuse gamma-ray emission with a broad spectrum that has a peak around 70 MeV. There are also contributions to the diffuse gamma-ray spectrum from the inverse Compton and bremsstrahlung processes. This emission can be seen at low Galactic latitudes in the all-sky view of the gamma-ray sky provided by *Fermi*-LAT; see Figure 1.3. The diffuse emission traces interstellar matter measured in other wavelengths, and is similar to its predicted luminosity.

SNRs are the preferred mechanism for producing cosmic-ray protons up to energies of 10^{15} eV, and those protons can produce gamma rays via pion production and decay, as described above. The detection of SNRs in TeV gamma rays provides evidence for large particle fluxes at cosmic-ray energies (up to $\sim 10^{15}$ eV). The pion signature in SNRs is a direct sign of proton acceleration in astrophysical sources. Recently this has been directly measured in the SNRs IC443 and W44 by *Fermi*-LAT [3], shown in Figure 2.7. Measurement of the VHE gamma-ray spectra were key to determining that the pion production and decay mechanism is dominant in those sources. Also, in studies of Tycho's SNR (a type Ia SNR) by VERITAS, a hadronic scenario is preferred over an inverse Compton scenario, because the leptonic fit requires a magnetic field that is lower than expected [27].

Another key source type for Galactic VHE gamma-ray astronomy are pulsar wind nebulae (PWNe). The most famous of these is the Crab Nebula, also one of the brightest sources in the VHE sky. The Crab Nebula accelerates a wind of relativistic electrons and positrons [28]. HE gamma rays are then produced through synchrotron radiation from the relativistic electrons and positrons. Those HE gamma-rays then undergo inverse Compton scattering off the same relativistic electrons and positrons to VHE energies [29].

Sources of TeV gamma rays (produced by pion production and decay, inverse Compton scattering, and bremsstrahlung radiation) in the Galaxy provide evidence of proton and electron acceleration. Galactic PWNe spectra exhibit the TeV signatures of inverse Compton

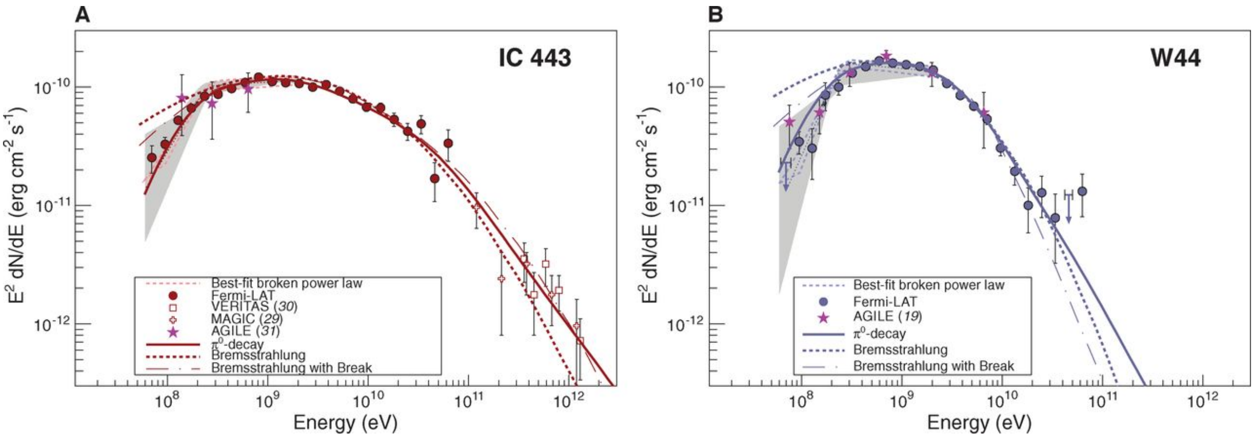

Figure 2.7: The π^0 decay signature detected in the spectra of SNRs by *Fermi*-LAT and IACTs in SNRs IC443 and W44. The solid lines denote the best fit π^0 decay gamma-ray spectrum. Figure from [3].

scattering at the sources. Recent evidence has been found in several SNRs of pion production and decay. However, more sources are needed with good spectral measurements over a broad energy range to determine if SNRs account for the majority of proton acceleration in the Galaxy. Furthermore, none of the sources identified so far has had clear evidence of accelerating particles above 10^{15} eV, so there is a need to find sources accelerating the higher energy particles that permeate the Galaxy. TeV gamma-ray surveys, such as the one discussed in this dissertation, provide a way to detect new sources and identify regions of cosmic-ray acceleration in the Galaxy.

CHAPTER 3

The Cygnus Region

The Cygnus region has a decades long history as a rich region of the Galaxy for studies of non-thermal emission. With a wealth of multiwavelength observations in the region we can start to piece together the nature of this unique region of the Milky Way Galaxy. This chapter starts with an overview of the source types in the region (Section 3.1), that include supernova remnants (SNRs), pulsars, and binaries. This is followed by a discussion of the high energy (HE) and very high energy (VHE) sources in the region. The chapter concludes with an introduction of Galactic source population studies in Section 3.2.

3.1 Multi-wavelength History

The Cygnus region is a complex region of the Galactic plane with sources in at least two spiral arms of the Galaxy as seen in Figure 3.1. It is one of the richest regions of star formation in the Milky Way Galaxy. The Cygnus-X complex was first identified as a source of diffuse radio emission in 1952 [30] and examinations of the region with numerous experiments over the subsequent decades have begun to unravel the nature of this uniquely bright region of the Galaxy. Radio observations reveal HII regions and molecular clouds, and optical observations reveal several OB star associations. The OB2 association, in particular, is of interest for its large number of massive stars whose stellar winds could heat molecular material in the region.

Early radio observations of the region revealed supernova remnants (SNRs) including the γ-Cygni Nebula and the "Crab-like" SNR CTB 87 [31, 32]. Furthermore a large superbubble structure was observed in x-rays in 1980 [33]; this prompted further study of the region in both radio and x-ray wavelengths. This resulted in the detection of the γ-Cygni SNR in

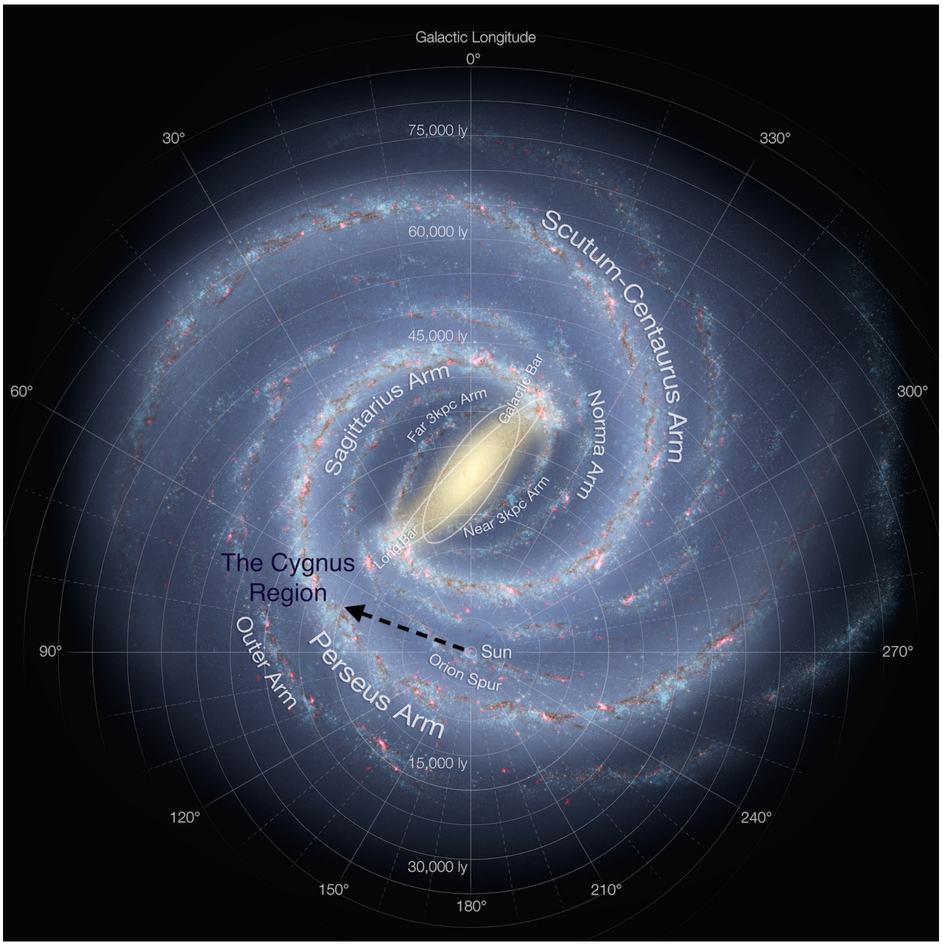

Figure 3.1: An artist's representation of the top down view of the Milky Way Galaxy (Credit: NASA/JPL-Caltech/ESO/R. Hurt); the Cygnus region (indicated by the arrow) has been labeled in navy.

x-rays [34]. Original interpretations of the superbubble involved an origin in the Cygnus OB2 region of massive stars, but further studies revealed that the superbubble is unlikely to be a single object [35]. Rather it is likely a superposition of astrophysical objects in the region.

3.1.1 Supernova Remnants

SNRs in the region include the previously mentioned γ-Cygni SNR and the “Crab-like” CTB 87. Optical observations of γ-Cygni agree with x-ray estimates of explosion energy of 10^{51} ergs over 7000 years ago [36, 37]. Its distance is estimated to be 1.7 kpc. The radio continuum view of γ-Cygni is shown in Figure 3.2 and is shown to complement the infrared (60 μm) and Hydrogen (21 cm radio) views in [38]. CTB 87 is an evolved remnant with evidence of a pulsar wind nebula in x-ray observations [39]. The distance to CTB 87 has been determined to be 6.1 kpc using radio H and CO observations [40].

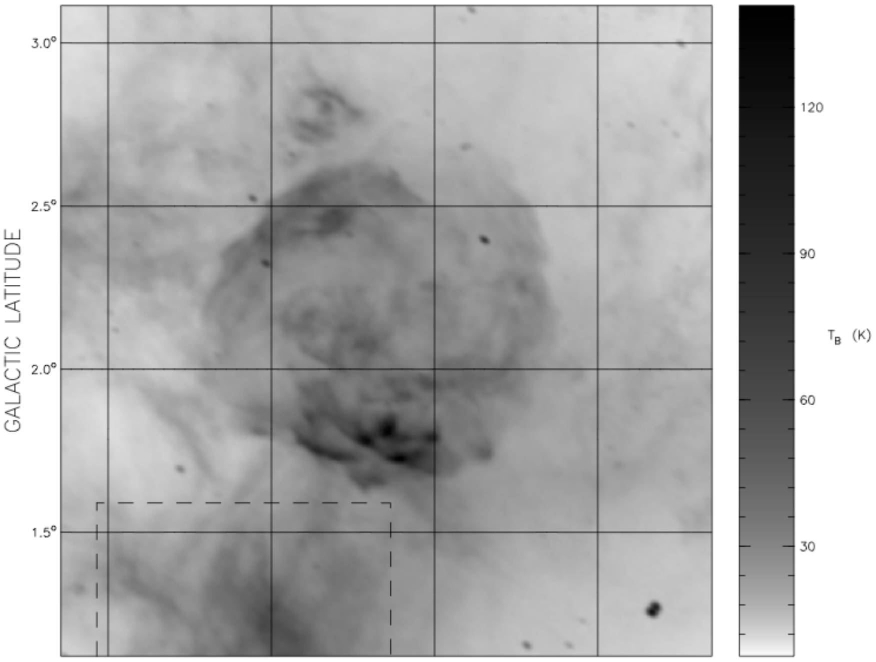

Figure 3.2: A Canadian Galactic Plane Survey radio continuum map of the γ-Cygni SNR at 1420 MHz. The spatial resolution is 0.8’ by 1.3’ [38].

There are a further six SNRs in the region as identified by Green’s supernova remnants catalogs [41–43]; see Table 3.1. Notably, CTB 80 (G69.0+2.7) is an old supernova in the snowplow phase approximately 1.5 kpc away [44] and it has an associated pulsar that could drive TeV emission. The other remnants include: G068.6-01.2 (a small faint radio SNR, not seen in gamma rays by *Fermi*-LAT), G069.7+01.0 (a radio detected shell SNR with a possibly coincident x-ray shell that is of a larger extent, not seen in gamma rays by *Fermi*-LAT), G073.9+00.9 (a radio detected shell type SNR seen by *Fermi*-LAT in gamma rays, 3FGL J2014.4+3606, but not seen in x-rays, with an estimated distance of 1–2 kpc and an estimated age of 11,000 to 12000 years, see [45]), and G076.9+01.0 (a filled SNR about 8 kpc away and 8900 years old seen in x-rays and with a x-ray and gamma-ray PWN). Details about these SNRs can be found in the Manitoba catalog [46]. This catalog provides further information on the detection of SNRs in x-ray, HE, and VHE wavelengths.

Table 3.1: SNRs in the Cygnus region as detailed in the Green's SNR catalogs: [41–43]. The Green's naming convention is in terms of location in Galactic coordinates, given in columns two and three. Alternate names of the SNRs from previous works are given in the final column.

Name	Glon (deg)	Glat (deg)	Alternate names
G068.6-01.2	68.6	-1.2	
G069.0+02.7	68.84	2.78	CTB 80
G069.7+01.0	69.69	1.0	
G073.9+00.9	73.91	0.88	
G074.9+01.2	74.94	1.14	CTB 87
G076.9+01.0	76.9	0.97	
G078.2+02.1	78.14	2.19	DR4, γ-Cygni SNR

3.1.2 Pulsars

Pulsars in the region are numerous (see Table 3.2) and cover a range of pulsar properties. Few are expected to contribute heavily at TeV energies because the spectra of pulsars observed at GeV energies fall off exponentially. However, pulsars can power PWNe, which can accelerate particles to multi-TeV energies. Pulsars of particular interest in the Cygnus region include the *Fermi*-LAT detected pulsars: PSR B1951, PSR J2021+3651, PSR J2021+4026, PSR J2030+4415, and PSR J2032+4127, as well as those associated with supernova remnants such as PSR J2022+3842, an energetic pulsar detected in HE gamma rays, x-rays and radio

[47]. Chandra observations of PSR J2021+3652 reveal a nebula at most 3–4 kpc away (closer than implied by the pulsar dispersion measure) with a bow shock and jets, named the "Dragonfly Nebula" [48].

Table 3.2: Pulsars in the Cygnus region as identified by the Australia Telescope National Facility (ATNF) pulsar catalog [49]. The naming convention is in right ascension (RA) and declination (dec), so the coordinates in Galactic latitude and longitude are also given for each pulsar in degrees, followed by the pulsar period in seconds, and any associated objects are in the final column.

Name (PSR)	Glon (deg)	Glat (deg)	Period 0 (s)	Associations
B1951+32	68.7	2.82	0.03953119285	CTB 80 2FGL J1953.0+3253
J1959+3620	72.4	3.44	0.406081181	*
B2000+32	69.3	0.88	0.6967605102	*
B2002+31	69.0	0.02	2.111264734	*
J2004+3429	71.4	1.57	0.2409526419	*
J2005+3547	72.6	2.18	0.6150338949	*
J2005+3552	72.7	2.14	0.3079429046	*
J2006+3102	68.7	−0.53	0.1636952365	*
J2007+3120	69.0	−0.53	0.6082053146	*
J2009+3326	71.1	0.12	1.438368602	*
J2010+3230	70.4	−0.50	1.442447521	*
! J2011+3331	71.3	−0.05	0.9317330935	*
B2011+38	75.9	2.48	0.2301936139	*
J2018+3431	73.0	−0.84	0.3876640866	*
J2021+3651	75.2	0.11	0.1037409521	AGL J2020.5+3653 2FGL J2021.0+3651
J2021+4026	78.2	2.09	0.2653176609	2FGL J2021.5+402 G78.2+2.1 2XMM J202131.0+402645
J2022+3842	76.9	0.96	0.04857877964	CXOU J202221.68+384214.8 G76.9+1.0
B2027+37	76.9	−0.73	1.216804658	*
J2029+45	82.7	3.59	1.099	*
J2030+4415	82.3	2.89	0.2270701774	2FGL J2030.7+4417
J2032+4127	80.2	1.03	0.1432499	MT91 213,Cygnus OB2

3.1.3 Binaries

Binaries are another class of source of interest to VHE gamma-ray studies. Of particular interest are binaries in which a main sequence object orbits a compact remnant such as a white dwarf, neutron star, or black hole. There are four such binaries known in the region. Each binary has considerable x-ray emission associated with it as identified in the Liu catalogs of low and high-mass x-ray binaries [50, 51]. Cygnus X-1 and Cygnus X-3 are high-mass x-ray binaries (binary systems that are bright in x-rays, typically with a compact object such as a neutron star or black hole with a massive stellar companion). They have been observed by IACTs as possible TeV emitters. They are of particular interest as microquasars (accreting compact objects such as a black hole), and are therefore useful for studying black holes and active galaxies. Cygnus X-1 and Cygnus X-3 have not yet been detected by the current generation of VHE telescopes and have flux limits at the 1–2% Crab Nebula emission level [52, 53]. 3A 1954+319 and XTE J2012+381 are low mass x-ray binaries (systems in which the stellar companion of the compact object is less massive than the compact object), and are not expected to emit VHE photons.

Table 3.3: Low and high-mass x-ray binaries from the Liu catalogs [50, 51]. This table gives their names and positions in Galactic coordinates, as well as associated objects/alternate names.

Name	Glon (deg)	Glat (deg)	Alternative objects
4U 1956+35	71.3	3.1	O9.7 Iab, Cyg X-1, V1357 Cyg
3A 1954+319	68.4	1.93	
XTE J2012+381	75.4	2.22	
4U 2030+40	79.8	0.7	WR star, Cyg X-3

3.1.4 Gamma-Ray Sources

So far the catalogs discussed have relied on radio, infrared, and x-ray observations in the Cygnus region. Next are the sources that have been detected as HE and VHE emitters specifically.

HE Gamma-Ray Sources

The EGRET (Energetic Gamma-Ray Experiment Telescope) instrument on the Compton Gamma-Ray Observatory satellite revealed the first HE gamma-ray emission in the region. It detected numerous sources as well as prominent diffuse emission in the region [54, 55].

2EG J2020+4026 is a HE source associated with the γ-Cygni remnant and was determined to have a spectrum characteristic of a pulsar [56]. Observations by the *Fermi*-LAT telescope have revealed many new sources and have resolved sources of diffuse emission into numerous point sources.

The *Fermi*-LAT experiment, detailed in Chapter 6, has released a number of point source catalogs from their all-sky survey observations, at 1 year (1FGL)[57], 2 years (2FGL) [58], and 5 years (3FGL) [59], as well as two HE catalogs (1FHL and 2FHL) [60, 61]. These catalogs reveal numerous sources in the region, including pulsars, SNRs, extragalactic sources seen through the Galaxy, and many unidentified sources. There are 25 sources in the region in the 3FGL catalog; 12 have associations in the 2FGL and/or 1FGL catalogs, seven of them are found in both. These catalogs were made using all-sky observations from 100 MeV to 100 GeV (in the 1FGL and 2FGL) or 300 GeV (in the 3FGL). As the observatory has gathered more data and gained improved knowledge of the instrument response, the collection and understanding of higher energy photons has improved, thus enabling the HE catalogs: 1FHL (10 GeV to >300 GeV) and 2FHL (50 GeV to 2 TeV). Furthermore there have been a number of papers on specific sources of interest in the Cygnus region.

The *Fermi*-LAT collaboration, and other groups, have reported detailed analyses of key sources in the Cygnus region. The *Fermi*-LAT collaboration has reported that the bright pulsar source PSR J2021+3651, first detected as a possible pulsar by EGRET, which is at a distance of around 4 kpc [48], does not demonstrate significant nebular emission [62]. The *Fermi*-LAT has also discovered the pulsar PSR J2032+4127 [63], which was then detected in the radio as well [64]. They measure its distance at about 3.6 kpc, but they speculate that it is more likely to be associated with the OB2 association at 1.7 kpc. They mention a nearby star as a possible binary companion to the pulsar, but it was only recently that the star was determined to be in a binary with the pulsar with a 20–30 year period [65]. They also discovered a pulsar in the region of the CTB 80 SNR, but do not report off-pulse emission [66]. Furthermore, the *Fermi*-LAT collaboration has reported variable emission from Cygnus X-3, the microquasar x-ray binary, with the orbital period detected in gamma rays, and the gamma-ray emission correlated with the radio emission [67].

Table 3.4: *Fermi* (3FGL) catalog sources in the region with locations in Galactic coordinates, and flags for appearing in other *Fermi*-LAT catalogs, followed by a final column with associated HE and VHE sources [57–61]. † Association with the 3FGL source unclear

3FGL Name	Glon (deg)	Glat (deg)	! 1FGL	2FGL	1FHL	2FHL	Other Associations
J1952.9+3253	68.7814	2.8258	yes	yes	yes	*	PSR
J2004.4+3338	70.6708	1.1855	yes	yes	yes	*	*
J2014.4+3606	73.8595	0.7974	*	*	*	*	*
J2015.6+3709	74.8648	1.1857	*	yes	*	yes	VERITAS † Galaxy
J2017.9+3627	74.5412	0.4109	yes	yes	yes	*	Milagro
J2018.5+3851	76.5927	1.6639	yes	yes	yes	*	Galaxy
J2018.6+4213	79.4023	3.5307	*	*	*	*	*
J2021.0+4031e	78.2408	2.1967	*	yes	yes	yes	γ-Cygni Nebula VERITAS
J2021.1+3651	75.2325	0.1131	*	yes	*	*	PSR Milagro
J2021.5+4026	78.2312	2.0833	yes	yes	*	*	LAT PSR
J2022.2+3840	76.8545	0.9628	yes	yes	yes	*	*
J2023.5+4126	79.2531	2.3417	*	*	*	*	*
J2024.6+3747	76.4068	0.0653	yes	*	*	*	*
J2026.8+4003	78.4916	1.0252	*	*	*	*	*
J2028.5+4040c	79.1851	1.1296	*	*	*	*	*
J2028.6+4110e	79.6007	1.3963	*	*	*	yes	Cygnus Cocoon Milagro
J2032.2+4126	80.2182	1.019	*	*	*	*	LAT PSR TeV
J2032.5+3921	78.5731	−0.2684	*	*	yes	*	*
J2032.5+4032	79.5131	0.4383	yes	yes	yes	*	*
J2034.6+4302	81.7667	1.6038	*	yes	*	*	*
J2036.8+4234c	81.6334	0.9972	*	*	*	*	*
J2037.4+4132c	80.8683	0.2946	*	*	*	*	*
J2038.4+4212	81.5271	0.5428	*	*	*	*	*
J2039.4+4111	80.8292	−0.2075	*	*	*	*	*
J2042.4+4209	81.9318	−0.0711	*	*	*	*	*

The *Fermi*-LAT has also been an extremely valuable tool for studying the diffuse gamma-ray emission in the Galaxy and how it relates to cosmic-ray transportation. One key discovery in the Cygnus region was of the Cygnus cocoon of emission [68], now associated with freshly accelerated cosmic rays. It was determined that cavities formed by young stellar clusters in the region (such as OB2) form a cocoon of hard cosmic rays. Modeling determined that the density of cosmic-ray particles in the region is 1.6–1.8 times the local cosmic ray density and they discuss that it is unlikely a single source like γ-Cygni could account for all of the accelerated particles in the region. X-ray observations by the *Suzaku* instrument have excluded electron acceleration to energies of 50 TeV [69]. However, the cocoon would be difficult to detect by VERITAS due to its large angular size, which is about the same as the field-of-view of the VERITAS camera.

A full analysis of the region using the *Fermi*-LAT data is undertaken as part of this dissertation, and is detailed in Chapter 7.

VHE Sources

With this wealth of multiwavelength targets and numerous regions of interest and sources identified by previously operating TeV instruments, such as HEGRA, Whipple, and Milagro, the Cygnus region is a rewarding region to study with TeV instruments.

The first unidentified TeV source, TeV 2032+4126, was discovered by the HEGRA collaboration in the Cygnus region [70, 71]. The source flux was determined to be about 5% of the Crab Nebula flux, spatially extended, and with a power-law spectrum with an index of −1.9. The source detection was confirmed in archival data from the Whipple 10 m experiment [72, 73]. Radio and x-ray follow-up observations determined no clear single counterpart, but the authors pointed out that the Cygnus OB2 region could contribute to the TeV flux through the interactions of stellar winds [74]. Two Micron All Sky Survey (2MASS) measurements of the OB2 region were used to determine that it has the most O stars of any galactic massive star association [75]. It is a region with rich molecular targets for locally accelerated cosmic rays [76]. Most recently, TeV J2032+4126 has been associated with the *Fermi*-LAT pulsar, PSR J2032+4127, and has been detected both by Milagro (below) and VERITAS (See Chapter 7).

The Milagro experiment undertook detailed studies of the region, first measuring upper limits in [18]. This was followed by the discovery of MGRO J2019+37, the brightest extended TeV source in the northern hemisphere [77]. This was further confirmed by the Tibet Air Shower Array [78]. This source is associated with a number of objects, discussed in the context of the VERITAS detection in Section 7.3.3. The Milagro survey of the Galactic plane yielded the further discovery of an extended source near TeV J2032+4126 [79–81]. The Milagro view of the Cygnus region is shown in Figure 3.3 and it shows a large source of emission associated with MGRO J2019+37, as well as a smaller source associated with TeV J2032+4126. Milagro measured diffuse emission in the Cygnus region at twice the predicted flux that is predicted from cosmic-ray propagation and interaction models, such as GALPROP [82]. Thus it was determined that a substantial fraction of the diffuse emission measured by Milagro is associated with active cosmic-ray sources [83].

3.2 VHE Galactic Source Populations

3.2.1 The Inner Galaxy

From 2004 through 2013, H.E.S.S. undertook a survey of the inner region of the Galaxy (from 250° to 65° in Galactic longitude and from $-3.5°$ to $3.5°$ in Galactic latitude), the H.E.S.S. Galactic Plane Survey (HGPS). This survey has led to the discovery of over 60 Galactic TeV sources. The HGPS has over 2800 hrs of data, with a sensitivity to point-like sources of down to 2% of the Crab Nebula flux.

The VHE gamma-ray source population in the HGPS is dominated by objects such as PWNe (∼35%) and SNRs (∼21%) [84]. For a large number of the sources that H.E.S.S. has detected, however, the physical origins of their emissions remain unclear, and these sources remain unidentified (∼31%). The rest of their source population includes massive stellar clusters, binary systems, and two extra-galactic sources. With their extensive coverage of

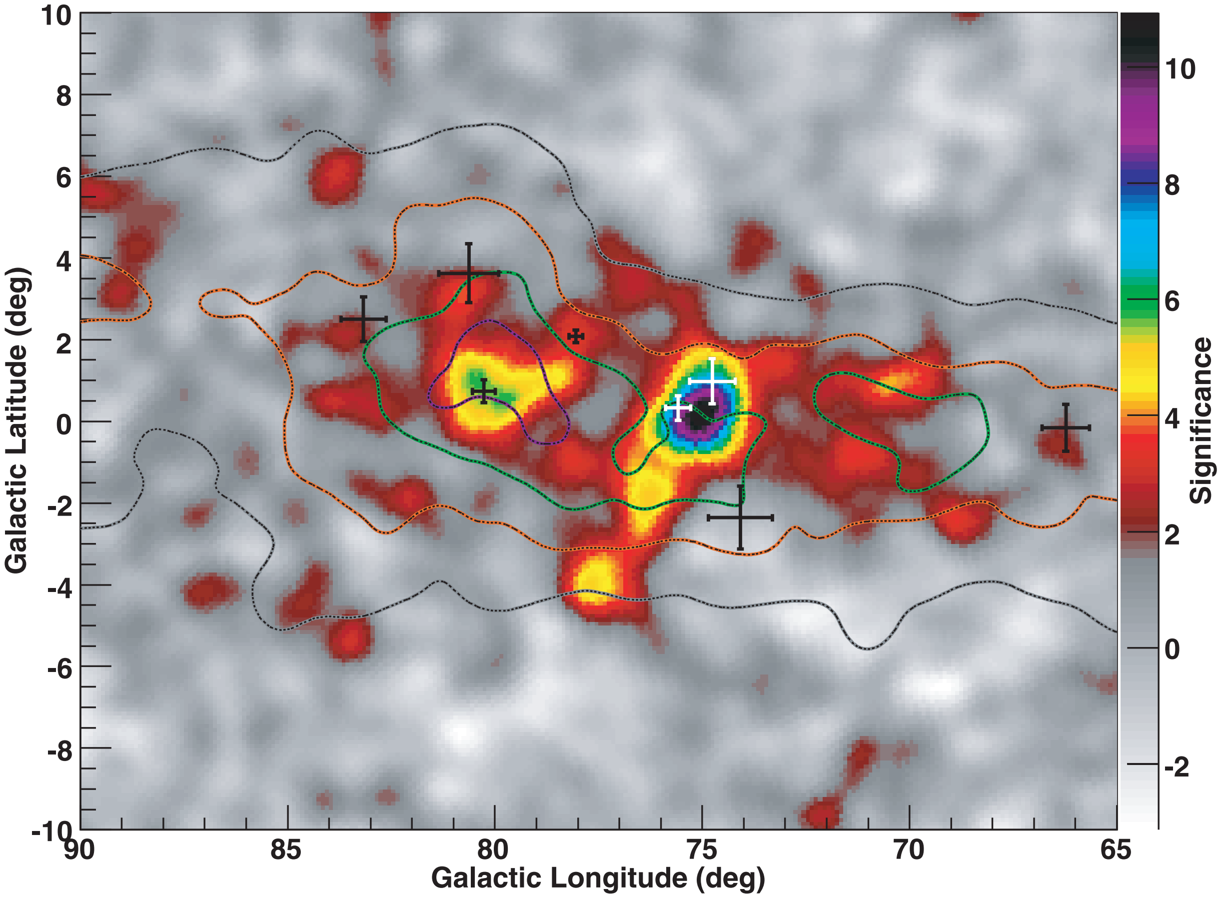

Figure 3.3: The Milagro map of the Cygnus region of the Galaxy. The color bar is in units of significance in standard deviations. The contours trace matter in the region from CO and HII surveys of the region. The crosses indicate EGRET sources. The large region with high significance is associated with MGRO J2019+37, and the smaller region to the left, with lower significance, is associated with TeV J2032+4126. Figure from [77].

the inner Galaxy, H.E.S.S. has been able to start to study the general TeV source population, including: the population of PWNe and SNRs [85, 86], and diffuse emission from the Galactic plane and the spectral morphology of the Galactic center. [87].

The observations made by H.E.S.S. include many hours of follow-up observations and thus H.E.S.S. has detected many sources with relatively low TeV gamma-ray fluxes (i.e. below 5% Crab Nebula flux), as well as many bright sources. Furthermore, almost all sources in the Galactic plane have measurable angular extension, especially notable in sources like SNRs and PWNe. The distributions of source fluxes and sizes are shown in Figure 3.4, these distributions are drawn from the H.E.S.S. source catalog [88]. The HGPS has proven the usefulness of a sensitive sky survey, but has only surveyed the southern portion of the Galactic plane. VERITAS is well suited to do similar studies in the northern sky.

In summary, the Cygnus region has been observed by a number of experiments in many wavelengths. Radio and x-ray observations determined that the Cygnus region demonstrated a large amount of non-thermal emission. Those observations along with gamma-ray observations have determined specific sources which are of interest to VHE studies. It has thus been determined to be a region with a wealth of sources that can contribute to Galactic cosmic-ray acceleration.

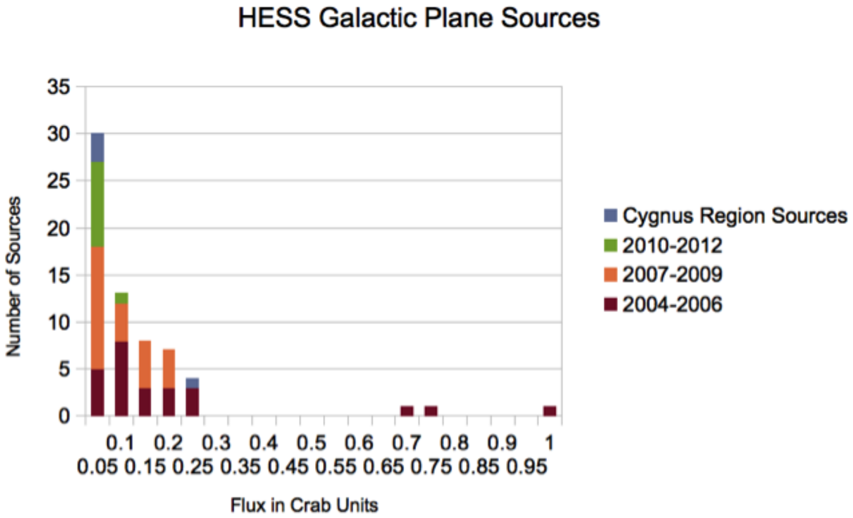

(a) Distribution of source fluxes

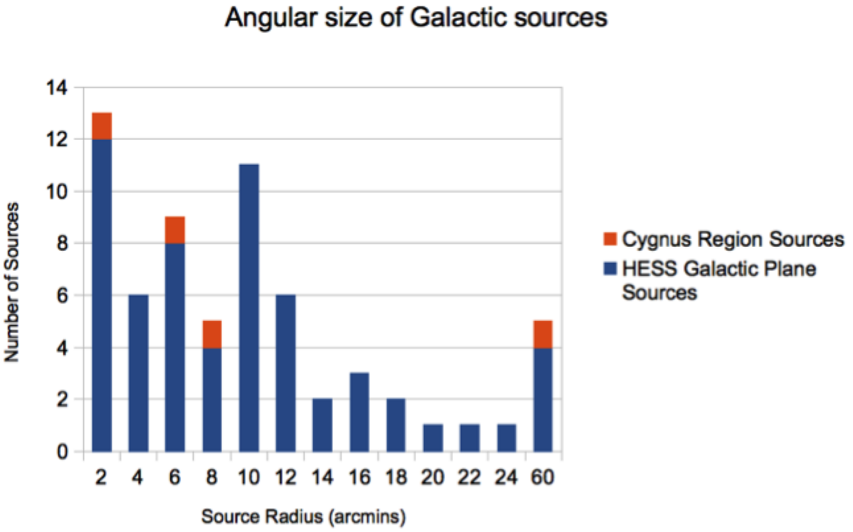

(b) Distribution of source Angular Size

Figure 3.4: On the top (a) is a histogram of the fluxes of the sources that H.E.S.S. has detected in their Galactic plane survey and from follow-up observations in bins of 5% Crab Nebula flux. On the bottom (b) is a histogram of the angular size of the same sources. In both histograms the VERITAS Cygnus region sources are added, and these sources are discussed in more detail in Section 7.3.

CHAPTER 4

Imaging Atmospheric Cherenkov Technique for Very-High-Energy Gamma-Ray Astronomy

This chapter outlines the basics of the technique employed by imaging atmospheric Cherenkov telescopes (IACTs) such as VERITAS. It starts with an overview of the properties of air showers and continues with a brief discussion of the detection method. The VERITAS experiment and analysis procedure are detailed in Chapter 5.

4.1 Extensive Air Showers

When cosmic rays and gamma-ray photons interact with the Earth's atmosphere, they produce a cascade of energetic particles (leptons, hadrons, and photons) known as an extensive air shower (EAS). In the case of a gamma ray, an incident photon interacts with the electromagnetic field of a nucleus in the air and produces an electron-positron pair that share the energy of the initial photon and travel in nearly the same direction. These particles are themselves energetic enough to emit bremsstrahlung photons along the direction of travel. Those photons can then interact again to create another electron-positron pair. At each step some energy is lost, but the process can continue (adding more and more particles to the shower) until the typical particle energy is small enough so that the dominant interactions are ionization processes. When the primary particle is a photon or electron/positron, the shower is referred to as an electromagnetic shower; when it is a hadron, the shower is a hadronic shower. Hadrons make up the majority of the primary particles and are thus a large source of background for gamma-ray experiments. Understanding these two types of extensive air showers is critical to discriminating gamma-ray-like primaries from proton-like

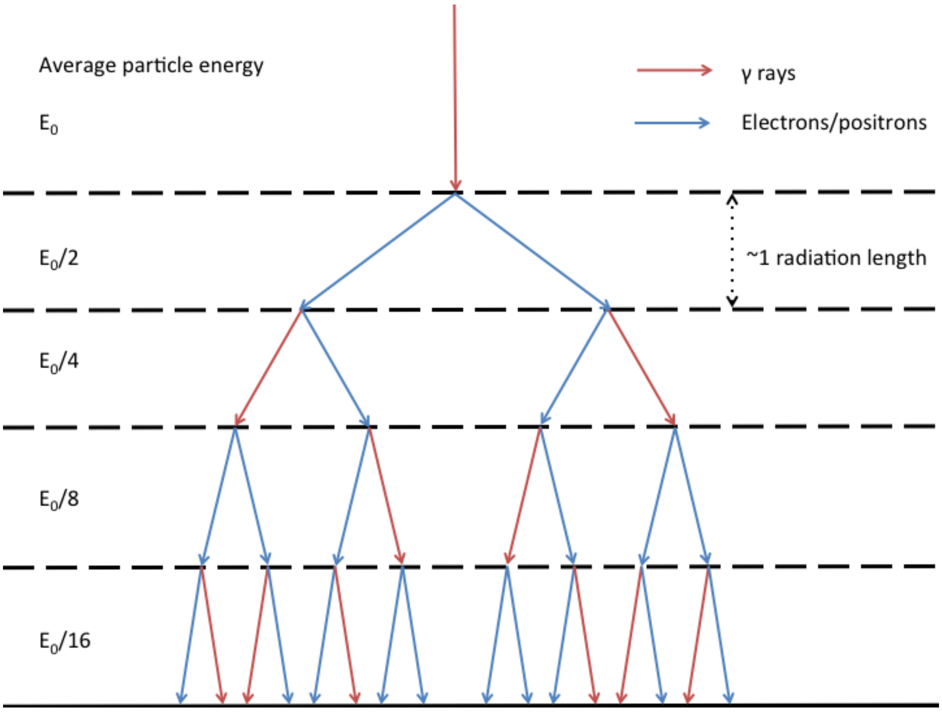

Figure 4.1: Schematic of electromagnetic shower development for a gamma-ray initiated shower. The average energy of each particle in the shower (as a fraction of E_0) is marked on the figure. Adapted from [4].

primaries. These two showers are discussed in further detail below.

4.1.1 Electromagnetic Air Showers

When a high-energy gamma ray enters the atmosphere, it travels some distance and then interacts with a nucleus to create an electron-positron pair. This pair roughly splits the energy of the incoming particle. Each of these particles can then generate high-energy photons through bremsstrahlung radiation, and those photons can create an electron-positron pair again. A schematic representation of the model for an electromagnetic air shower initiated by a photon is presented in Figure 4.1. The number of particles in the shower increases geometrically with atmospheric depth.

This process continues until the average energy of the particles is low enough that ionization processes become the dominant energy loss mechanism for the electrons and positrons. A key feature of the pair production process is that the directions of the electrons and positrons have a small angle of deflection relative to the direction gamma ray that initiates them. Further along, the photons begin to lose energy by Compton scattering and photoelectric absorption. The processes that dominate the attenuation of photons of different energies are shown in Figure 4.2. The critical energy, below which ionization dominates, is about 80 MeV for electrons. For photons with energies below about 30 MeV, Compton scattering begins to dominate over pair production. Thus the number of particles in the shower falls off after the maximum number of particles is reached, when the energies are approximately this critical energy. The first development of this model was by Rossi and Greisen in 1941; Figure 4.3 shows their model for the number of shower particles versus atmospheric depth [89]. Showers for lower energy primaries reach their maximum number of particles (electrons, positrons, and photons) at higher altitudes, die out earlier, and contain fewer particles, than showers for higher energy primaries. Notably this model does not include particles other than electrons, positrons, and photons, as opposed to hadronic showers, discussed next.

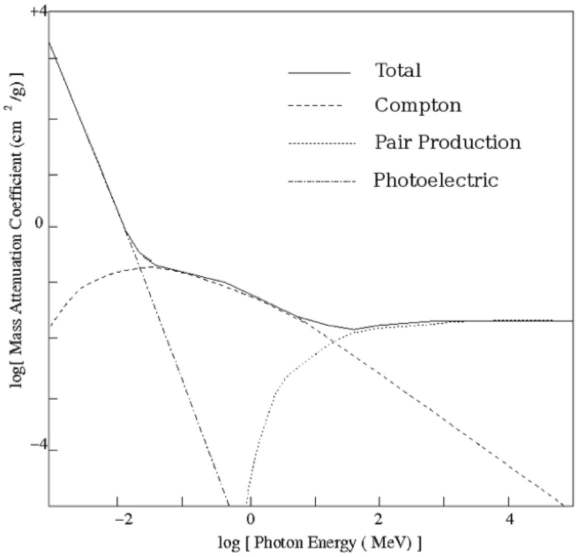

Figure 4.2: The log mass attenuation coefficient in cm^2/g versus photon energy. This shows the primary interaction mode for a gamma ray of a certain energy [90].

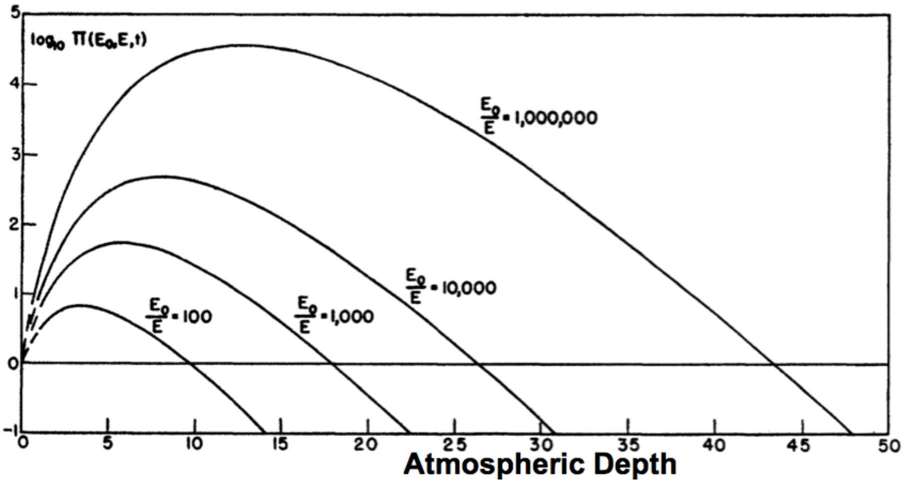

Figure 4.3: The number of particles (electrons, positrons, and photons) in a shower versus atmospheric depth for a shower initiated by an electron with energy E_0 [89].

4.1.2 Hadronic Air Showers

When a high-energy cosmic-ray proton or nucleus enters the atmosphere, it initiates a hadronic air shower with a core of hadronic interactions, along with muonic components and electromagnetic sub-showers. These interactions are diagrammed in Figure 4.4. The energy of the primary particle is shared among pions, kaons (which decay into pions and other particles), and light baryons. The secondary nuclei and charged pions multiply until the energy drops below that required for pion production, about 1 GeV. Secondary protons lose energy through ionization. Neutral pion (π^0) secondaries almost immediately decay into two gamma rays. These gamma rays initiate electromagnetic cascades; these are electromagnetic sub-showers. The charged pions decay into muons and neutrinos. Because the nuclear interaction and ionization losses for muons is low and because the muons are moving relativistically, they survive to penetrate to the ground in significant numbers.

Electromagnetic and hadronic showers have key differences. A side by side comparison of photon and proton showers each initiated by a 100 GeV primary is presented in Figure 4.5. It can be seen that the hadronic secondaries have more lateral extension due to processes that introduce transverse momentum like inelastic scattering and particle decay. In the electromagnetic case, the primary interactions are pair production and Bremsstrahlung interactions with small scattering angles. The hadronic showers have large particle density

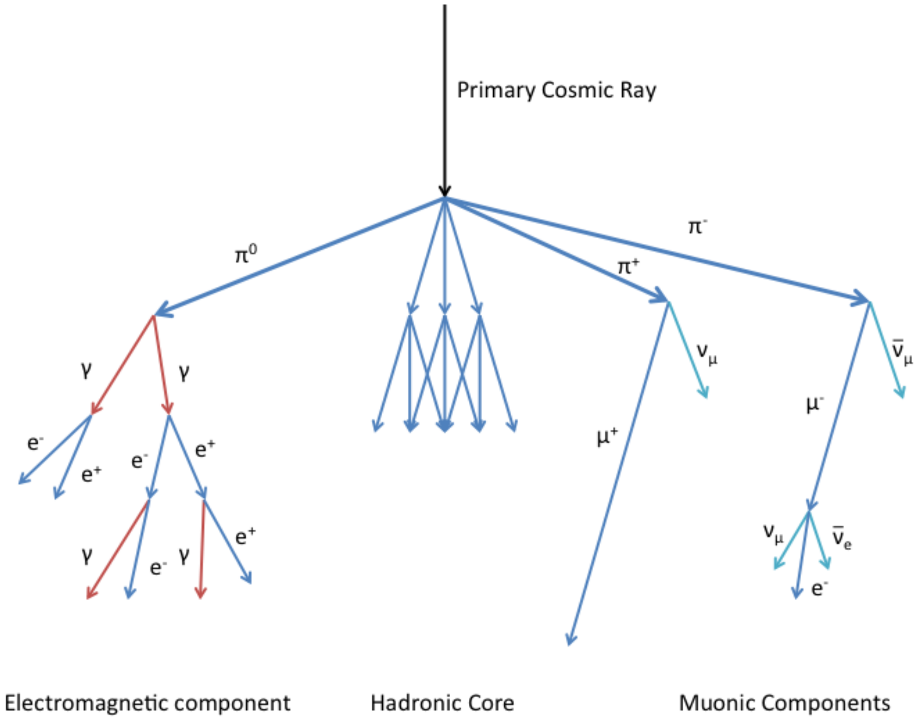

Figure 4.4: A schematic for the interactions in a hadronic air shower. Adapted from [4].

fluctuations due to multiple showers and are less uniform. Therefore the electromagnetic initiated showers have less lateral spread than hadron initiated showers. The secondary particles of hadronic showers penetrate more deeply into the atmosphere due to a longer mean path length between interactions. The mean free path length for inelastic scattering between protons and air is about 800 kg/m^3 versus a mean free path length of 350 kg/m^3 for bremsstrahlung or pair production interactions with gamma-ray photons. These differences are useful for distinguishing background hadronic showers from gamma-ray-like showers in the analysis of IACT data discussed in Section 5.3.5.

4.1.3 Cherenkov Emission from Air Showers

The particles of the air shower emit a cone of Cherenkov radiation as they travel through the atmosphere. This light is emitted as long as the velocity of the charged particle exceeds

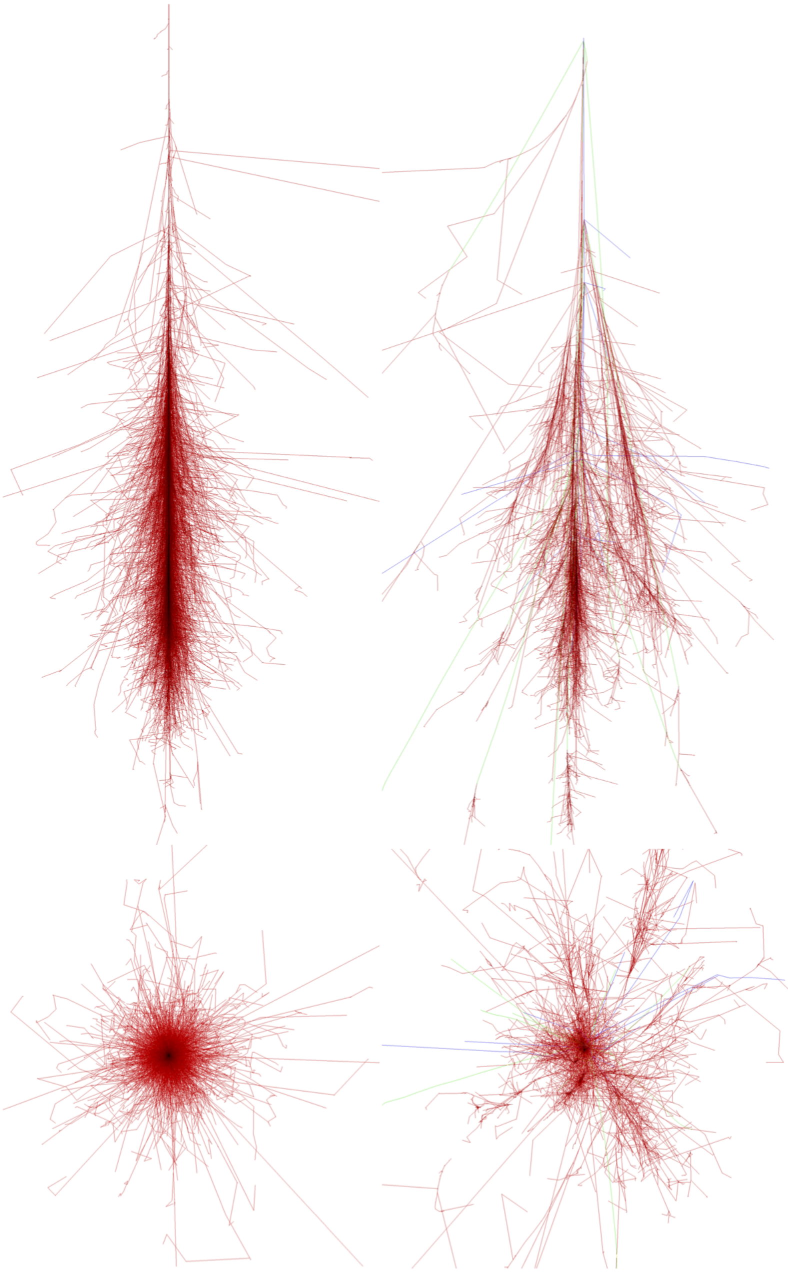

Figure 4.5: Shower simulations for a 100 GeV photon (left) and proton (right). The top shows the longitudinal development of the shower. The bottom shows the lateral distribution. The gamma-ray-initiated shower shows less lateral spread and more uniformity than the proton-initiated shower of the same energy. Images from [5], based on CORSIKA simulations [6].

the speed of light in the medium through which it is traveling, i.e.

$$\beta n > 1, \tag{4.1}$$

where n is the index of refraction in the medium, and $\beta = v/c$ is the ratio of the velocity of the particle in the medium to the speed of light in a vacuum. The Cherenkov radiation comes about because the particle induces a polarization in the particles of the atmosphere, and this causes the particles to radiate photons. The forward traveling photons constructively interfere to form the cone of light, as shown in Figure 4.6. The angle of this cone of radiation is determined by the particle velocity, v, and the velocity of light in the medium ($c' = c/n$):

$$\cos\theta_C = \frac{c'}{v} = \frac{1}{\beta n}. \tag{4.2}$$

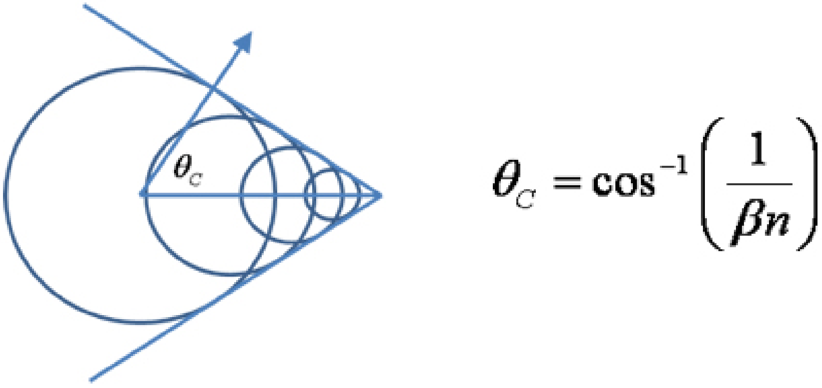

Figure 4.6: The wavefront of Cherenkov light emitted by a charged particle moving in a medium with refractive index n, with a velocity greater than c/n. The angle of emission is $\theta_C = \cos^{-1}\frac{1}{\beta n}$.

The light emission requires $\beta \geq 1/n$; this leads to a minimum particle energy for Cherenkov emission of:

$$E_{min} = \frac{mc^2}{\sqrt{1-\beta^2}}, \tag{4.3}$$

where m is the rest mass of the particle. Using $n = 1.00029$ for air, this energy threshold is

21 MeV for an electron.

The density of the air, and therefore the refractive index, varies with altitude, so the Cherenkov angle also varies with altitude. The angle increases lower in the atmosphere. Thus the light from different altitudes superimpose on each other at observation level with a characteristic ring seen in Figure 4.7. Furthermore, most of the photons are emitted near shower maximum. Because the process is calorimetric, the number of Cherenkov photons scales with energy. Figure 4.7 (a) shows the distribution of Cherenkov photons on the ground as a result of a gamma-ray shower due to a 1 TeV primary photon, and Figure 4.7 (b) shows the lateral distribution of the photons for different primary energies. The "Cherenkov light pool" is the relatively flat portion of this distribution, out to about 120 m. For a 100 GeV shower, the density of Cherenkov photons at an altitude of about 1000 m is only about 10 photons per square meter. The IACT method relies on large mirrors and sensitive photon detectors to detect these showers.

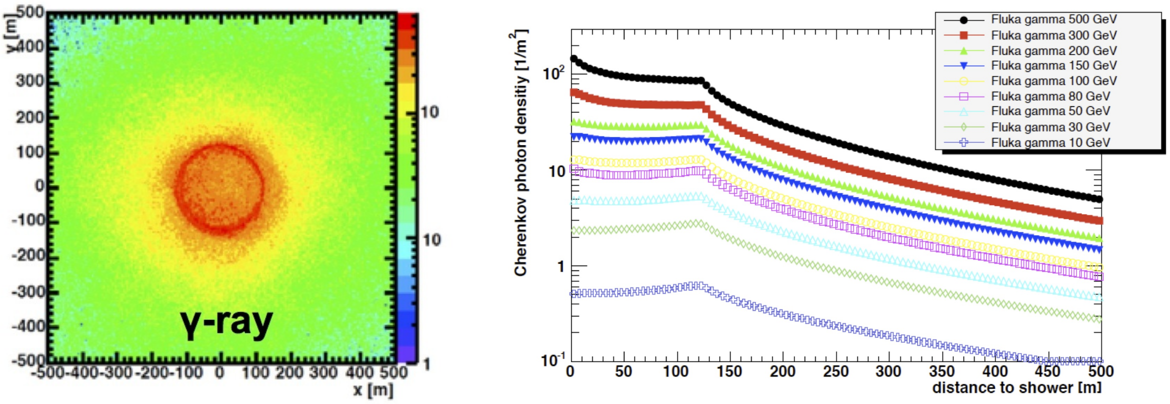

(a) Photons on the Ground

(b) Lateral distribution

Figure 4.7: (a) Simulated Cherenkov photon density at VERITAS ground level (1.3 km a.s.l.) for a 1 TeV primary. The Cherenkov photon density, in units of photons per m^2, are plotted in the color scale as a function of x-y position on the ground in meters. (b) Average lateral distribution for showers produced by primary gamma rays of different energies. Figure from the VERITAS collaboration.

4.2 Imaging Atmospheric Cherenkov Technique

The imaging atmospheric Cherenkov technique uses the atmosphere as a calorimeter for initiating the Cherenkov light that is recorded from high-energy particles [91]. Measurements of the Cherenkov radiation enable us to get information about the initial particles, and enable very-high-energy gamma-ray measurement of astrophysical sources [92].

4.2.1 The Principle

The key components of the imaging atmospheric Cherenkov technique are large light collecting area, because the Cherenkov pool is faint, and fast detectors and electronics, because the Cherenkov flashes are only a few nanoseconds in duration. Because the Cherenkov light image is large in extent on the ground (radius of about 100 m), a coarse segmented mirror system can be used. The key challenge is discriminating gamma-ray-initiated showers from other cosmic-ray showers initiated in the atmosphere. The shower is seen in the cameras as an elliptical image as shown in Figure 4.8, with the major axis providing information about the longitudinal development and the minor axis providing information about the latitudinal distribution of the shower. This shape is a key part of distinguishing gamma-ray showers from proton showers; a gamma-ray shower image will be compact and point to the center of the camera and a proton shower image will be more rounded, less smooth, and will not point toward the center of the camera. The amount of light in the Cherenkov shower is proportional to the energy of the initial particle, so the amount of light collected in an image is used to determine the energy of the primary particle.

Multiple telescope systems allow for stereoscopic imaging of the showers for better background rejection and position reconstruction, as well as larger light collection area for higher effective area and better sensitivity. The telescopes are usually set up with a distance between them that is about the same size as the Cherenkov light pool. The orientations of the images in the cameras can be used to reconstruct the arrival direction of the primary particle. A schematic for a multiple telescope setup is shown in Figure 4.9.

Typical IACTs use photomultiplier tubes (PMTs) in the cameras for the light detectors

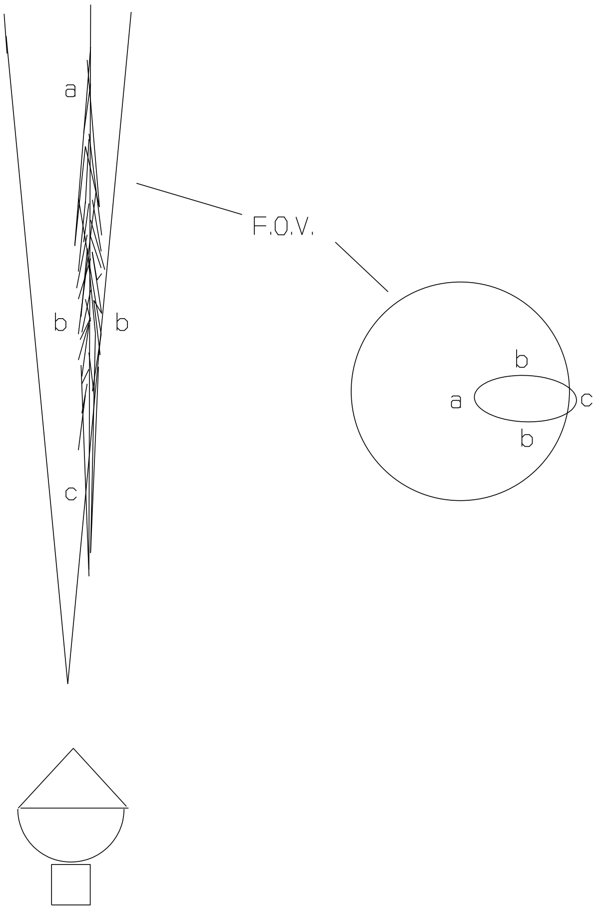

Figure 4.8: Left: the cone of the view of a Cherenkov telescope intersects the core of an air shower. Right: the elliptical image that results in the camera; it is characteristic of a gamma ray [93].

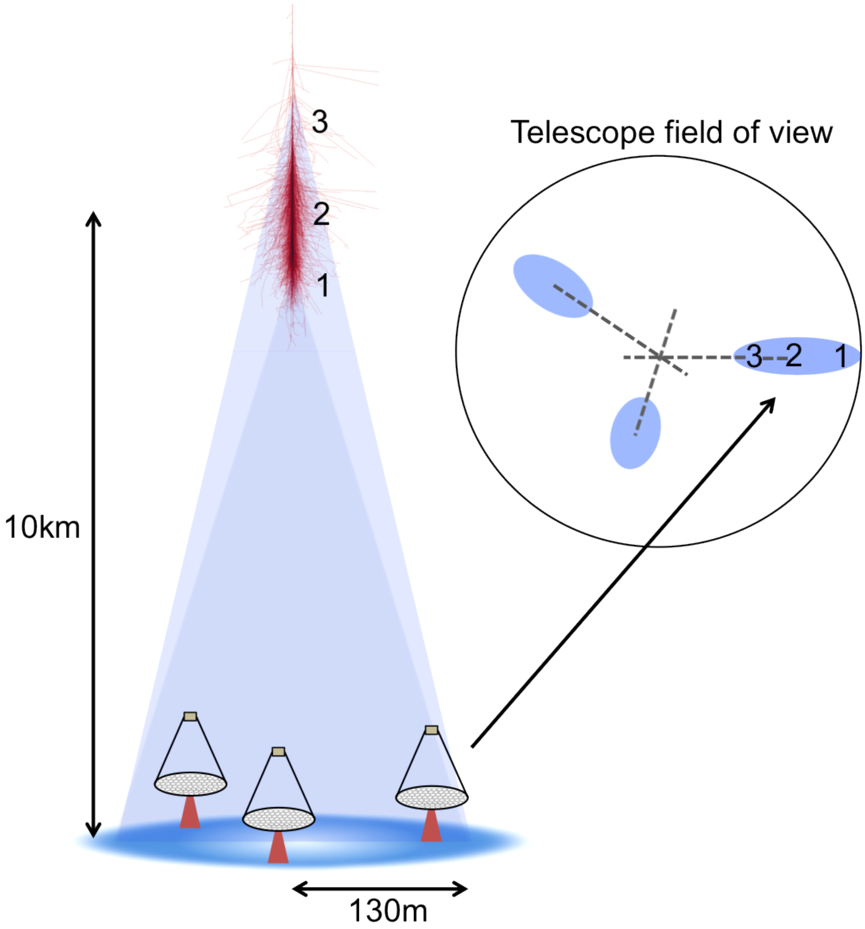

Figure 4.9: A cartoon diagram of a multiple telescope IACT array. Telescopes within the Cherenkov light pool each measure an image of the shower. These images, superimposed on each other on the right, can then be used for direction reconstruction [94].

because of their fast detection capabilities. This, along with fast electronics, is one thing that helps reduce the effects of the night sky background. The night sky background arrives randomly in time and location, while the Cherenkov light pool creates a few nanosecond image. The fast electronics allow experiments to suppress a large amount of the background light in the cameras. Multiple telescopes also simplify the removal of night sky background by requiring triggers in multiple telescopes within a small time window.

4.2.2 Current and Future IACT Facilities

Early detectors developed the key techniques for observing gamma-ray sources over the large cosmic-ray background. The development of the imaging technique by (Whipple [11]) and the stereoscopic technique (HEGRA [8]) were critical for developing the current generation of IACT experiments (VERITAS, H.E.S.S. and MAGIC). Early experiments detected only a few sources. The most prominent early source was the Crab Nebula whose integral flux at 1 TeV, $\sim 2\times10^{-11}$ cm^{-2}s^{-1} [95] is now used as the standard reference for TeV source strength. These experiments are compared in Table 4.1. In the future, the Cherenkov Telescope Array (CTA) will build and improve on the current generation of IACTs.

Table 4.1: Physical characteristics of two previous, and three current, IACT facilities. H.E.S.S. II is the fifth, larger, telescope in the middle of the H.E.S.S. array. Adapted from [96].

Instrument	Location	Telescopes	Mirror area (m^2)	Pixels per camera	Field-of-View (°)
Whipple	Arizona	1	75	379	3.2
HEGRA	Canary Islands	5	8.5	271	4.3
H.E.S.S. (II)	Namibia	4 (+1)	$\sim$ 100 ($\sim$ 600)	690 (2048)	5 (3.2)
MAGIC	Canary Islands	2	$\sim$ 200	1039	3.5
VERITAS	Arizona	4	$\sim$ 100	499	3.5

The major experiments of the current generation of IACTs are: VERITAS, used in this dissertation and detailed in Chapter 5, H.E.S.S. in Namibia, and MAGIC, on the Canary Islands. They each have multiple large telescopes, allowing for stereoscopic imaging. They also use PMT cameras with fast electronics to collect Cherenkov images. This generation of instruments can detect TeV sources having fluxes less than 1% Crab Nebula flux in about 25 hours of observations.

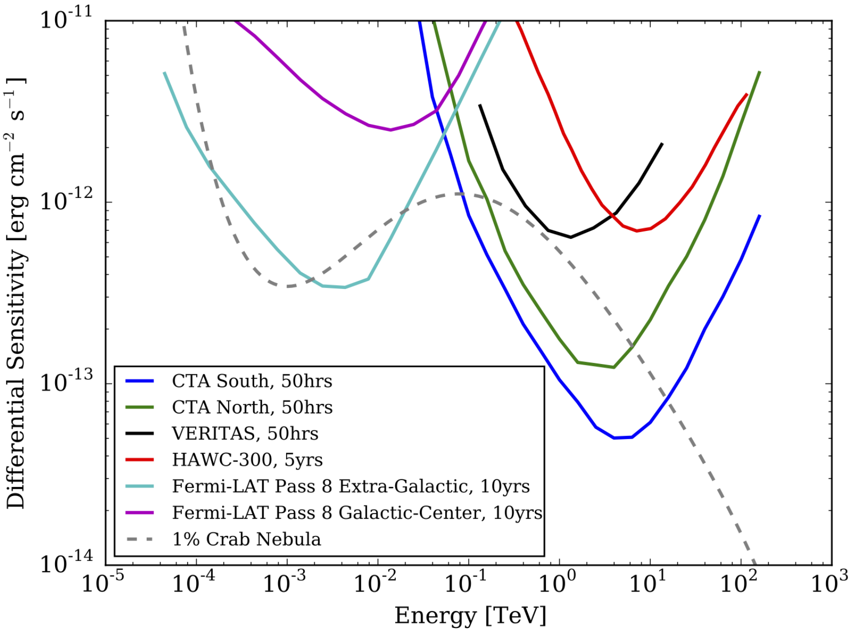

Figure 4.10: The improvement of differential sensitivity of present and future gamma-ray telescopes. Also plotted are the sensitivities of *Fermi*-LAT and HAWC. [13, 14, 16, 19, 97, 98]

The current generation of IACTs has laid the foundation for CTA and they have demonstrated the wealth of gamma-ray sources. CTA will be able to utilize new technologies such as silicon based photomultiplier detectors, as well as improve on the current technologies. This will result in an increase in sensitivity of a factor of five to ten in the 100 GeV to 10 TeV range. CTA plans to undertake survey observations of the inner Galaxy from the southern site, in Chile, and of the outer Galaxy, including the Cygnus region, from the northern site, on the Canary Islands. The improvement in sensitivity over the current generation of IACTs is shown in Figure 4.10.

CHAPTER 5

VERITAS

The Very Energetic Radiation Imaging Telescope Array System (VERITAS) is an array of four 12 m diameter imaging atmospheric Cherenkov telescopes (IACTs) located at the Fred Lawrence Whipple Observatory in southern Arizona (31°40' N, 110° 57' W, 1.3 km a.s.l.); see Figure 5.1 [12]. Each telescope has a camera made up of 499 photo-multiplier tubes (PMTs) with a 3.5° field of view. VERITAS can detect gamma rays at energies of 85 GeV to >35 TeV with an energy resolution of 15-25%. The pointing accuracy of the array is better than 50", and the angular resolution per photon with a 68% containment radius is 0.1° at 1 TeV. VERITAS began four-telescope operations in 2007 and has undergone a number of upgrades. These include a telescope move in 2009 that improved the geometry of the array, a trigger upgrade in winter 2012, and a camera upgrade in the summer of 2012. All of these upgrades have improved the sensitivity and lowered the energy threshold of the array [99, 100]. The current VERITAS configuration is able to detect a source with 1% Crab Nebula flux in about 25 hours of observations [97]. In Section 5.1 the hardware aspects of the array are discussed, followed by a discussion of the camera upgrade in Section 5.2. The chapter concludes with a discussion of VERITAS calibration and data analysis in Section 5.3.

5.1 The VERITAS Array

The four VERITAS telescopes are comprised of identical optical systems (mirrors, support structures, and tracking), cameras, trigger systems, and data acquisition systems.

(a) Before T1 Move

(b) After T1 Move

Figure 5.1: The VERITAS array before (a) and after (b) the move of one of the telescopes in 2009. It was moved to improve the array geometry by making the distances between the telescopes more uniform ($\sim$ 100m). Image credit: The VERITAS Collaboration http://veritas.sao.arizona.edu/.

5.1.1 Telescopes

Each telescope consists of a tubular steel optical support structure (OSS) and has a commercial altitude-azimuth positioner. The positioner is capable of slewing the telescopes at operating speeds of about 1° per second to an accuracy of better than 0.01°. 345 hexagonal mirrors are mounted onto the OSS to form a 12 m diameter mirror with a reflecting area of about 115 m^2, arranged according to a Davies-Cotton design (which consists of an area of spherical mirrors arranged on an approximate surface so that all of the images are superimposed at the camera) [101]; see Figure 5.2. Because there is no protection from the weather, the mirrors are continuously re-coated so that on average the mirrors are replaced every three to four years [102]. The mirrors have an average reflectivity of 85% over the Cherenkov wavelength range of 250-450 nm and better than 90% at 300 nm (see Figure 5.3). The mirrors are manually aligned periodically to keep the optical point spread function (PSF) of the telescopes to better than 0.05° at operational elevations [103]. Four arms support the camera at the focus of the mirrors, with a mechanical bypass to transfer the load of the camera to counter weights.

5.1.2 Cameras

The cameras, located at the focus of each telescope, consist of 499 PMTs; see Figure 5.4 (a). The upgraded PMTs, Hamamatsu R10560-100-20 MOD, are UV sensitive with a fast rise time (1.9 ns) and a good quantum efficiency (37% at 330 nm). A comparison with the previous PMT is in Section 5.2. In front of the PMTs are modified Winston-style light cones that concentrate light from the mirrors onto the PMTs. The light cones reduce both the dead space between pixels and reject some background light; see Figure 5.4 (b). A multi-channel high-voltage power supply powers each pixel, and has the capability of setting each pixel's voltage individually. Each pixel can thus be adjusted so that its photon response is nearly uniform. The process for measuring differences in the timing and gain between pixels is discussed with the nightly calibrations; detailed in Section 5.1.5. The PMTs are operated at a typical voltage of around 800 V and are set to result in a nominal gain of 2×10^5. The

Figure 5.2: A close up of the hexagonal VERITAS mirrors. Each is mounted on three adjustable mounts which allow for manual mirror alignment.

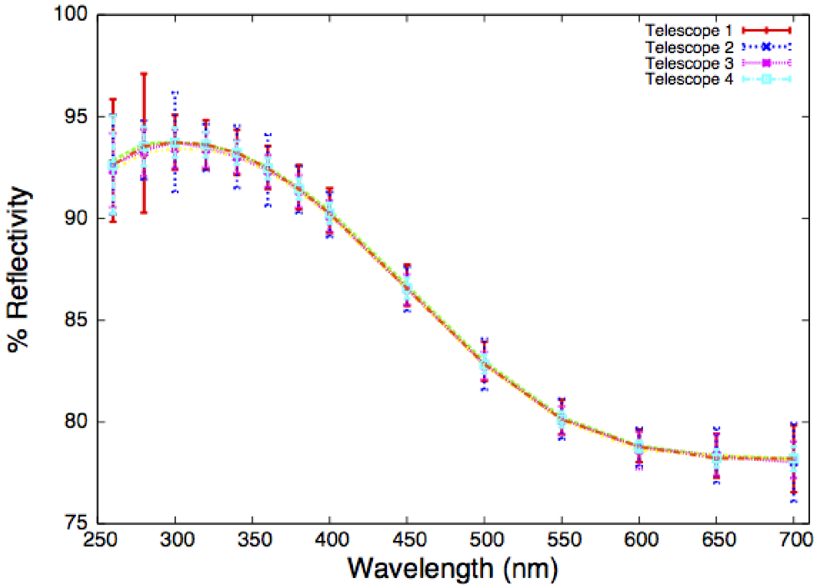

Figure 5.3: The reflectivity of the VERITAS mirrors versus wavelength. The mirror reflectivity from 250-450 nm is better than 90%, with a peak around 300 nm [102].

post-upgrade PMTs have $\sim 1.5\times$ the gain for the same set voltage when compared to the pre-upgrade PMTs and they are set at a lower voltage to maintain the same nominal gain. In the base of each PMT, a high bandwidth pre-amplifier provides an extra gain of about 6 to the PMT signals. These signals are fed into the VERITAS trigger and data acquisition system diagrammed in Figure 5.5, described in detail in the next sections.

5.1.3 Trigger

Signals from the pre-amplifiers are sent into the VERITAS three-level trigger system, which is used to detect Cherenkov flashes of light resulting from gamma rays and cosmic rays, as well as to suppress the signal of background night-sky photons and muons. The system is explained in detail in [104]. The first level (L1) of the trigger system is at the pixel level and triggers when the pulse in a pixel rises above a set threshold. It uses a constant fraction discriminator (CFD) to set the trigger level in the presence of varying night sky background (NSB). For dark-sky observations the CFD is typically set to 45 mV, which corresponds to about 4-5 photoelectrons. Level 2 (L2) operates at the camera level and triggers when three adjacent pixels trigger the L1 within six nanoseconds. The last trigger, level 3 (L3), operates

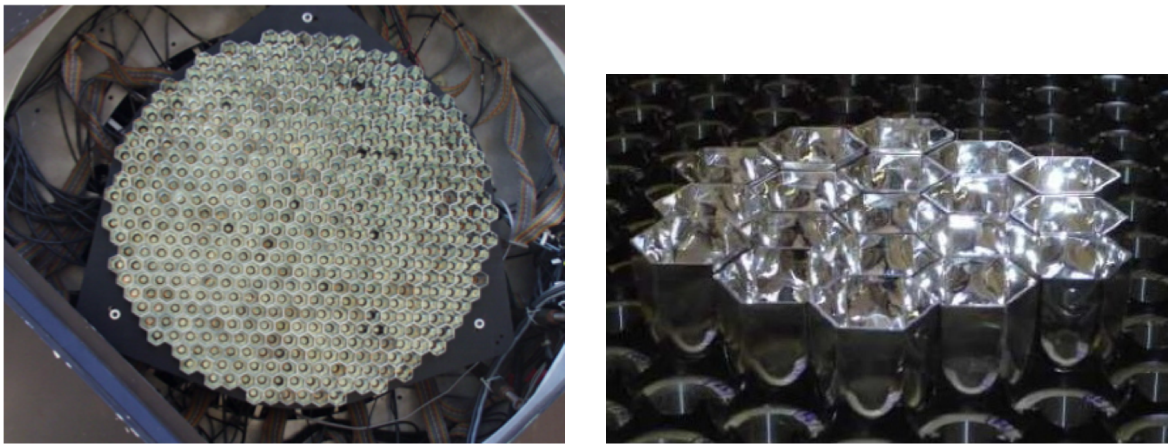

(a) Camera Face (b) Lightcones

Figure 5.4: The VERITAS camera at the focal plane (a) with the lightcones in front of the 499 PMTs along with a detail of the lightcones (b). The hexagonal lightcones fill in the gaps between the PMTs and reduce background light.

at the array level and requires a time coincidence between the L2 triggers of two cameras in the array within a 50 nanosecond time window. Events that satisfy all three triggers are read out by the data acquisition system and are archived for analysis. Analysis of the images in the camera is undertaken to determine the primary characteristics of an event for doing background rejection, energy determination, and source localization as part of the analysis procedure. The image reconstruction analysis is discussed in Section 5.3.3.

Bias curve calibration data is used to set the L1 trigger level by scanning over a range of CFD levels and recording the L3 trigger frequency. A sample bias curve is shown in Figure 5.6. At a low trigger level, the NSB dominates the triggered readouts at a very high rate, increasing the deadtime of the array and setting off accidental L1 triggers. At a certain point, depending on night sky conditions, the triggers from cosmic rays begin to dominate, and the rate is lower. The ideal trigger threshold is that which is set to maximize cosmic-ray triggers without increasing the deadtime of the array. The CFD level is changed depending on the observing conditions; for example, higher in response to the presence of moonlight or in dark fields of the sky where a low energy sensitivity is desirable. Typical settings, for common observing modes, are in the 20-60 mV range.

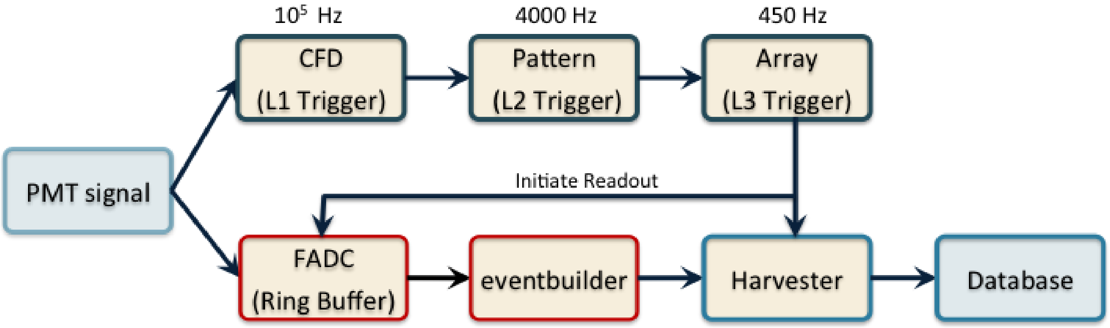

Figure 5.5: Diagram of the trigger and data acquisition systems for VERITAS. The analog PMT signal is split with one part going to the three level trigger system (top) and a copy going to the data acquisition system (bottom). The typical rate of each trigger is displayed above the relevant box. In the data acquisition system the PMT signal is digitized and stored in a ring buffer until the signal from the array level trigger initiates the readout. The eventbuilder combines the signals from the other PMTs and telescopes into a single event. The event is then written to a database and archived.

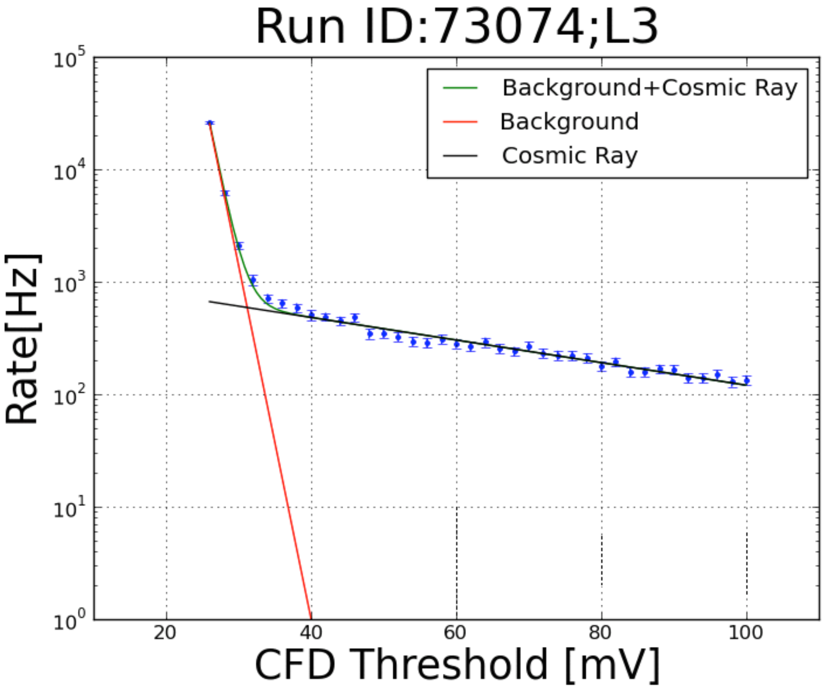

Figure 5.6: A VERITAS bias curve. The L1 (CFD) trigger level is changed from 25 to 100 mV and the L3 trigger rate is measured. At lower trigger levels NSB dominates, and the slope changes when the background triggers are suppressed and then cosmic-ray triggers dominate.

5.1.4 Data Acquisition

The data acquisition system is diagrammed in Figure 5.5. 500 megasample-per-second flash analog-to-digital converters (FADCs) continuously digitize the analog signals from the PMTs [105]. For each PMT channel, buffer holds the FADC signal while awaiting an L3 trigger signal. When the L3 signal is received, the DAQ system reads out the FACD buffer, usually 32 to 48 ns in length. A telescope level eventbuilder collects the telescope events and then passes them to an array level harvester. The harvester stores the events in a custom VERITAS data format for storing to disk. Additional information, such as notes about the observation conditions and target information, are recorded to a database for each run. This information is used alongside next-day quality plots are used for data-quality selection, discussed in Section 5.3.1.

5.1.5 Observations

VERITAS takes data on clear, dark nights under low or moderate moonlight from September through June, with a break in the summer for the monsoon season. This results in about 900 hours of dark-time data per year, plus a few hundred more hours of reduced-high-voltage data per year. Standard observations are undertaken in "wobble mode," in which the pointing of the telescopes is offset from the source position by 0.5°. The wobble direction is set to correspond to a cardinal direction. Each data run is about 15-30 minutes long, with long term observations getting runs of 20-30 minutes and snapshot blazar targets getting 15-minute runs. The wobble position is changed for each data run on a given source, or a new source is pointed at after the data run concludes. Moonlight observations are taken when the Moon is above the horizon. A reduced-high-voltage (of 81% of nominal operating voltage) is used when the currents in the PMTs are higher than 15 μA (typically when the Moon is more than about 35% illuminated).

For the VERITAS Cygnus region survey data were taken on grid pointings over a 15° by 5 ° region covering from 67° to 82° in Galactic longitude and from -1° to 4° in Galactic latitude. The grid observations are separated by 0.8° in Galactic longitude and by 1.0° in Galactic latitude to allow for substantial overlap in the field-of-view of grid points. Approximately one hour was taken on each grid point yielding a base exposure of 6-7 hours over the region. A further discussion of the Cygnus region survey data can be found in Section 7.1.

Observations are scheduled based on a plan put together by the VERITAS Time Allocation Committee (TAC). The yearly plan includes long-term targets established in 2011 by the science working groups, along with observing proposals submitted annually. It is the duty of the TAC to rank the targets from the long-term plan, proposals, and target of opportunity observations. The targets observed include Galactic sources (such as SNRs, PWNe, pulsars, and binaries), possible sources of dark matter (such as dwarf galaxies and the Galactic center), and extragalactic targets (such as gamma-ray bursts, galaxy clusters, and active galaxies). A recent overview of VERITAS science highlights is presented in [106].

Weather Monitoring

Because the light yield of Cherenkov photons on the ground is affected by local weather, like clouds and haze, the atmospheric conditions are monitored during observations. The first line in weather monitoring are the observers on the site, who can look outside at conditions. The monitoring instruments on site include: an infrared sky temperature monitor, a weather station, and a laser-based cloud backscatter monitor, as well as a CCD camera pointed at the sky. The sky temperature is monitored using three infrared pyrometers (one on Telescope 2, one on Telescope 3, and one pointed straight up) that measure the infrared emission in a range (8 μm to 14 μm), where the sky does not radiate, but where water vapor and droplets in the sky do. A higher temperature corresponds to more water in the atmosphere. This information is displayed in real time for the observers. An array of weather monitoring instruments allows real-time monitoring of the temperature, humidity, wind speed, and rainfall at the observatory. A light detection and ranging instrument (LIDAR) is installed at the observatory to measure the backscattered light from short laser pulses as a function of time. The LIDAR measures the height, concentration, and distribution of dust, fog, haze, rain, and clouds in the atmosphere. The infrared pyrometers, weather, and LIDAR data are also saved to an offline database. Finally, a CCD camera with a fisheye lens allows for optical monitoring of the night sky by the observers. This information informs the observers about the conditions on a given night. The data saved to the database are also critical for determining data quality, discussed in Section 5.3.1.

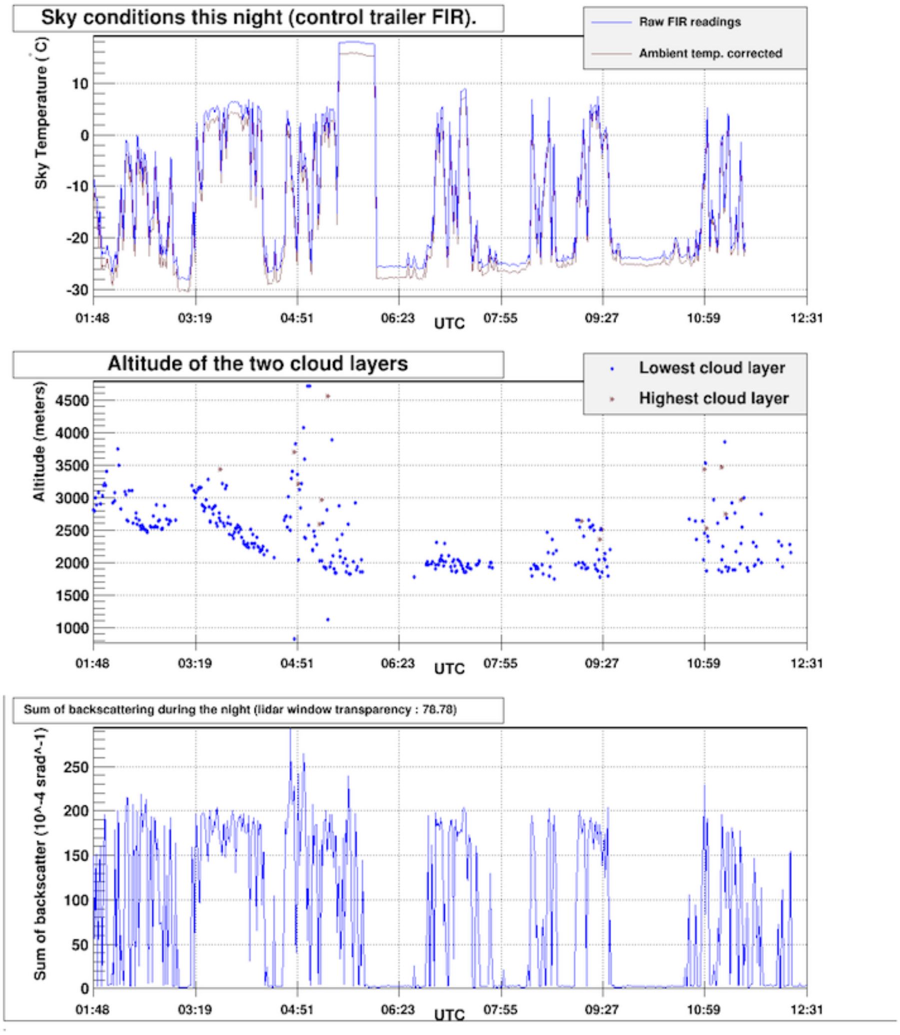

Figure 5.7: Weather data from a cloudy night at VERITAS. The top panel shows the output from the infrared sky temperature monitor, the middle panel shows the output from the LIDAR measurement of the height of the clouds, and the bottom panel shows the LIDAR measurement of the transparency of the clouds.

Calibrations

A large number of measurements are undertaken regularly to maintain the stability of the experiment and, while not discussed in detail, are listed here. These calibrations and monitoring of the VERITAS experiment and subsystems are scheduled either nightly (flasher), monthly (reflectivity, single photoelectron (PE), bias curves, high/low gain calibration), each season (channel mapping), or as needed (mirror alignment, camera gain flat-fielding, and L2 timing). Some of these measurements can be done in bad weather and therefore do not affect regular data taking.

A key nightly calibration is the flasher, used for inter-pixel calibration [107]. The telescopes are pointed at a dark patch of the sky, and a dedicated 2-5 minute run is taken with a fixed trigger readout, while a system lights several LEDs pointed at the cameras. This can be used to measure relative timing differences and these corrections are relative gains between the pixels and is applied in the analysis (Section 5.3.3). When the RMS of the relative gains is larger than about 10% the PMT voltages are adjusted, in a procedure called flat-fielding, making the PMT response to the flasher light uniform. The calibrations are also used to relate the traces of the PMT pulses measured in digital counts (dc) to the number of photoelectrons (pe), typically the ratio of dc/pe is ≈ 5.4. The PMT response depends on a number of factors including the wavelength of the light it measures and the gain of given pixel.

5.2 The VERITAS Camera Upgrade

In summer 2012, the VERITAS cameras were upgraded with new PMTs and pre-amplifiers [100, 108]. The newer PMTs were selected for improved quantum efficiency (see Figure 5.8), which would therefore lower the energy threshold and increase the sensitivity of the array by increasing the photon collection efficiency by 50%. During that summer, the old cameras were disassembled (with PMTs and current monitoring boards removed from cameras) and then the new PMTs were assembled, tested in a black box to determine if there were any poor connections, and installed in the cameras. Then the new PMTs were tested in the array following the start of season procedures. The new PMTs resulted in the immediate improvement of fewer dead pixels; see Figure 5.9. A number of studies using the Crab Nebula were undertaken to confirm the increased sensitivity and lower energy threshold (see Figure 5.10). The sensitivity of the array was improved by about a factor of 2 over V4 at the lowest energies. Furthermore, the analysis energy threshold was reduced from 150 GeV to 85 GeV.

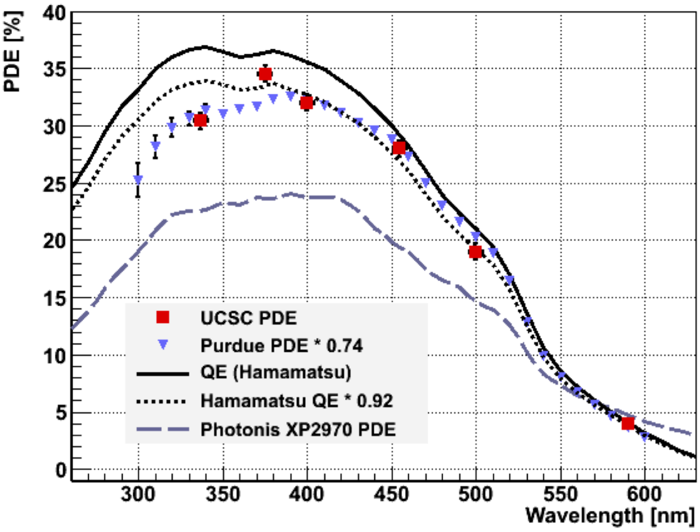

Figure 5.8: The quantum efficiencies of the pre- and post- upgrade PMTs as a function of wavelength. The post-upgrade PMTs (The solid and dotted lines come from the manufacturer, the red and blue points are measurements by the VERITAS collaboration) are clearly more efficient at the optical wavelengths utilized by VERITAS to observe Cherenkov light. The efficiency of the old PMTs is shown by the dashed line. Figure from [108].

5.3 VERITAS Data Analysis

The VERITAS collaboration uses two data analysis packages; VEGAS (VEritas Gamma-ray Analysis Suite) and eventdisplay (ED). The VERITAS plots in this dissertation are generated using ED, unless otherwise noted. The analysis procedure with ED is outlined in this section. ED was developed by Gernot Maier (DESY) and Jamie Holder (University of Delaware) for the VERITAS prototype and it has since been developed into a complete analysis package. The analysis procedure with VEGAS is similar, but will not be discussed

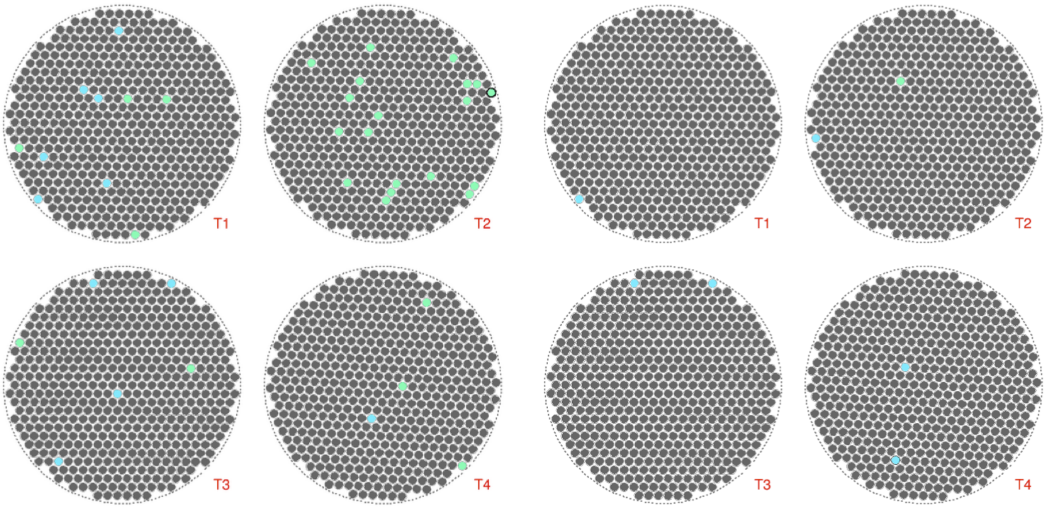

Figure 5.9: The dead channels pre- (left), and post- (right) PMT upgrade for each camera (TX, where X ranges from one to four is the label given to each telescope). The good channels are in gray, with dead channels in light blue [100].

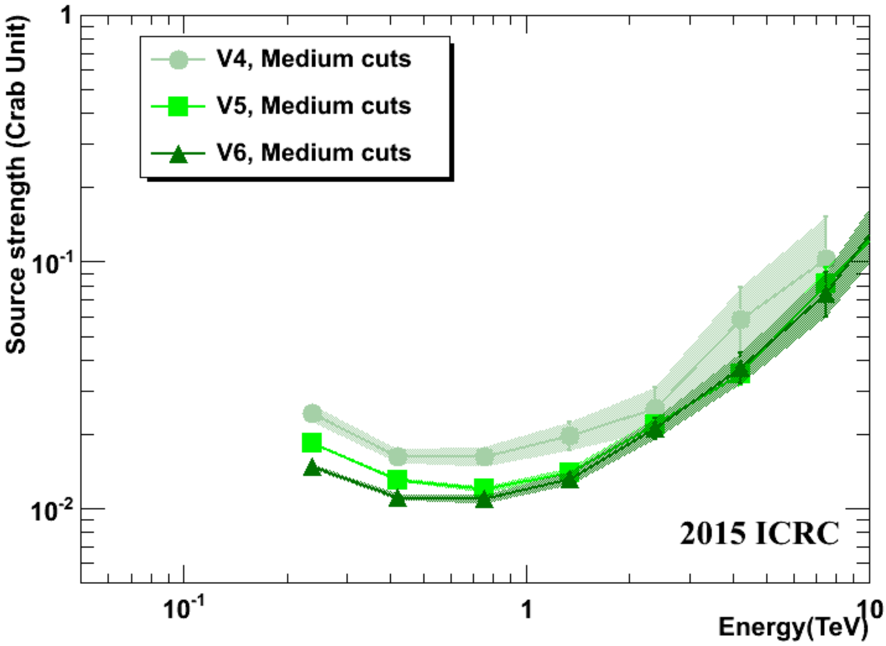

Figure 5.10: A plot of the the VERITAS array sensitivity for different phases of the experiment. V4 refers to the original array configuration, V5 to the array post-T1 move, and V6 to the array with the camera upgrade. The source strength is calculated as a percentage of the flux of the Crab Nebula in a given energy bin such that the source would be detected with 5σ significance after 50 hours of observing time. Figure from [97].

in detail; a discussion can be found in [109]. Every VERITAS analysis is done independently with each analysis package, and the results are cross checked.

5.3.1 Data Quality

The first step in undertaking VERITAS analysis is picking good-quality data. All the data collected are sent through an early analysis to produce plots picked to highlight any problems with the data. Everything is assessed in next-day data quality monitoring (DQM); this gives an initial cut on quality and has been a valuable tool for the early diagnosis of problems with the array. Cuts to the data can also be assigned by the DQM process. Examples of these cuts for data quality include: time cuts for a cloud passing in front of the cameras, or telescope cuts for a telescope with a tracking error. On top of this early assessment, all data used in this dissertation were checked to meet the weather and operation quality standards (detailed in Section 7.1).

5.3.2 Simulations

There are two levels of Monte Carlo simulations used to understand VERITAS data. One is for the air shower development and Cherenkov light; the other is for the detector response. The shower development simulation package used is CORSIKA [6] version 6.960, using the parameters of the VERITAS site, as well as the IACT option that saves Cherenkov photons that cross a fiducial sphere around the detector position. The detector simulation is done with a package developed by VERITAS called GrISU [110].

The density of Cherenkov photons on the ground depends on the energy of the primary particle, the height of its initial interaction, the angle of the shower, and the local geomagnetic field. The range in energies of the simulated primary particles is 30 GeV to 200 TeV, following an E^{-2} differential flux spectrum. The energies are weighted during the analysis procedure to account for a different spectral shape of the potential source. The shower simulations cover a range of VERITAS observation zenith and azimuthal angles to represent the shower angle and they cover geomagnetic effects. Corrections based on winter and summer atmospheric profiles, based on average FIR measurements, are applied after the shower simulation.

The GriISU package handles the propagation of Cherenkov photons through the optics of the VERITAS telescopes, as well as the response of the PMTs and electronics. The final output of the simulations can then be analyzed in the same way as data, and can be used to validate event reconstruction, compare analysis packages, and determine the instrument response functions for flux measurements. The systematic uncertainty from the detector simulations is about 15%. The resulting flux uncertainty is about 20%.

5.3.3 Image Parameters

The first step in the analysis is to characterize the images saved by the trigger system. This is done by analyzing the FADC signals (trace analysis), cleaning the image in the camera, and then determining the parameters that describe the shape and orientation of the image in the cameras. The shape parameters are called the Hillas parameters and are described below.

Trace Analysis

At the FADC trace level, the analysis separates a pixel signal with a PMT pulse (Figure 5.11(a)) from a pixel signal that is consistent with NSB fluctuations, that is consistent with noise around the pedestal level (Figure 5.11(b)). This pedestal is a negative offset added to the analog signals. The pedestal level is determined by reading out the FADC traces at a 1 Hz rate during standard data taking. It is typically about 16 digital counts (dc). The signal pulse is characterized by a fast rise time and a slow decay back to the pedestal level. T_0 is the time where it has risen to half of the maximum pulse height and is known as the arrival time. The measurement of charge in the pixel is done by summing the signal from the FADC trace within a time window, subtracting the pedestal level, and applying the gain corrections as measured by the nightly flasher calibrations.

A short time window for summing the trace is used to minimize the contribution of NSB photons. This is done in two timing stages. In the first, a wide integration window

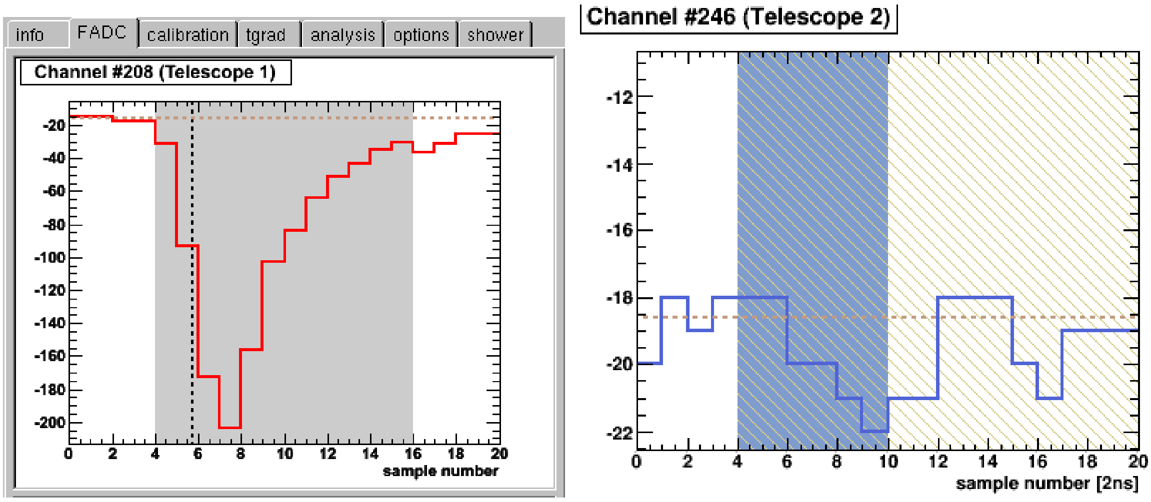

(a) Pulse

(b) Night-Sky Background

Figure 5.11: (a) An FADC trace with a significant light pulse and (b) a trace without a pulse (consistent with NSB) in digital counts versus time. The NSB trace shows fluctuations around the pedestal level; note the smaller y-range. The sampling rate is 500 MS/s. The horizontal dashed lines represent the pedestal level. The vertical dashed line on (a) indicates T_0. The gray shading indicates the summation window. The ratio of dc/pe is ≈ 5.4.

(18 samples) is used to calculate the charge and arrival time of each signal. Then the image cleaning discussed next is applied. In the second timing stage, a short window (7-12 samples) is placed on each signal, with the position determined with the temporal evolution of the shower taken into account.

Image Cleaning

The goal of the image cleaning is to determine which pixels are likely to be part of the shower image and cut out pixels which are likely to be NSB photon signals. First the RMS variation of the pedestal values (pedvar) over a few-minute time window is determined to characterize fluctuations in the NSB. Then a two-stage cut on pixels is used to identify *image* and *border* pixels. *Image* pixels are those with a charge greater than five times the pedvar, and the *border* pixels are those with a charge greater than 2.5 times the pedvar and having at least one bordering *image* pixel. *Image* pixels with no neighboring *image* or *border* pixels are also removed. The pixels that remain (*image* and *border* pixels) are then used as the image of the Cherenkov shower. An example of cleaned images for a four telescope event is shown in

Figure 5.13.

Hillas Parameterization

The final step in the image analysis is to determine the parameters that define the Cherenkov shower image; they are shown schematically in Figure 4.8. The standard method is based on the Hillas parameters [111]. These typically include: the zeroth order, the sum of all charges after image cleaning, the first order, which describes the position of the image, and the second order, describing the extent of the image. These are calculated using the formulas in [112]. The geometry of typical image parameters is displayed in Figure 5.12 and the definitions for parameters utilized in the VERITAS analysis are provided in Table 5.1.

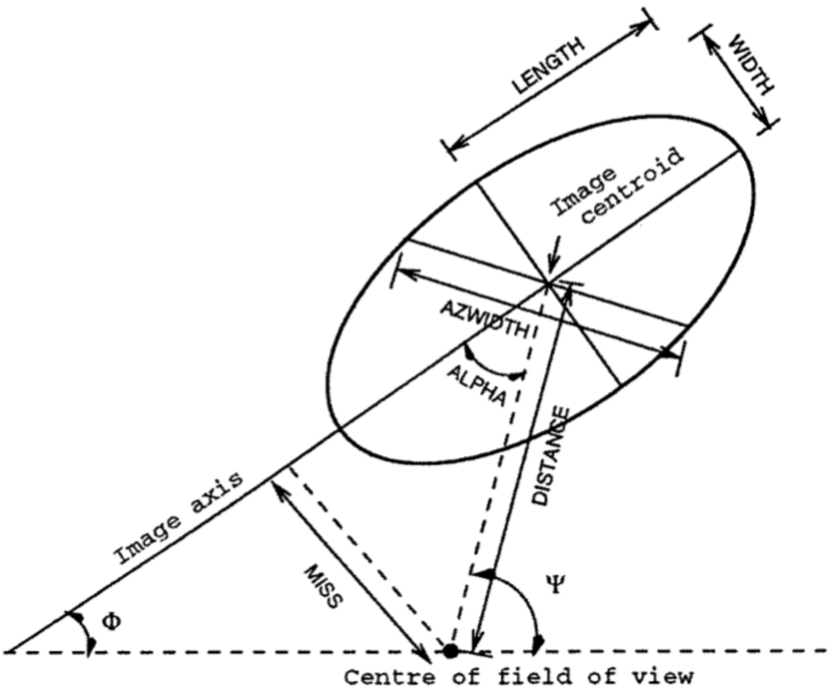

Figure 5.12: The Cherenkov image in a camera is represented by an ellipse with the width and length determined from the extent of the image along the the semi-minor and semi-major axes respectively. The distance, alpha, and miss parameters provide the orientation and position of the image in the camera. The azwidth combines the position and extent of the image [112].

Table 5.1: The definitions of the Hillas parameters.

Size	The sum of the integrated charge in pixels that are part of the image (in either dc or photoelectrons), related to the primary particle energy
Width	The RMS spread of the light along the minor axis of the image, related to the projected lateral development of the shower
Length	The RMS spread of the light along the major axis of the image, related to the projected vertical development of the shower
Distance	The distance of the centroid of the image to the center of the field of view of the camera
Loss	The fraction of the image size contained in edge pixels

All of the preceding steps to determine the image parameters are run on each telescope individually. The image cuts and other analysis cuts for the analysis in this dissertation are discussed in Section 5.3.5. The overall array level event reconstruction is discussed in the next section.

5.3.4 Event Reconstruction

Quality cuts are applied to images that are to be analyzed. These include: a minimum number of *image* and/or *border* pixels per telescope (typically $N > 4$), a minimum image size (size > 400 dc), and a maximum loss value (loss < 0.5). These values were optimized by the collaboration using Crab Nebula data where the Crab Nebula flux was scaled to 5% of its nominal value. There is a further requirement that two or more telescopes have images; this requirement can be increased to three or four telescopes, if needed for an analysis, for better event reconstruction at a cost of energy threshold. For the purposes of the work in this dissertation, we have chosen the three telescope requirement because of the improved event reconstruction.

Next is the reconstruction of the directional information for the event using the stereoscopic information provided by two or more telescopes having an image; see Figure 5.13 (a). The goal is to reconstruct the direction of the shower, the shower core location, and the height of the shower in the atmosphere. The method for determining the direction of the shower is based on algorithm 1 presented in [113]. Each of the shower images is superimposed on a single camera coordinate system (see Figure 5.13 (b)). Then the image axes from the Hillas parameterization are intersected for each pair of telescopes with that image and the location of the shower core is the position given by the weighted average of each intersection; see Figure 5.13 (c). The weights include the sine(s) of the angle between image axes, the sizes of the images, and the ratio of width over length; these are intended to give more weight to bright, elongated image pairs.

The shower core is needed for the energy reconstruction and gamma-hadron separation. It is defined in a plane perpendicular to the shower arrival direction and corresponds to where the shower would have hit the ground. A reconstructed image in the ground coordinates is shown in Figure 5.13 (c). The impact parameter is defined as the distance from the shower core to each telescope. Distant showers tend to produce images that are parallel to each other and the angular resolution is worse for showers with large impact parameter. The analysis employs a cut on shower core position of 250 m from the center of the array to reduce the systematic uncertainty associated with poorly reconstructed air showers.

The shower emission height, defined as the point in the shower with the maximum number of Cheronkov light emitting particles, is calculated using a weighted mean of image size. The σ (error) of the mean is also determined. Both parameters can be used for removing background showers because both hadronic showers and single muons penetrate into the atmosphere more deeply than gamma rays, especially at lower energies.

The energy reconstruction relies on the fact that the number of Cherenkov photons in the air shower is related to the energy of the initial particle. This means that the energy is related to the sizes of the images. The number of Cherenkov photons in a shower can vary with observing conditions, such as: telescope pointing, shower impact parameter, and the NSB. Simulations covering the parameter space allow the energy to be estimated using a lookup table, i.e. a file with the median and the 90%-width error of the logarithm of the image size versus gamma-ray energy and impact parameter; see Figure 5.14. Because the lookup table has discrete bins, an interpolation is used for values in between bins.

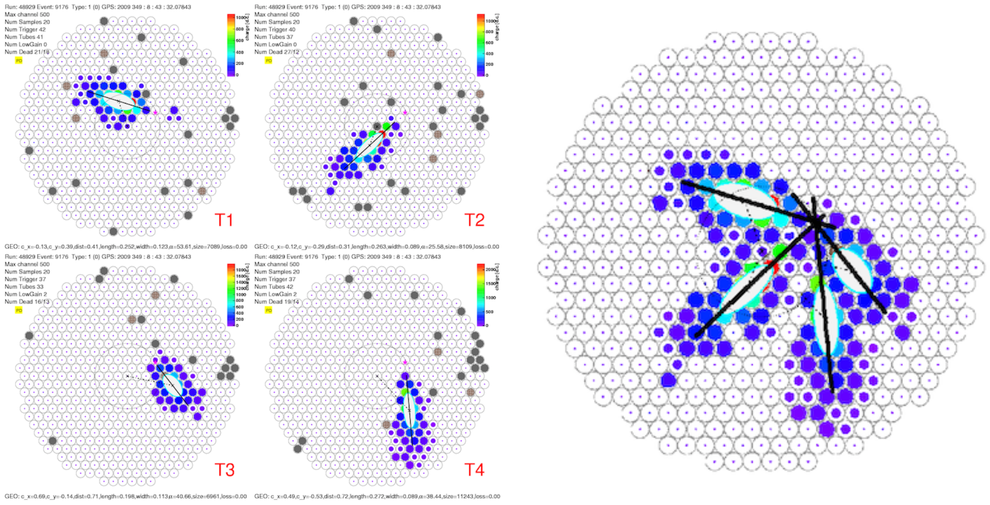

(a) 4-telescope event

(b) Sky coordinates

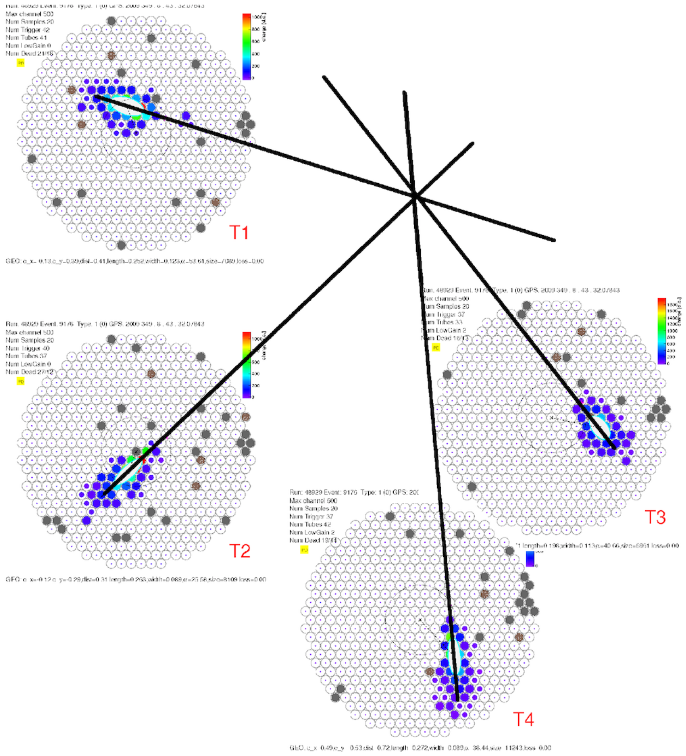

(c) Ground coordinates

Figure 5.13: An example of a four telescope event in VERITAS: (a) shows the images in each camera, (b) shows the images in the sky coordinates (in which the images are superimposed for determining the source position), and (c) shows the images in the ground coordinates (in which the they are placed at the positions of their relative telescopes; this is used for determining the impact parameter). The image cleaning can be seen in the camera figures, triggered pixels which do not meet the *image* or *border* criteria are grayed.

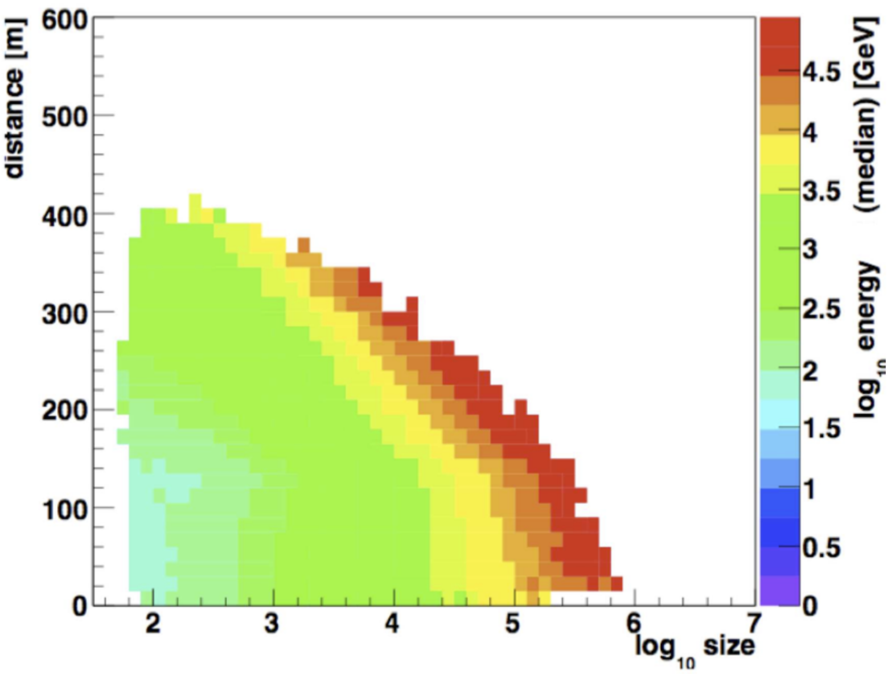

Figure 5.14: An example of a lookup table for the log of the median energy (color scale) of the reconstructed event from simulations plotted against impact parameter (distance [m]) and size (in dc). At low energies, the number of filled bins is limited by the requirements of number of pixels per image. At high energies the filled bins are limited by the Monte Carlo statistics and the camera size.

5.3.5 Gamma-Hadron Separation

With the reconstruction of the parameters for each event, the next goal is to separate gamma-ray showers from hadronic showers which are described in Section 4.1. The primary cut used is on the "shape" parameters of the image, as described by the width and length Hillas parameters. These each depend on the energy of the initial particle, the shower parameters (direction and impact parameter), and the NSB. Simulations are again used to produce a lookup table of the median and 90%-width error of the width $(w_{MC}, \sigma_{width,MC})$ and length $(l_{MC}, \sigma_{length,MC})$ parameters versus impact parameter, R, and image size, s. Then the mean-scaled width and mean-scaled length are calculated using:

$$MSCW = \frac{1}{N_{images}} \sum_{i=1}^{N_{images}} \left(\frac{width_i - w_{MC}(R,s)}{\sigma_{width,MC}(R,s)} \right) \tag{5.1}$$

and

$$MSCL = \frac{1}{N_{images}} \sum_{i=1}^{N_{images}} \left(\frac{length_i - l_{MC}(R,s)}{\sigma_{length,MC}(R,s)} \right) \tag{5.2}$$

where i is the sum over the telescopes with images and N_{images} is the total number of telescopes with an image. In this definition the MSCW and MSCL for gamma-ray showers are normally distributed and centered at zero. Hadronic showers are more irregular and more spread out and so their parameters are longer and wider than those of a gamma-ray shower (see Figure 5.15). The values for the cuts that are used to separate gamma-ray and hadron initiated showers are determined by simulations. In the case of *moderate* cuts, they are optimized to detect a source with a 5% Crab Nebula flux. Examples of the image quality and *point* source cut parameters are described in Table 5.2.

A cut on the square of the arrival direction, θ, or the square of the angle on the sky between the source position and the reconstructed direction, is used to cut out the nearly isotropic cosmic-ray background. If an arrival location is far from the source location than there is a greater chance that the event is not a gamma ray emitted by that source. The value depends on the analysis, with a value of $\theta^2 < 0.008$ for a *point*-source analysis and a

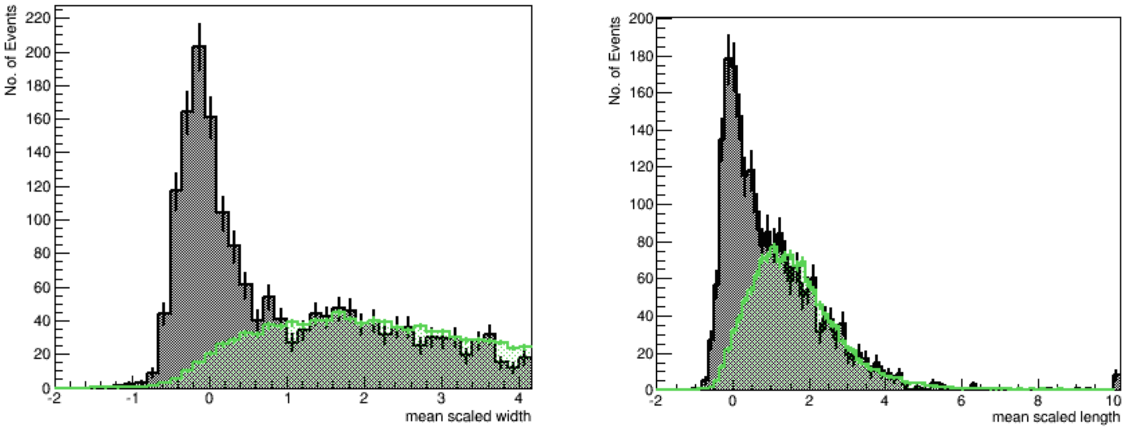

(a) MSCW

(b) MSCL

Figure 5.15: Distribution of mean-scaled parameters from events taken from a Crab Nebula run. The black-shaded distribution shows events in the ON region, with a peak from gamma-ray events. The green distribution shows events from the OFF region and thus represent the background. The background (hadron) distribution is wider than that of gamma-ray events. The ON and OFF regions are defined in Section 5.3.6

Table 5.2: Cuts used in the VERITAS Cygnus survey analysis to select gamma-ray showers. The descriptions of each cut parameter can be found in the text. The values are chosen by analysis of Crab Nebula and/or simulation data, and are fixed for a standard analysis.

	Moderate energy cuts	*Hard* energy cuts
Point source cuts	min number of tubes > 4 max core distance < 350 m min size ≤ 400 dc dist from camera center $< 2°$ max loss cut ≤ 0.5 $\theta^2 < 0.008$ $-1.2 < MSCW < 0.5$ $-1.2 < MSCL < 0.7$ Energy Threshold: 250-270	min number of tubes > 4 max core distance < 350 m min size ≤ 1000 dc dist from camera center $< 2°$ maximum loss cut ≤ 0.5 $\theta^2 < 0.008$ $-1.2 < MSCW < 0.5$ $-1.2 < MSCL < 0.7$ Energy Threshold: 450-550
Extended source cuts	N/A	min number of tubes > 4 max core distance < 350 m min size ≤ 500 dc dist from camera center $< 2°$ max loss cut ≤ 0.5 $\theta^2 < 0.050$ $-1.2 < MSCW < 0.5$ $-1.2 < MSCL < 0.7$ Energy Threshold: 450-550

$\theta^2 < 0.05$ for an extended-source analysis. The θ^2 distribution for the Crab Nebula is shown in Figure 5.16 Furthermore, a cut on the angular distance of the event form the center of the camera of 0.2° is used. The image cuts and shape cuts allow for a background rejection of more than 99.5% for a *point*-source analysis.

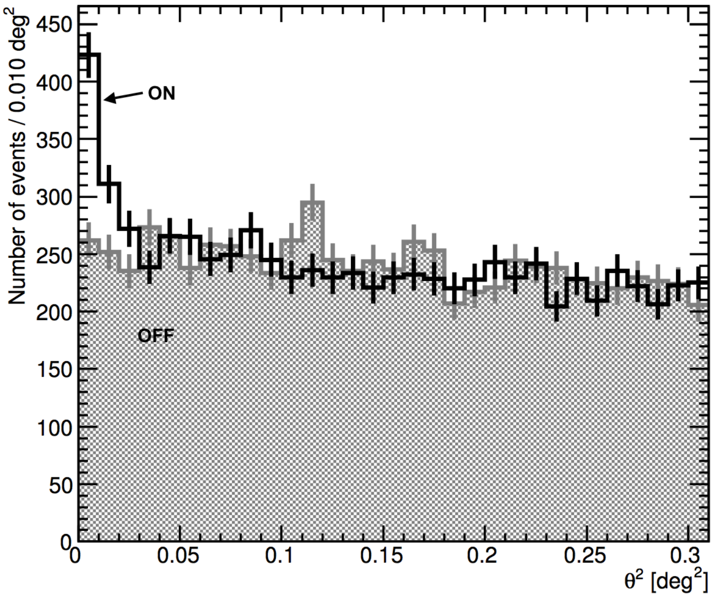

Figure 5.16: The distribution of θ^2 parameter for the Crab Nebula. It can be seen that a cut on θ^2 provides a cut on events not associated with the source location.

Table 5.3: The effects of various cuts for a sample analysis of one 20 minute run Crab data, using the ring background method. Calibration includes trace analysis (using the flasher data), time, and size cuts. $\alpha = 0.3134$ in this analysis.

Analysis stage	Number of events
Calibration	304577
removed by number of images > 2	154557
After MSCW cuts	137719
Spatial cuts	
At source position (ON)	104
At source position (OFF)	78
OFF×α	24.45
ON - OFF×α	79.55
Li and Ma significance	9.591 σ

5.3.6 Background Determination

There still remains a gamma-ray-like cosmic-ray background (largely due to electromagnetic showers initiated by cosmic-ray electrons), and so to determine if there is an excess of gamma rays at the source location above that background, the background must be estimated. A sky map is filled in with each reconstructed event that passes quality and hadron separation cuts. An ON and and an OFF region are then defined. There are three main background determination methods employed by VERITAS: the ON-OFF, the ring background, and the reflected region. In the simple ON-OFF method observations are taken ON the source position, and also at a defined OFF position on the sky covering the same horizon coordinates on the sky as the ON region, where no gamma-ray source is expected. This method requires observation time be used to take data in an OFF region. In order to take data more efficiently, VERITAS uses wobble-mode observations to cover the source position on the sky and get enough data to define an OFF region within the sky map rather than in a dedicated observation. These methods are described in a number of places, for example in [114].

For the ring background method, the OFF region is a ring centered around the ON region, with a radius chosen such that the ratio of the ON to OFF region area is approximately 1:10; see Figure 5.17 (a). The ratio of ON to OFF region areas is typically called α, and, for the ring background method, needs to be corrected to account for camera acceptance. The camera acceptance is the probability that a signal will be measured (see Figure 5.19) and it worsens away from the camera center. It is generally called the radial acceptance, as it is assumed that it is radially symmetric. The radial acceptances are determined from observations of gamma-ray-like events that are outside the exclusion region or from a different data set. There is good agreement with simulations to $1.5°$ from the camera center; therefore a cut on distance to camera center is used for the data analysis.

The reflected region method uses several circular regions of the same size as the ON region equidistant from the pointing position as the OFF region; this geometry is shown in Figure 5.17 (b). The events from these regions are scaled by the relative size of the ON and OFF regions to determine the level of background events. The OFF regions are each at

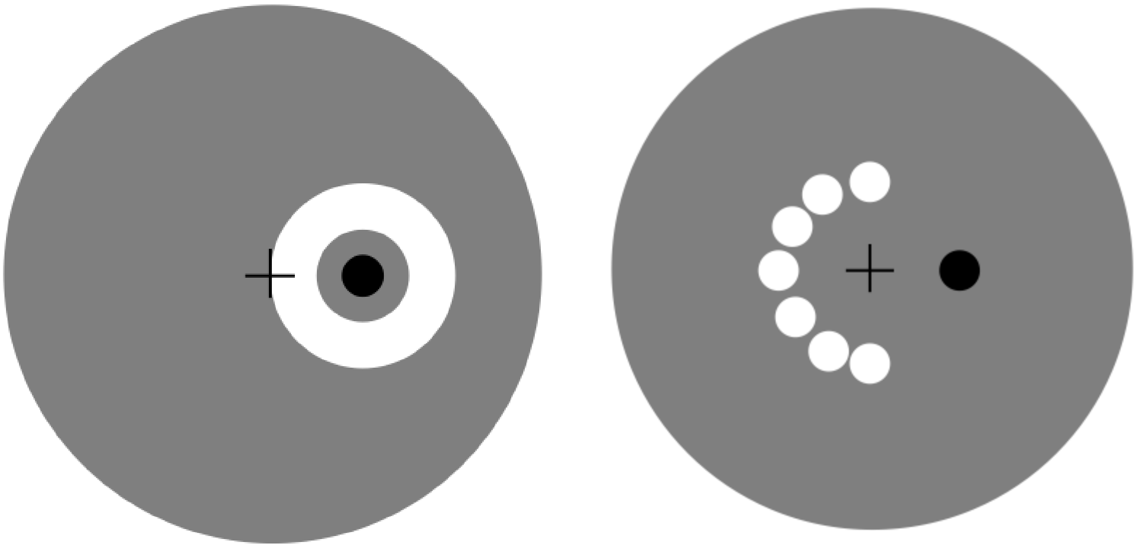
(a) Ring Background Method (b) Reflected Region Method

Figure 5.17: The ring background (a) and reflected region (b) methods for defining an OFF region. The gray circle represents the field of view of the camera. The black cross (+) represents the camera pointing. The black circle represents the source position, ON (typically 0.5° offset from the pointing direction). The white regions are then the OFF regions.

the same distance from the camera center as the ON region, and therefore no correction for camera acceptance is applied to the α.

The number of excess events is given by the number of events in the ON region minus the number of events in OFF region, normalized by α. Generally $\mathrm{N}_{\mathrm{excess}} = \mathrm{N}_{\mathrm{ON}} - \alpha \mathrm{N}_{\mathrm{OFF}}$

5.3.6.1 Radial Acceptance Studies

The standard ED analysis uses a pre-computed radial acceptance based on a gamma-ray events from a blazar source. In the course of the data analysis for the Cygnus region, it was determined that this source is not a good representation of the radial acceptance in the Cygnus region. This is due to differences in the zenith angle (see Figure 5.18) and a measurable dependence of the radial acceptance on the zenith angle (see Figure 5.19). The VEGAS analysis computes the radial acceptance using the data set being analyzed. This method was utilized for the Cygnus region analysis by ED as well.

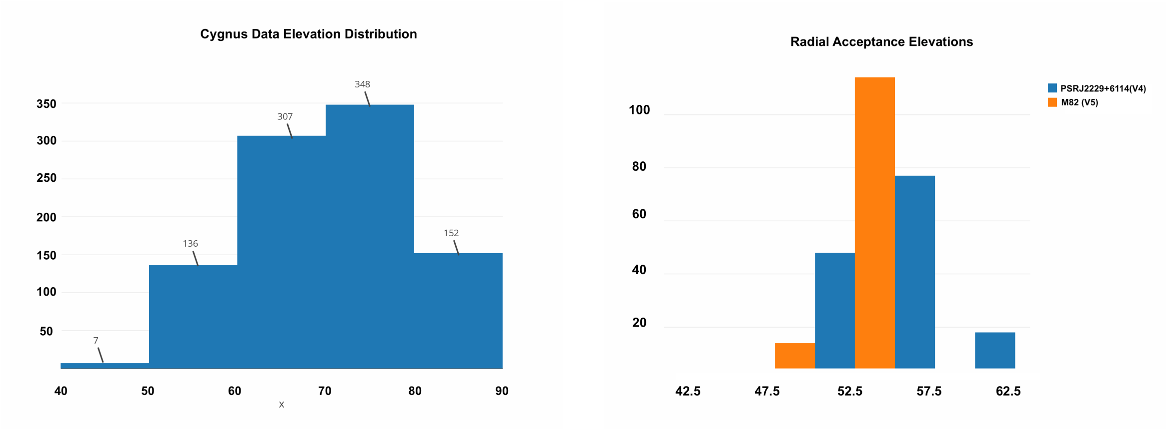

(a) Cygnus Data (b) Standard Data

Figure 5.18: (a) The elevation of data used in the Cygnus region analysis and (b) the elevation of data used to make the standard radial acceptance files.

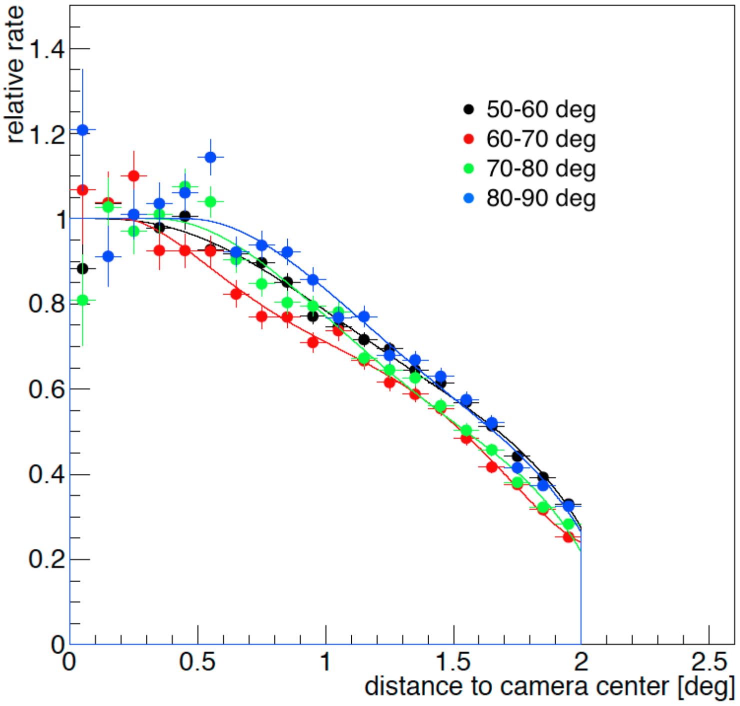

Figure 5.19: Radial acceptances (relative rate) as a function of distance to the camera center for the data used in the Cygnus region analysis. Each curve is for a different bin in zenith angle in degrees. There is a dependence on zenith angle, and thus different curves were used for data at different zenith angles.

5.3.7 Detection Significance

Now with a proper description of the ON and OFF events, the significance of a source is calculated following Eq. (17) of Li and Ma [115]:

$$S = \sqrt{2}\left\{ \mathrm{N_{ON}} \ln\left[\frac{1-\alpha}{\alpha}\left(\frac{\mathrm{N_{ON}}}{\mathrm{N_{ON}}+\mathrm{N_{OFF}}}\right)\right] + \mathrm{N_{OFF}} \ln\left[(1+\alpha)\left(\frac{\mathrm{N_{OFF}}}{\mathrm{N_{ON}}+\mathrm{N_{OFF}}}\right)\right]\right\}^{1/2} \quad (5.3)$$

A standard cutoff for the detection of the a gamma-ray source is the “five sigma” (5σ), or five standard deviation, threshold. At this level there is a less than 1 in 3.5 million chance pf obtaining a false positive if there is no signal. A more stringent requirement includes taking into account the trials factor of the detection into account. The Li and Ma significance is consistent with the Gaussian probabilities for cases when the observed counts are not too few, for $\mathrm{N_{ON}}$ and $\mathrm{N_{OFF}}$ greater than about 10.

In the case when the source does not pass the 5σ threshold for detection, an upper limit can be calculated using Helene [116], Rolke [117], or Feldman and Cousins [118]. When an upper limit is reported, the method for calculation and ON and OFF counts are reported as well.

The gamma-ray-like events are mapped onto a two dimensional sky map of 0.025° bins, and the signal and background calculations are applied on each pixel. The final sky map is presented in significance. It represents the integrated events in each bin and is smoothed, and thus the bins are correlated. This sky map can be used for fitting the extension of the source using options available in the software.

5.3.8 Spectral Reconstruction

With enough excess events detected, it is possible to construct a flux energy spectrum of the source. This can be used to gain insight into the physical processes at work in the source. The spectrum is in units of differential flux of gamma rays as a function of energy. The energy of each gamma ray is determined following the reconstruction discussed in Section

5.3.4 and is then binned. The flux in each bin is given by the number N per time t per average area $\langle A \rangle$:

$$\Phi(E) = \frac{N}{t\langle A \rangle} \tag{5.4}$$

To get the average area, an effective area is integrated over the energy bin of interest. Where an effective area is defined as

$$A_{eff}(E) = (\pi R^2)\frac{N_{selected}(E)}{N_{simulated}(E)} \tag{5.5}$$

where πR^2 is the simulated area over which the impact points of the primary particle are uniformly distributed, $N_{selescted}$ is the number that trigger the camera and pass selection cuts, and $N_{simulated}$ is the number of showers simulated. A typical effective area curves for varying zenith angle are shown in Figure 5.20. They are calculated by assuming a source spectrum and then using simulations to determine which events survive the selection cuts. The effective area varies with a number of parameters including: energy, zenith angle, source analysis cuts, and NSB. Tables taking into account many of these differences are produced using Monte Carlo simulations, and are used in the analysis for the flux calculation. Also noted on the figure is the energy threshold for each zenith angle curve.

In order to obtain $\langle A \rangle$, the flux of a source is assumed to follow a spectral shape

$$\phi(E) = \phi_0 \left(\frac{E}{E_0}\right)^{-\alpha} \tag{5.6}$$

where ϕ_0 is the normalization constant, E_0 the normalization energy, and α the spectral index. If the shape is assumed to be constant with energy, $N(E > E_{thresh})$ is number of excess events, and $N_{theory}(E > E_{thresh})$ the expected excess for a spectral shape then the flux is calculated with

$$\Phi(E > E_{thresh}) = \frac{N(E > E_{thresh})}{N_{theory}(E > E_{thresh})} \times \int_{E_{thresh}}^{\infty} \phi_0 \left(\frac{E}{E_0}\right)^{-\alpha} dE \tag{5.7}$$

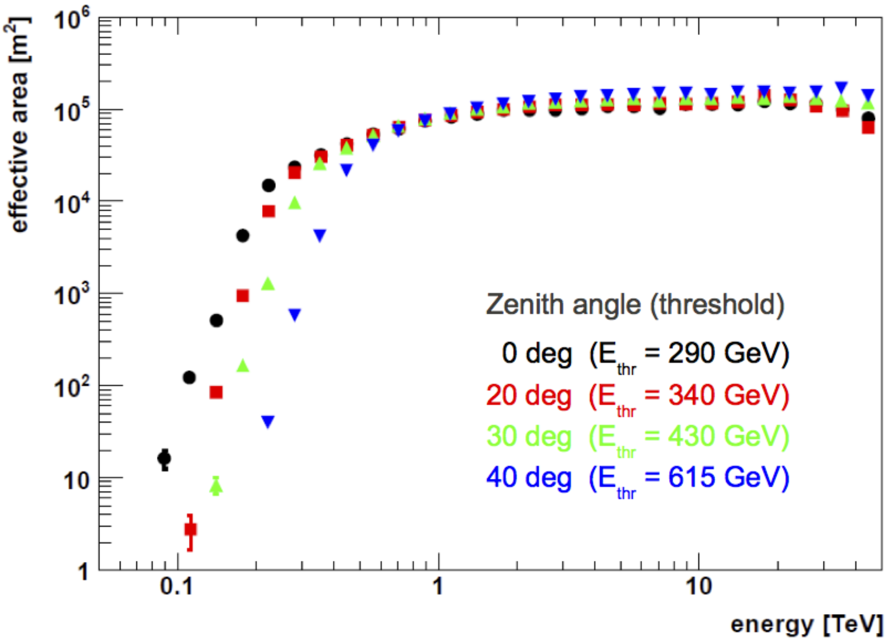

Figure 5.20: Moderate-source cut effective areas for varying zenith angle. The energy threshold for each is given in parentheses. This is for a source with a Crab-Nebula-like spectrum, observed at the standard wobble offset of 0.5°, and assuming a night sky noise similar to observations in the Galactic plane.

where

$$N_{theory}(E > E_{thresh}) = t_{obs} \times \int_{E_{thresh}}^{\infty} \phi_0 \left(\frac{E}{E_0}\right)^{-\alpha} A_{eff}(E)dE. \tag{5.8}$$

The resulting flux values depend on the assumed spectrum due to averaging the effective area over a finite bin width. The finite energy resolution of the instrument will also lead to spill-over of events between bins. ED determines the flux in bins that are at least as wide as the energy resolution and will calculate an upper limit if the flux in a bin is less than 2σ ([116–118]). The differential source spectrum can then be fit to the bins with measured values.

VERITAS is the primary instrument used in this work. Here the experiment and camera upgrade, and analysis procedure were discussed. The results are presented in Chapter 7. Next the other experiment used in this dissertation, the *Fermi*-LAT, will be discussed.

CHAPTER 6

The *Fermi*-LAT

While VERITAS is used for VHE observations of astrophysical sources, the *Fermi Gamma-ray Space Telescope* observes the universe in high-energy gamma rays (20 MeV to >300 GeV). Its observations are complementary to those done by VERITAS, and the data and tools for analysis are available to the public. This chapter begins with an overview of the experiment and concludes with an outline of the general data analysis procedures.

6.1 Experiment Description

The *Fermi Gamma-ray Space Telescope* (see Figure 6.1) has been operating since its launch in 2008 with two gamma-ray instruments: the Large Area Telescope (LAT) and the Gamma-ray Burst Monitor (GBM). The LAT is *Fermi's* primary instrument, and it is sensitive to gamma rays with energies from 20 MeV to greater than 300 GeV, making it the most sensitive detector to operate at GeV energies. For each gamma ray that the LAT detects, it measures its arrival time, direction, and energy. The LAT has a very large field-of-view ($>$ 2 steradians), and for a large part of its operation it has been observing in survey mode with very good stability. The effective collecting area is 6500 cm^2 at 1 GeV, which is quite small when compared to the large collection areas of IACTs (about 10^5 m^2 at 1 TeV). The angular resolution of the *Fermi*-LAT is strongly energy-dependent, with a 68% containment radius of about 0.8° at 1 GeV.

When a gamma ray enters the detector, it interacts with a high-Z (high atomic number) conversion foil made of tungsten, and undergoes pair production. The resulting electron and positron pair is tracked in single-sided silicon strip detectors, and the energy measured in

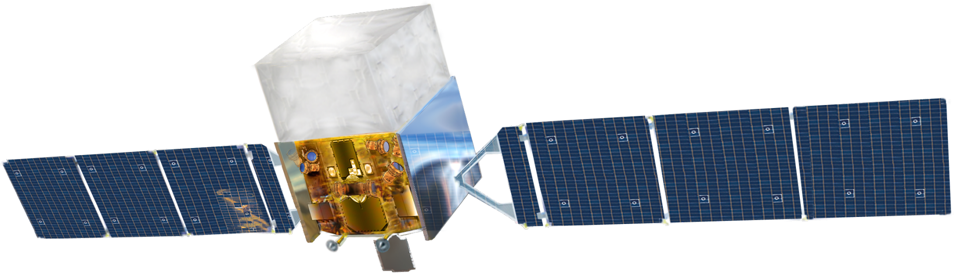

Figure 6.1: An artist's rendering of the *Fermi* satellite. Credit: NASA E/PO, Sonoma State University, Aurore Simonnet.

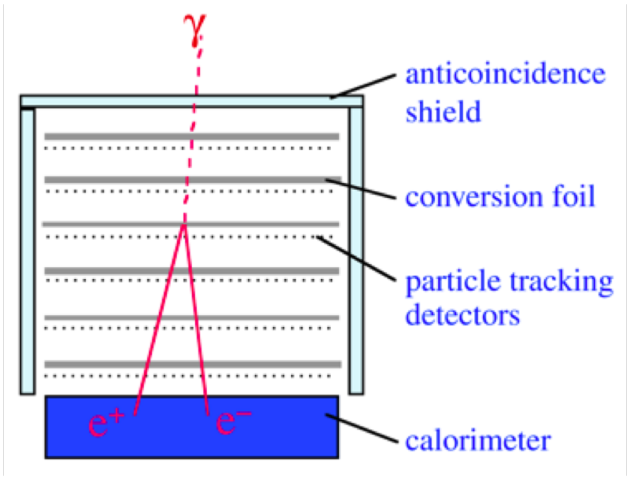

Figure 6.2: Diagram of pair-production, particle tracking, and calorimeter within the *Fermi*-LAT. Image credit: NASA/Sonoma State University/Aurore Simonnet.

via an electromagnetic shower in the calorimeter. An anticoincidence shield surrounds the front three sides of the instrument, which is diagrammed in Figure 6.2.

The current version of data released to the public uses the Pass 8 [98] event reconstruction. This data release included reprocessing the data from scratch (including simulations of the detector, event reconstruction, and background rejection) and implementing all of the knowledge of the instrument and environment gained in nearly five years of operations. This has resulted in improvements in the effective area (See Figure 6.3), the angular resolution, the understanding of systematic uncertainties, and the energy range of the data analysis. The resulting improvements of the LAT capabilities for Pass 8 data are presented in Table 6.1 where they are compared with the previous event reconstruction, Pass 7. The improvements in sensitivity at higher energies are of particular interest for the work in this dissertation.

Table 6.1: A comparison of *Fermi*-LAT Pass 7 and Pass 8 event reconstruction. The Pass 8 event reconstruction improves on the energy range, energy resolution and angular resolution of Pass 7.

IRF era	Energy Range	Energy Resolution at 10 GeV	Angular Resolution at 10 GeV
PASS7	20 MeV - 300 GeV	<10%	0.2°
PASS8	<20 MeV - 500 GeV	<8%	<0.1°

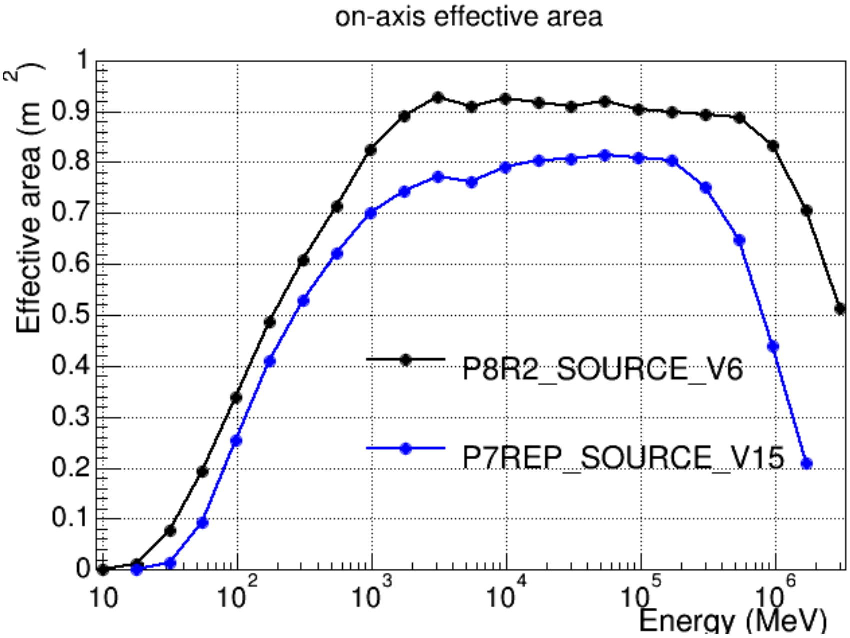

Figure 6.3: The improvement in the effective area of the *Fermi*-LAT going from Pass 7 (P7REP_SOURCE_V15) to Pass 8 (P8R2_SOURCE_V6). From [98].

6.2 Analysis

The *Fermi*-LAT analysis is undertaken with a publicly available set of tools available online [119]. The work in this dissertation uses v10p5r0 of the science tools, and the Fermipy Python tools [120]. The data used have gone through the Pass 8 event selection, described above. The analysis is undertaken following the documentation and threads available at the Fermipy website, and using the steps outlined by the *Fermi*-LAT collaboration. Tables describing the energy resolution, effective area, and angular resolution are called the Instrument Response Functions (IRFs), and are provided to the public with the analysis tools. Models for the Galactic and extragalactic diffuse emission are provided by the *Fermi*-LAT collaboration (gll_iem_v06.fits and P8R2_SOURCE_V6 files).

Here is a quick outline of the general binned analysis procedure; an overview of the data set analyzed in this work is discussed in Section 7.2. First the data are downloaded from the *Fermi*-LAT servers. Here the data can be selected for the region on the sky (called the region of interest or ROI), energy range, and time range of interest. Data are selected for an area of sky larger than the ROI to better account for photons from sources outside the ROI. Further selections to the data are made as the next step of the analysis, such as event class (SOURCE, CLEAN ...) and event type. The event classes correspond to the photon selection that is applied to the data. For example, P8R2_SOURCE_V6 is the recommended selection for a Galactic point source analysis such as the one undertaken in this dissertation.

Next, a counts map is made to identify any new bright sources and to provide a sanity check that the data covers the ROI. A three-dimensional map of the sky with a third axis for energy, called a counts cube, is generated. A livetime cube, describing the time that the LAT observed a given position on the sky at a given inclination angle, is pre-computed to speed up the exposure calculations. Then the exposure cube is generated. This is a map of the exposure of the experiment at each point in the sky with a third dimension of energy.

The likelihood fit requires an input model for the emission in the ROI. A reasonable starting point is the list of sources in the 3FGL catalog, or a higher energy catalog for an analysis with higher low energy cutoff. The model, saved as an `.xml` file, includes sources beyond the ROI that could contribute photons in the region. The model also allows for the definition of which sources are to be allowed to fluctuate during the likelihood fit and which are to be fixed. A source map tool creates the input-model counts map from the sources listed in the `.xml` file using the exposure and effective point spread function. With the Fermipy tools, all of the steps after downloading the data, from select events to source maps, are done with one setup script using parameters defined in a configuration file. These steps are the starting point for any *Fermi*-LAT analysis.

Once the setup of the source model is complete, it is possible to perform the likelihood fit. Using the binned analysis technique [121], the routine *gtlike* uses a maximum likelihood optimization to fit the model parameters. It is then possible to calculate the strength of the source detection, the flux of the source, and spectrum for sources in the region of interest. The metric used by the *Fermi*-LAT Collaboration is Test Statistic (TS) defined as:

$$\mathrm{TS} = -2\ln\left(L_{max,0}/L_{max,1}\right), \tag{6.1}$$

where $L_{max,0}$ is the maximum likelihood value for the model without the additional source (in this case the null hypothesis), and $L_{max,1}$ is the maximum likelihood value for the model with the additional source included. A larger TS indicates that the 'null' hypothesis is incorrect. $\sqrt{\mathrm{TS}}$ is approximately the detection significance of a source.

In this analysis, sources in the model with low TS (< 20) are removed from the model. It is not expected that the 3FGL would fully model the ROI due to a different low energy cutoff, and a longer exposure in the data analyzed for this work. A model map of the fit source parameters is subtracted from the counts map to make a residual map. A TS map, or map with TS computed at each bin in the ROI, can also be made. The Fermipy tools include a routine to find new sources (with TS > 25) which can then be added to the model. New sources identified in the analysis are detailed in Chapter 7.

Many of the brightest sources in the Galaxy, at *Fermi*-LAT energies, are pulsars. However, nearly all pulsars demonstrate an exponential cutoff in their spectrum. The pulsed emission is therefore not expected to contribute at TeV energies. In contrast, PWNe are very common TeV emitters, and any nebulae associated with these bright pulsars might be detectable by VERITAS. To search for any potential nebula emission an analysis needs to be done to remove (or at least significantly reduce) the pulsar emission. To do this, a "gated" analysis is conducted, where a time cut is applied to the photons using the phase of the pulsar to remove the on-pulse contribution.

We used Tempo2 [122], a pulsar timing software package, to assign pulsar phases to the pulsars using the timing models available at [123]; the phaseograms are checked against the published results. The on-pulse region was defined to cover any on-pulse or bridge emission, with identifying all of the pulsar emission taking precedence over the amount of time available for the off-pulse analysis. This means that the remaining emission at the source should only be the (much weaker) off-pulse emission and should allow for any background sources to become apparent. The pulsar timing and on- and off-pulse maps for the pulsars in the Cygnus region can be seen in Appendix C.

An ideal analysis would have pulsar models over the whole time range of the dataset, but these are not yet publicly available. Because of this limitation, we performed an on-pulse analysis on the data range available to fit an on-pulse source. The model of the pulsar in the analysis of the full dataset was then fixed to the on-pulse values, and the dataset refit. Nebula emission should then be apparent as a positive residual. For this method to work, the on-pulse flux needs to be steady over time, so we produced lightcurves of each of these objects and checked for flux variability.

The details and results of the *Fermi*-LAT analysis of the Cygnus region are presented in Chapter 7.

CHAPTER 7

The VERITAS Cygnus Survey

This chapter covers the VERITAS Cygnus survey analysis efforts, starting with a detailed discussion of the VERITAS observations undertaken and data quality selection (in Section 7.1), as well as the *Fermi*-LAT data (in Section 7.2). Next is a quick overview of the previous VERITAS results in the region, followed by a study of the systematic errors and a determination of the trials factor in Section 7.4 and Section 7.5, respectively. The chapter concludes with the VERITAS and *Fermi*-LAT results in the region as a whole and for specific sources/regions of interest. The work presented in the chapter comes partially from a paper being prepared with significant contributions from Ralph Bird (UCLA) and Maria Krause (DESY). The official VERITAS results for the paper come from the VEGAS analysis package; all other plots in this dissertation are from ED, unless otherwise noted.

7.1 Observations

The observations undertaken by VERITAS in the Cygnus region include 140 hours of observations taken in survey mode from 2007-2009. These observations resulted in a nearly uniform effective exposure of 6-7 hours in a 15° by 5° area of the Cygnus region of the Galaxy from 67° to 82° Galactic latitude and from $-1°$ to 4° Galactic longitude, as well as coverage with a smaller effective exposure over a 9° by 19° region. Furthermore, the full data set includes about 150 hours of follow-up point source observations taken from 2008 to 2012. All observations were taken with zenith angles from 10°-35° to minimize the systematic uncertainties associated with large zenith-angle observations. The survey and follow-up observations result in a data set of 949 runs, or 295 hours of data, with an average elevation

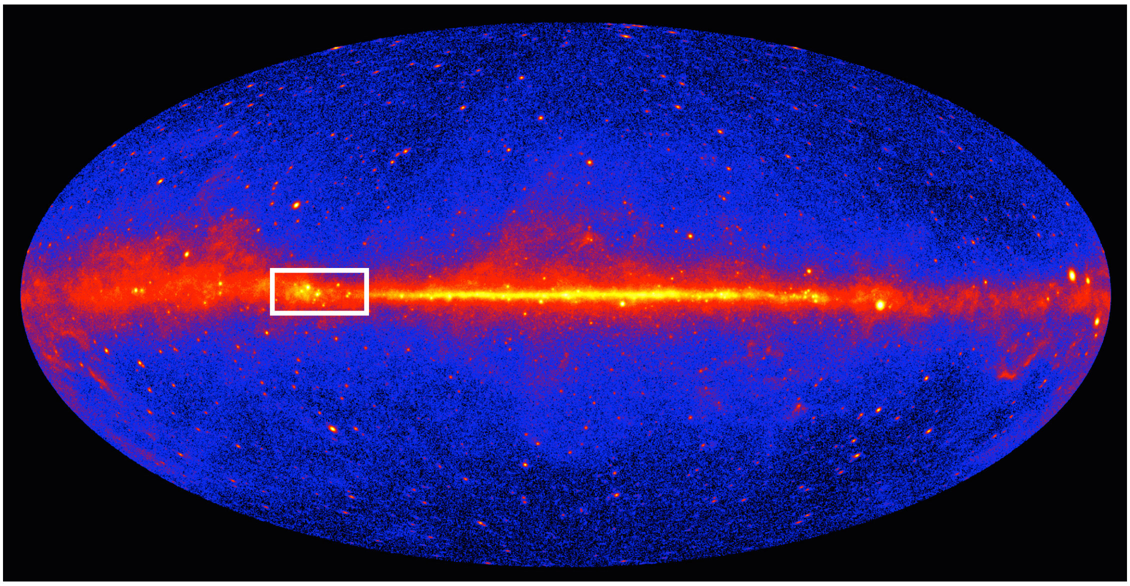

Figure 7.1: The *Fermi*-LAT all-sky view with the Cygnus region marked as a box.

Table 7.1: Summary of the numbers of data runs taken and runs cut by DQM with corresponding observing time for the survey mode and follow-up Cygnus observations.

	Survey Runs	Follow-up Observations	Total
Number of runs taken	548	718	1266
Hours	183	239	422
Number cut by DQM	139	178	317
Hours	47	59	106
Hours cut within runs	6	15	21
Number of good runs	409	540	949
Hours	130	165	295

of 69.8°. The resulting exposure from combining these observations is displayed in figure 7.2.

Out of a total number of 548 data runs taken as sky survey observations in the region, 139 of these are marked as “do not use” in the data quality monitoring (DQM). The follow-up pointed observations add a further 718 runs, of which 178 were cut by DQM. Table 7.1 summarizes the number of runs in the data set and the number cut by DQM. To the total data set of 944, comprising 316 hours of data, further time cuts have been applied, resulting in a total 295 hours of data. 194 runs in the total data set are three-telescope runs, requiring different instrument response functions (IRFs).

In order to do a VERITAS analysis, a list of bright stars for exclusion in the analysis

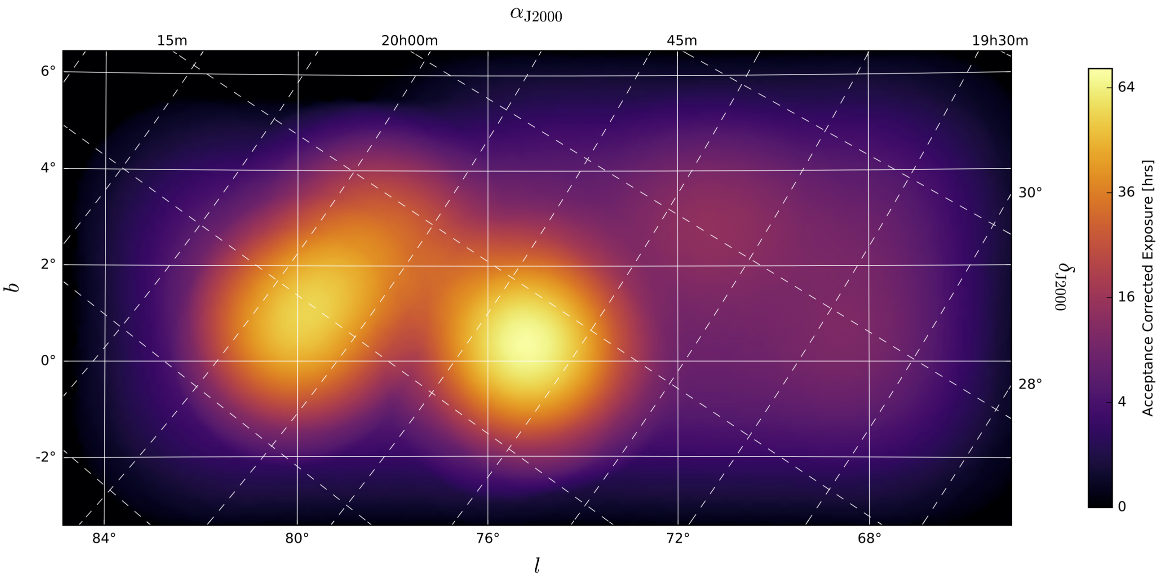

Figure 7.2: The VERITAS exposure in the Cygnus region mapped in Galactic coordinates (with RA, dec indicated). The color scale is in hours.

must be generated. The two analysis packages use different default magnitude cutoffs and different exclusion sizes. Furthermore, the region has a large number of bright stars, so the cutoff magnitude should not be too low otherwise a large region of the sky will be cut out of the analysis. A cutoff magnitude of 6 was decided for the survey analysis and was used by both analysis packages. Furthermore, the previously detected VERITAS sources are defined as exclusion regions. The definitions for the exclusion regions and a map of the regions are shown in Appendix A.

There have been over 60 further hours of observations in the region since 2012 with the upgraded VERITAS cameras. These data will not be discussed here, but are being analyzed for future study by the VERITAS collaboration.

7.2 *Fermi*-LAT Data Set

The *Fermi*-LAT data were selected covering a 30° radius region centered at Galactic longitude (l) 74.5° and Galactic latitude (b) 1.5° from the mission start to January 2016. In order to minimize the contribution of the Galactic diffuse emission and maximize angular resolution, photons were selected in the energy range from 1–500 GeV. The counts map is shown in Figure 7.15. A description of the data downloaded for this analysis is presented in Appendix B.

A model file was generated using the *Fermi* Large Area Telescope Third Source Catalog (3FGL) catalog [59], with templates for extended sources (including the Cygnus cocoon) provided by the *Fermi*-LAT Collaboration. It was also confirmed that the sources from the 1FHL (The First *Fermi*-LAT Catalog of Sources Above 10 GeV) [60] and 2FHL (The Second Catalog of Hard *Fermi*-LAT Sources) [61] are also 3FGL sources, and do not need to be added to the model. The model is generated to cover a region extending beyond the analysis region by 5°. Any sources expected to contribute less than 10 photons to the analysis region were deleted from the model. For this analysis the Galactic diffuse emission model, gll_iem_v06.fits, and isotropic diffuse model, iso_P8R2_SOURCE_V6_v06.txt, provided by the *Fermi*-LAT collaboration were used. After an initial fit, sources with a TS (test statistic) less than 16 were removed from the subsequent fits. The list of removed sources and the list of new sources outside the Cygnus region is available in Appendix B.

Following the pulsar analysis procedure outlined in Section 6.2, the four brightest pulsars in the region were examined for off-pulse emission. The phase analysis and on pulse fits are detailed in Appendix C

7.3 Previous VERITAS Results

VERITAS has previously published the following results on four sources in the Cygnus region: VER J2019+407 (associated with the γ-Cygni SNR) [124], TeV 2032+4130 [125], and two sources in the Cygnus OB1 region coincident with MGRO J2019+37 [126].

7.3.1 TeV J2032+4130, VER J2031+415

The initial detection of TeV J2032+4130 by HEGRA and early observations by Milagro and ARGO-YBJ are discussed in Chapter 3. It was detected at the 8.7σ significance level by

VERITAS following 48.2 hours of observations from 2009-2012 and is given the designation VER J2031+415 [125]. The VERITAS centroid of the emission is at (l,b) = 80.3°, 1.11° ((RA,dec) = $20^h 31^m 41^s$±65s, 41°33'48"±37 (J2000)), consistent with previous detections. The VERITAS data indicate extended emission in the shape of an oval with a major axis of 9.5'±1.2' and a minor axis of 4.0'±0.5', oriented to the northwest by $-63 \pm 6°$. The spectrum is well fit by a differential power law ($dN/dE = N_0 \times (E/TeV)^{-\Gamma}$), where Γ is the index and N_0 is the normalization, with an index of 2.10 $\pm 0.14_{stat} \pm 0.21_{sys}$ and a normalization of $(9.5 \pm 1.6_{stat} \pm 2.2_{sys}) \times 10^{13}$ TeV^{-1} cm^{-2} s^{-1} at 1 TeV.

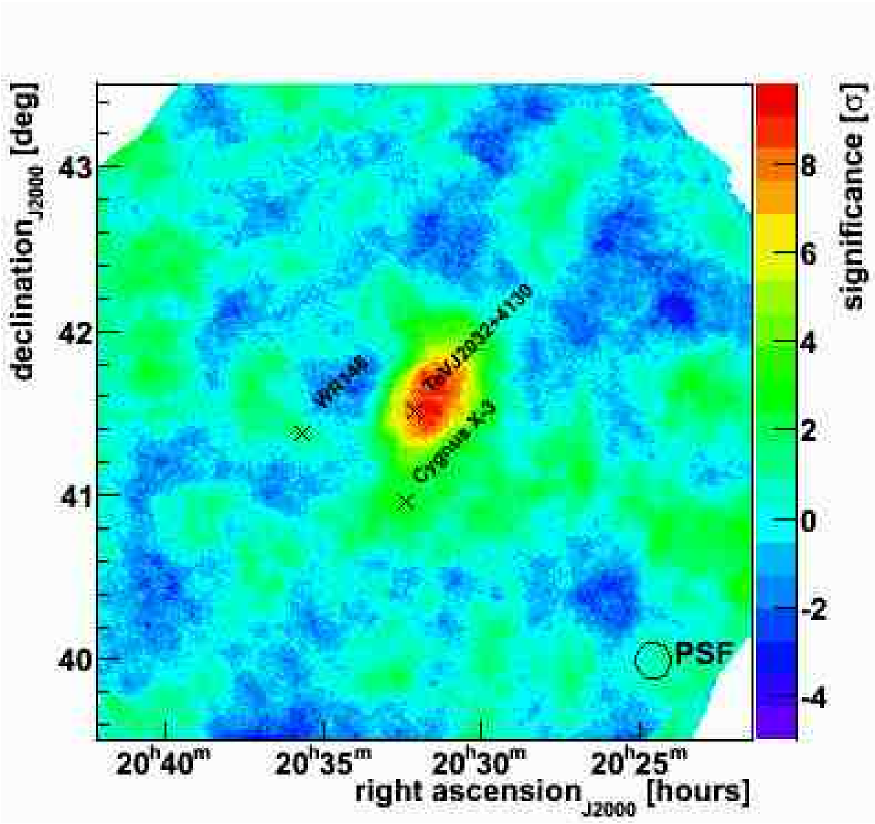

Figure 7.3: VERITAS significance map of TeV 2032+4130. Color indicates significance, the ×'s show the positions of the Wolf-Rayet star WR 144, Cygnus X-3 (also in the field-of-view of the VERITAS observations), and TeV 2032+4130, coincident with the *Fermi*-LAT pulsar PSR J2032+4127. The black circle indicates the VERITAS point spread function (68% containment). Figure from [125].

There are various scenarios for the emission from TeV J2032+4130, which depend on which objects within the TeV extent of the source are considered to be associated. Objects in the Cygnus X complex with possible ties to the Milagro source TeV J2032+37 include the Cygnus OB2 association, Cygnus X-3, the γ-Cygni SNR nearby, and the *Fermi*-LAT detected pulsar (a possible PWN scenario). An earlier analysis of the region around the *Fermi*-LAT pulsar undertaken using four years of data over an energy range of 500 MeV to 100 GeV and using a cut on pulsar timing, found no evidence of PWN emission at *Fermi*-LAT energies. The location of TeV J2032+4130 is in a rare void in the radio and infrared (IR) that appears to be a region cleared by a supernova or pulsar wind nebula, but the possibility of particle acceleration by stellar winds from stars in the OB2 association cannot be ruled out.

7.3.2 γ-Cygni SNR, VER J2019+407

VER J2019+407 is an extended source associated with the γ-Cygni SNR (SNR G 78.2+2.1) detected at the 7.5σ significance level by VERITAS at a flux of 3.7% of the Crab Nebula flux in 21.4 hr of data analyzed in 2009 [124]. The VERITAS source is located in the northwestern rim of the remnant centered at (l,b) = 78.2°, 2.26° ((RA,dec) = $20^h20^m4.8^s$, 40°45’36”±37 (J2000)) with a statistical positional uncertainty of 0.03°, a systematic positional uncertainty of 0.018°, and with a spatial extent of 0.23°. Figure 7.4 shows the VERITAS detection (background subtracted, acceptance corrected) with mutiwavelength contours and sources overlaid. The position of the *Fermi*-LAT detected pulsar is indicated near the center of the remnant, about 0.5° away from the VERITAS source position. The spectrum is characterized by a differential power law with an index of 2.37 $\pm 0.14_{stat} \pm 0.20_{sys}$ and a normalization of 1.5 $\pm 0.2_{stat} \pm 0.4^{12}_{sys}$ photon TeV^{-1} cm^{-2} s^{-1}. This yields an integral flux of 5.2 $\pm 0.8_{stat} \pm 1.4^{-12}_{sys}$ photon cm^{-2} s^{-1} above 320 GeV, corresponding to 3.7% of the Crab Nebula flux.

The TeV source is coincident with a region of enhanced x-ray emission, and with bright radio arcs of the SNR. It is unlikely that this single SNR could account for all of the cosmic-ray acceleration in the Cygnus cocoon region based on its brightness, but it could be a significant contribution. The other proposed scenario for particle acceleration at VER J2019+407 is that of a PWNe, either of the *Fermi*-LAT detected pulsar or of a yet unidentified pulsar.

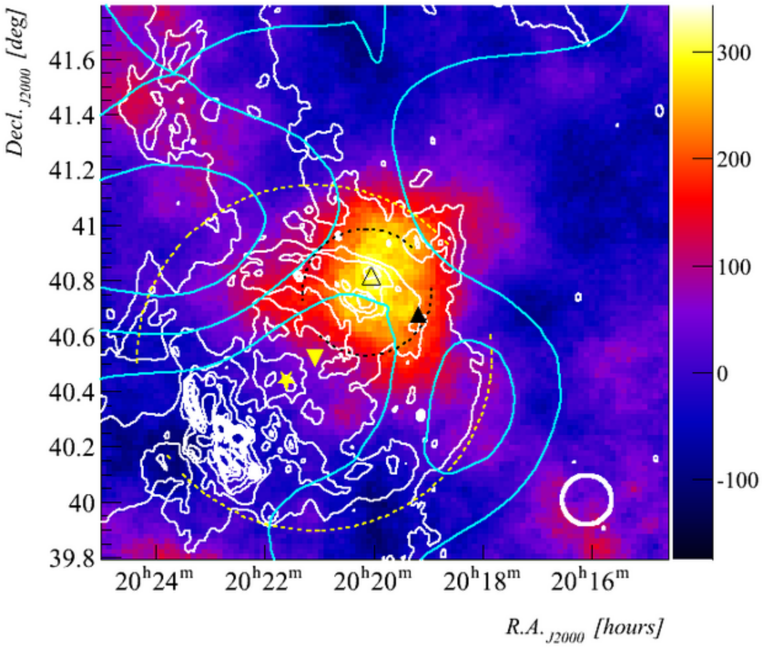

Figure 7.4: A 1.4° by 1.4° skymap of the source VER J2019+407 excess map (color scale, in units of excess counts). The dashed black circle indicates the 1σ fitted extent for the remnant based on the VERITAS data. Overlaid are: the greater than 10 GeV gamma-ray emission detected by the *Fermi*-LAT (from the 2FGL) (yellow dash-dot circle, centroid indicated by the yellow upside down triangle), the 1420 MHz radio continuum contours in white, and the Cygnus cocoon in cyan (0.16, 0.24, 0.32 photons/bin contours). The open and filled black triangles show the respective positions of the deprecated catalog sources 1FGL J2020.0+4049 and 2FGL J2019.1+4040. The small white circle indicates the VERITAS point spread function (68% containment). Figure from [124].

7.3.3 VER J2016+317 (CTB 87) and VER J2019+368 (Cisne)

Using 70 hours of data, VERITAS resolved two sources in the region of MGRO J2019+37, a point-like source, VER J2016+317 (associated with CTB 87, a SNR), and VER J2019+378 (a bright extended source with numerous possible counterparts) [126]. The excess map is presented in Figure 7.5. VER J2016+317 is detected with a significance of 7σ at the position (l,b) = 74.9°, 1.14° ((RA,dec) = $20^h16^m2^s$±3s, 37°11'52"±40' (J2000)) with no significant source extension, and a spectrum of the emission that is best fit by a differential power law with index 2.3 ± 0.4. The peak of the emission from this source is consistent with the peak of the radio emission of SNR CTB 87. The other source is detected at 8.2σ using an extended source search. The peak of the emission from VER J2019+368 is at (l,b) = 74.9°, 0.36° ((RA,dec) = $20^h19^m25^s$±72s, 36°48'14"±58' (J2000)); it has an elongated oval shape of 0.34°±0.03°along the major axis, 0.13°±0.02° along the minor axis with an angle of 71° east of north. A two-source model did not provide a good fit for VER J2019+378. Taken as one source, the spectrum was well fit by a differential power law with index 1.7 ± 0.3.

The contours of the VHE emission overlap a bright, extended low-energy emission region of the SNR CTB 87. Detailed studies of the morphology of the source in the future could clear up the ambiguity of the source as a PWN or as a SNR. The PWN scenario would require either the x-ray pulsar associated with the region to have a large proper motion, and an age less than 5-10 kyr, or the more typical picture for an x-ray PWNe at VHE of cosmic microwave background photons being accelerated by inverse Compton scattering. The VERITAS source is also co-located with the *Fermi*-LAT source 3FGL J2015.6+3709, which has a proposed extragalactic origin with the nearby blazar. There is no VERITAS emission associated with the blazar, as it is well separated from the errors on the position of VER J2016+371. Because of this clear separation and the similarities with other VHE PWNe, the preferred source classification of VER J2016+371 is that of a PWN associated with SNR CTB 87.

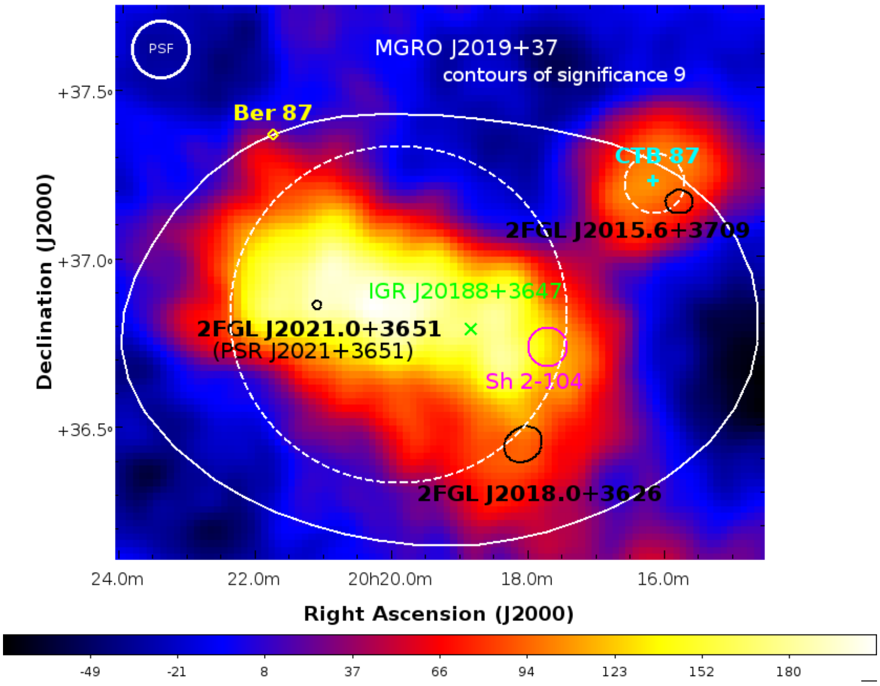

Figure 7.5: VERITAS excess map (color scale) of the region around MGRO J2019+37 above 600 GeV. The color bar corresponds to the number of excess events. The change from red to blue occurs at 3σ. The regions for spectrum analysis of the two VERITAS sources are demarcated by the white dashed circles, and the potential counterparts are indicated with either ellipses representing their shape or crosses. The 9σ significance level MGRO J2019+37 contour is in white. Figure from [126].

7.3.4 Previous Limits

VERITAS has furthermore reported limits on the microquasar binary system Cygnus X-3 [53]. Using 44 hours of data taken from 2007-2011, no significant emission from the binary was detected. Flux upper limits were made using the Rolke method [117]. The limit was not strong enough to constrain the overall spectral shape based on *Fermi*-LAT spectrum extrapolations.

7.4 Systematics Studies

The Cygnus region data set is unique compared to data sets based on the standard VERITAS pointed observations. It is comprised of a number of observations along a grid, as well as extensive follow-up observations at a few locations of interest. The data therefore covers a large region with varying observation times. A number of studies were undertaken to confirm the stability of the analysis procedures and confirm that the two independent analysis packages are consistent under a variety of observing conditions. These conditions include two array epochs, V4 (before the T1 move) and V5, as well as two observing seasons, Winter (ATM21) and Summer (ATM22) over the five years of observations. The first systematic study was with the Crab Nebula, the brightest steady VHE gamma-ray point source. Second, we tested the consistence of the extended source analysis on the source MGRO J1908+106.

7.4.1 Crab

Due to its unique nature as a bright, Galactic point source at TeV energies, the Crab Nebula is an important source for characterizing non-standard VHE gamma-ray observations and new analysis techniques. A mini-survey of the Crab Nebula was undertaken at the same time as the original Cygnus survey and it can be used to characterize the sensitivity of the analysis techniques. We also evaluated five hours of Crab Nebula data taken each observing season.

The observations for the mini-survey were taken in ten grid pointings in the region around the Crab Nebula resulting in about three hours of data with an average elevation of 76°. The analysis was undertaken without inputting the known source location. The data can be used to compare our updated standard analysis methods with the methods available at the time of the survey, as well as to characterize any improvements made possible by new analysis techniques that are still being evaluated for their usefulness and accuracy. Shown in Figure 7.6 is the analysis for this mini-survey data for extended source moderate cuts; the figure shows that the two analyses are consistent for a bright point source such as the Crab Nebula. Further checks of the extended source analysis with MGRO J1908, in the next section, show that hard extended cuts are more appropriate for a weak extended source.

From the analysis of the year-by-year Crab data it has been determined both that the two analysis packages are consistent with each other and that they are consistent on a year-by-year basis. The year-by-year consistency with ED is shown in Figure 7.7. The consistency between packages and by epoch is shown in Figure 7.8.

Table 7.2: The results of the Crab Nebula analysis with VEGAS and ED over the two observing epochs – V4 and V5. The index and flux normalization are shown for a simple power-law spectrum fit.

Value	VEGAS V4	VEGAS V5	ED V4	ED V5
Spectral index	-2.46	-2.45	-2.50	-2.50
Flux normalization ($\mathrm{cm}^{-2}\mathrm{s}^{-1}\mathrm{TeV}^{-1}$)	3.14×10^{-11}	3.28×10^{-11}	3.15×10^{-11}	3.17×10^{-11}
Flux norm error	6.1×10^{-13}	5.2×10^{-13}	6.88×10^{-13}	5.77×10^{-13}

7.4.2 MGRO J1908+106

Because a large number of Galactic sources are extended on the sky, we furthermore checked that the spatial reconstruction of the two analysis packages is consistent using extended source cuts. We decided to use the VERITAS-detected Milagro source MGRO J1908+106 to check this, due to its previously measured extension [127]. The maps produced by each analysis package are presented side by side in Figure 7.9. It can be seen that the spatial reconstruction with each package is consistent.

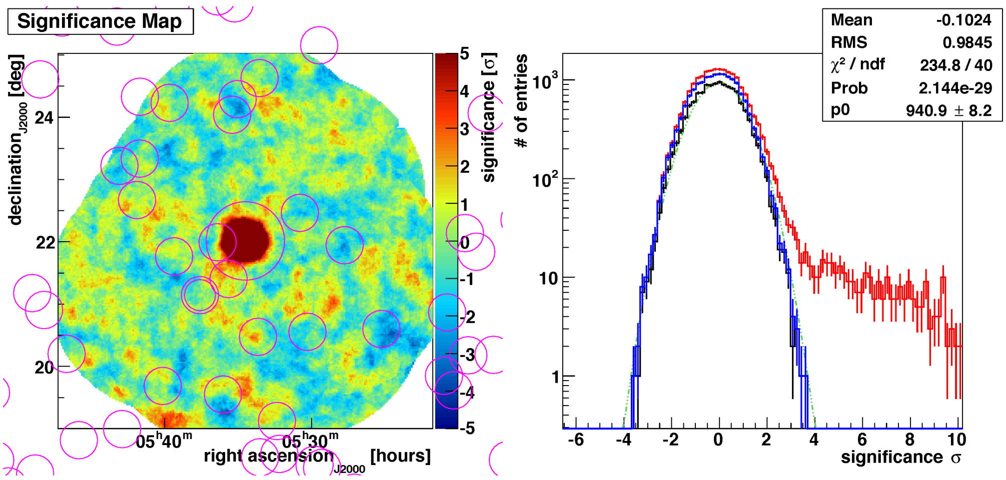

(a) ED sky map

(b) ED Significance Distribution

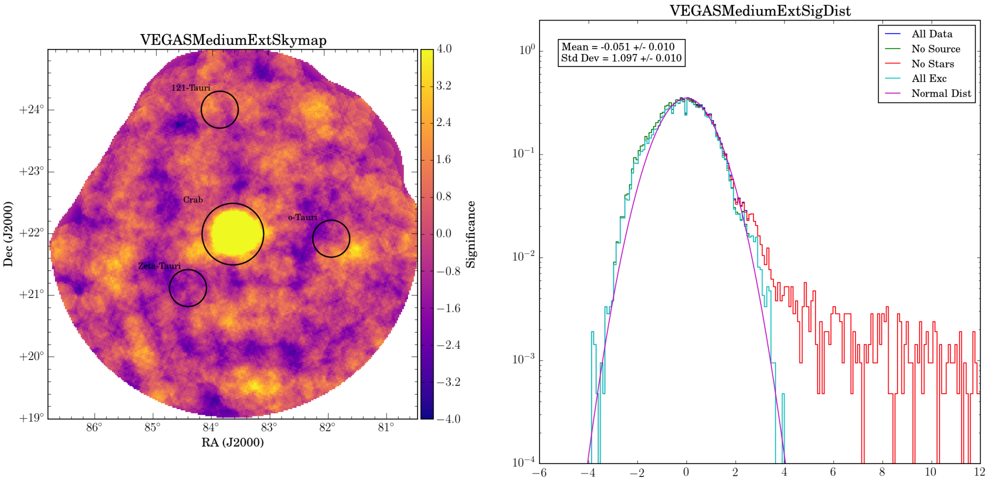

(c) VEGAS sky map

(d) VEGAS Significance Distribution

Figure 7.6: The ED (top) and VEGAS (bottom) results for the mini-survey of the Crab Nebula using extended, moderate spectrum source cuts. On the left are the skymaps (in significance, color scale) of the region for each package, and on the left are the resulting significance distributions. The analyses are consistent for a bright point source such as the Crab Nebula.

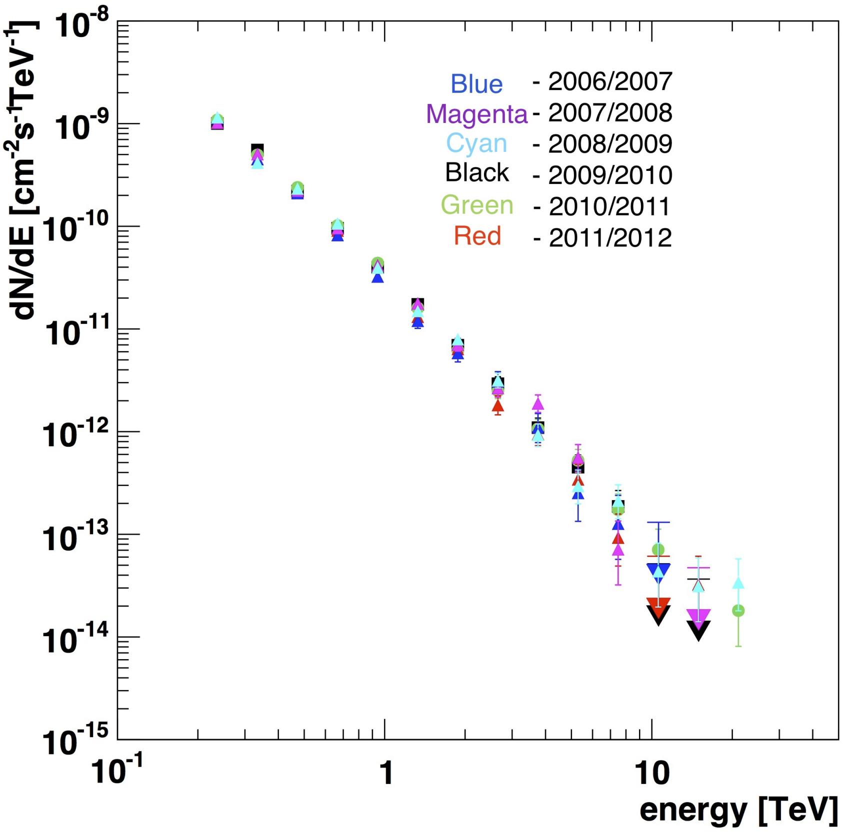

Figure 7.7: The Crab Nebula spectra determined on a year-by-year basis by ED. They are all consistent with each other, showing that the analysis is robust under the two observing epochs and varying conditions.

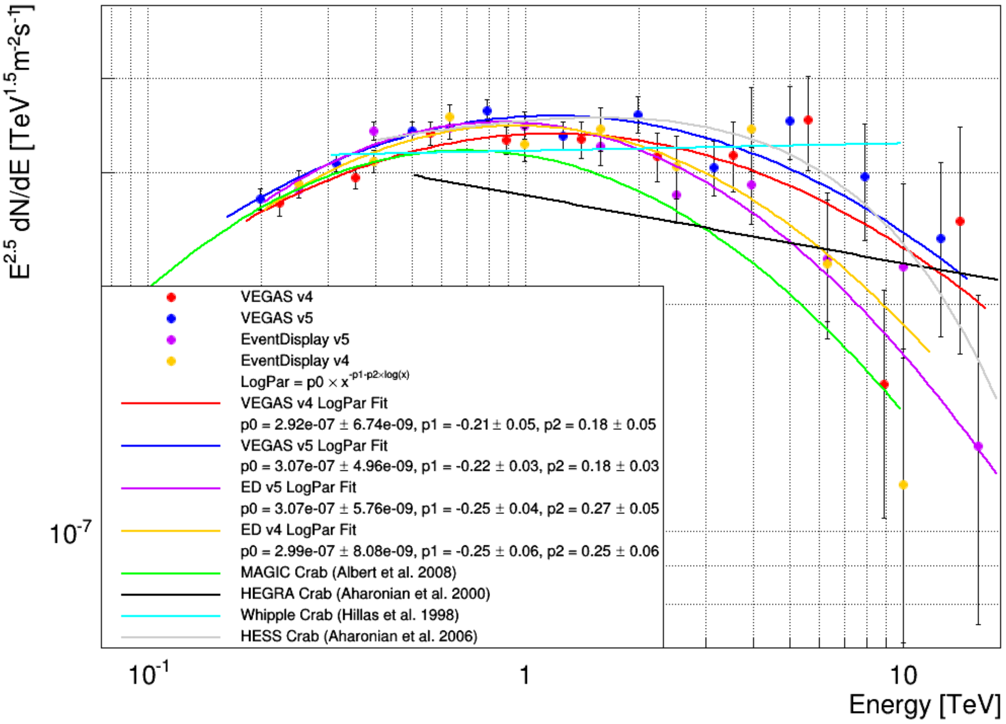

Figure 7.8: The Crab Nebula spectrum produced epoch to epoch with VEGAS and ED. The curves indicate the fit for each spectrum. This shows that the two analysis packages are consistent with each other and over time. Also shown are the results from the MAGIC, HEGRA, Whipple, and H.E.S.S. experiments to indicate the consistency with other experiments.

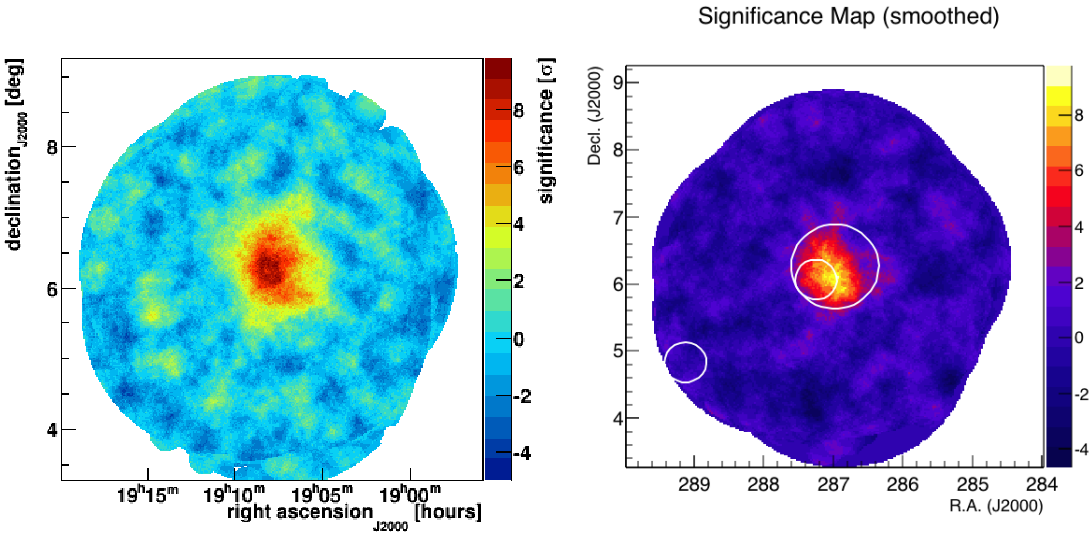

(a) ED map

(b) VEGAS map

Figure 7.9: The ED (a) and VEGAS (b) significance (color scale) sky maps of the region of MGRO J1908+106. The source is measured to have a consistent extent, morphology, and location reconstruction in each analysis package. Differences in maximum significance are consistent with the differences in methodology and energy threshold between the two packages.

7.5 Trials Factor Estimation

A blind search over the region for significant gamma-ray sources would incur a large trials factor from the “look-elsewhere” effect. Therefore a Monte Carlo simulation was undertaken to determine the trials factor. The first step was to create an exposure-corrected acceptance map such as the exposure shown in Figure 7.2. Then random photons were generated according to that exposure map. Next, the significance map was generated using the same ring background method (RBM) analysis chosen for the analysis of the Cygnus data set. An example random photon map and significance map are presented in Figure 7.10. The value of significance of the highest significance bin is recorded, as well as the value of significance of a reference bin. In total about 1.5×10^6 simulations were performed for both the point and extended source analyses. The difference in the trials factor between the two was less than 2%, and was therefore determined to be negligible.

The relationship between a pre-trials probability (p_{pre}) and a post-trials (p_{post}) probability is given by:

$$p_{pre} = 1 - (1 - p_{post})^{1/X_T}. \tag{7.1}$$

The resulting trials factor versus significance for the Cygnus region analysis is shown in Figure 7.11. For example for a pre-trials significance of below about 4.5σ, the post-trials significance is 0. This is consistent with expecting a fluctuation of this size in every observation covering this area.

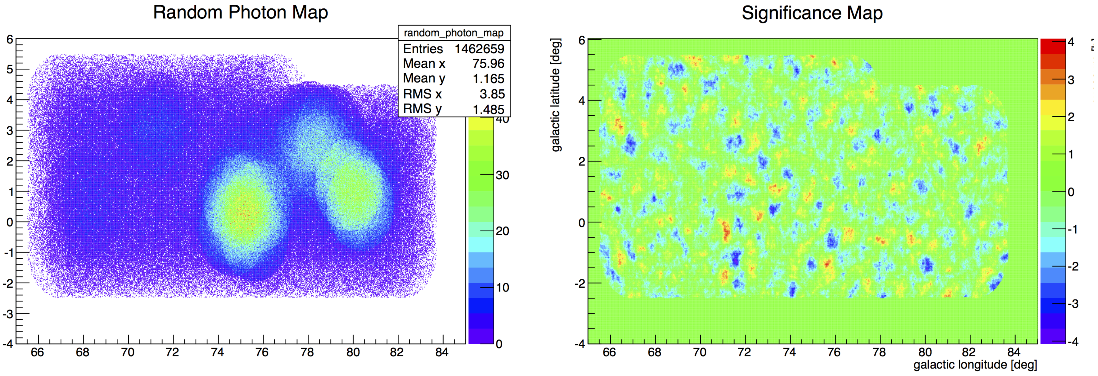

(a) Random photons (b) RBM significance map

Figure 7.10: (a) An example of the random photon map generated for the trials simulation analysis and (b) the resulting significance map. The value of significance for the highest significance bin and a reference bin are saved for each random photon map.

7.6 Results

This section begins with an overview of the results for the entire region as seen by VERITAS and *Fermi*-LAT. It then discusses the detailed results for individual sources seen by both experiments and concludes with the VERITAS upper limits for sources that are seen by *Fermi*-LAT, as well as for other sources of interest as discussed in Chapter 3.

7.6.1 VERITAS Sky Maps

Section 7.6.1 shows the VERITAS sky maps for the full analysis of the Cygnus region. The significance is plotted as a function of Galactic latitude and longitude (l,b). When looking at these sky maps, the four previously detected sources are clearly visible. No new sources or

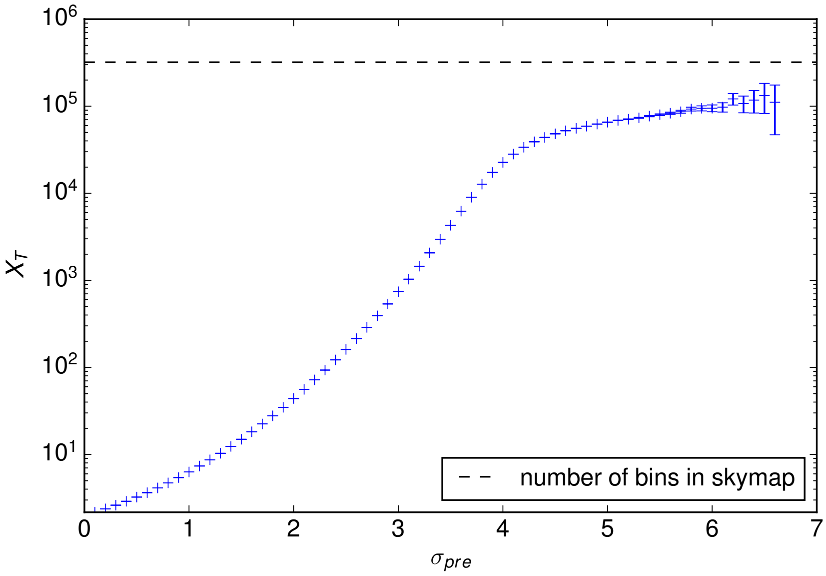

Figure 7.11: The trials factor, X_T, as a function of local significance, σ_{pre}. The black dashed line represents the total number of bins in the Cygnus region seen by VERITAS.

hot spots are visible on these maps. A significance distribution, with the measured sources and the bright stars excluded, is consistent with a normal distribution with a mean at 0 and a standard deviation of 1 (as expected for the background). This is shown in Figure 7.14. To check for weak sources which could be masked by the total significance distribution, the whole region was split into smaller (4° × 4° square) regions and the distributions checked for evidence of a significance above background in each region. When measured sources and bright stars are excluded the smaller region significance distributions are also consistent with background.

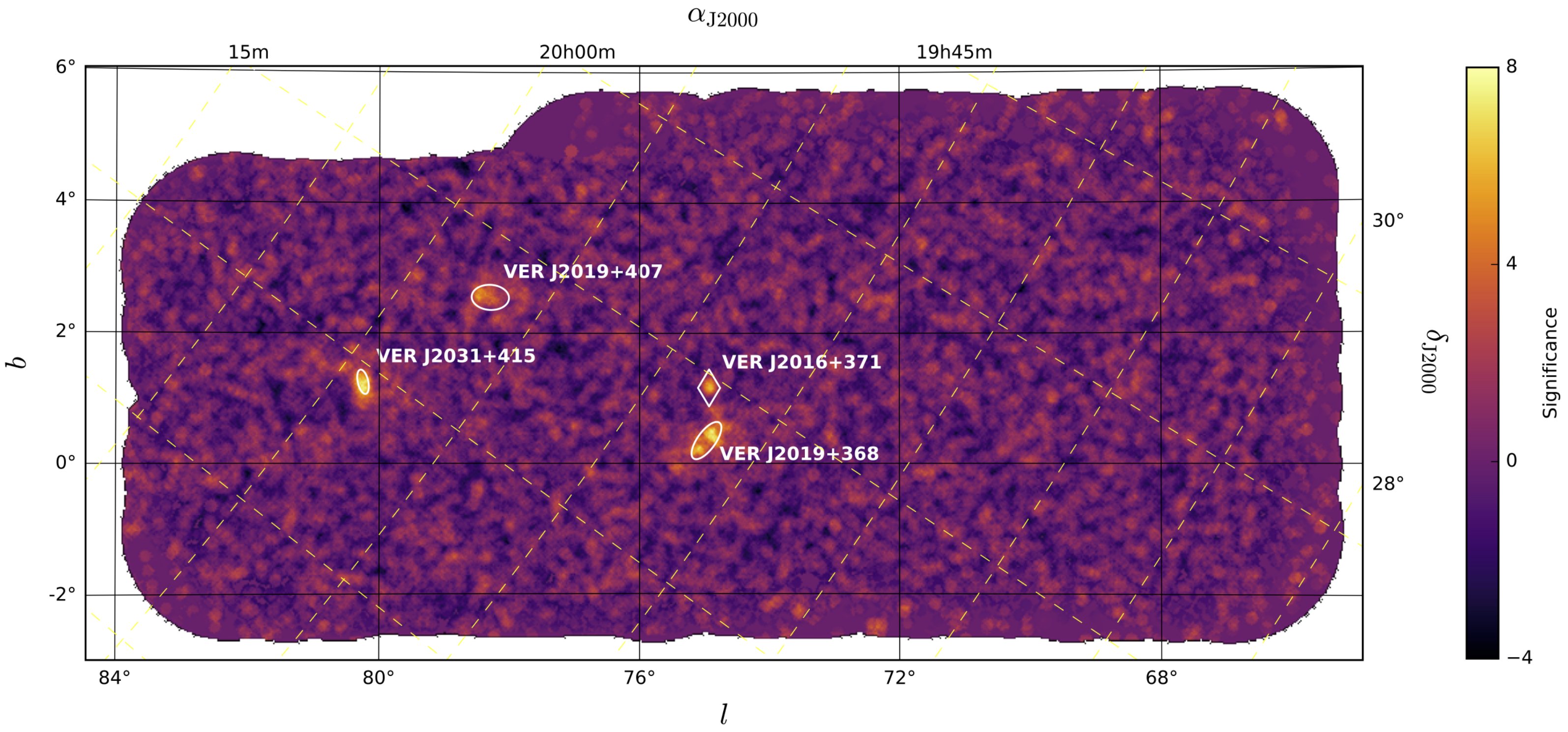

Figure 7.12: The VERITAS significance map for the Cygnus region generated using the hard cuts and the point source integration. The significance is calculated as described in Chapter 5, using the ring background method. Ellipses for the 1σ extent of the extended sources, VER J2019+368, VER J2031+415, VER J2019+407, are shown, as well as a diamond representing the position of the point source VER J2016+371.

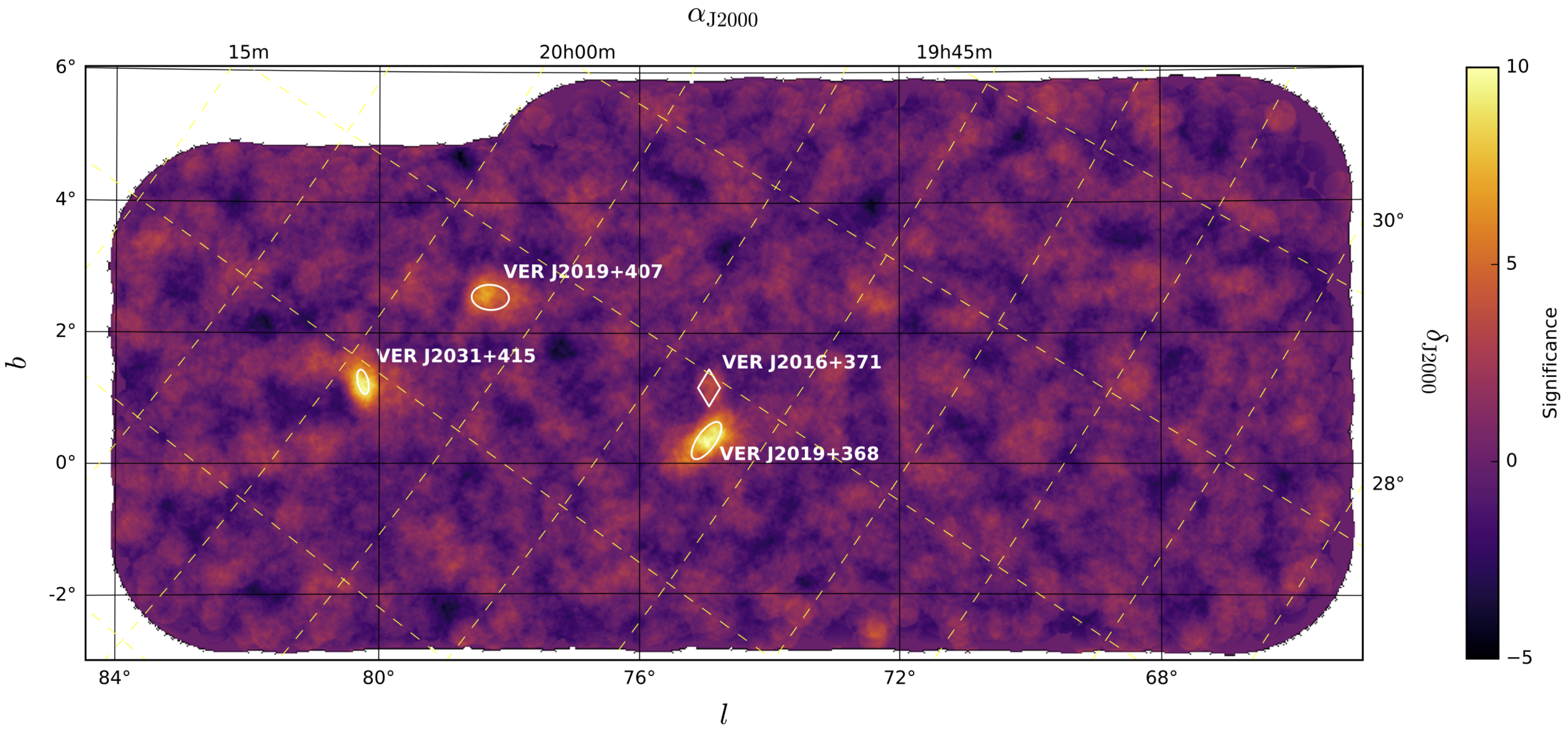

Figure 7.13: The VERITAS significance map for the Cygnus region generated using the hard cuts and the extended source (b) integration. The significance is calculated as described in Chapter 5, using the ring background method. Ellipses for the 1σ extent of the extended sources, VER J2019+368, VER J2031+415, VER J2019+407, are shown, as well as a diamond representing the position of the point source VER J2016+371.

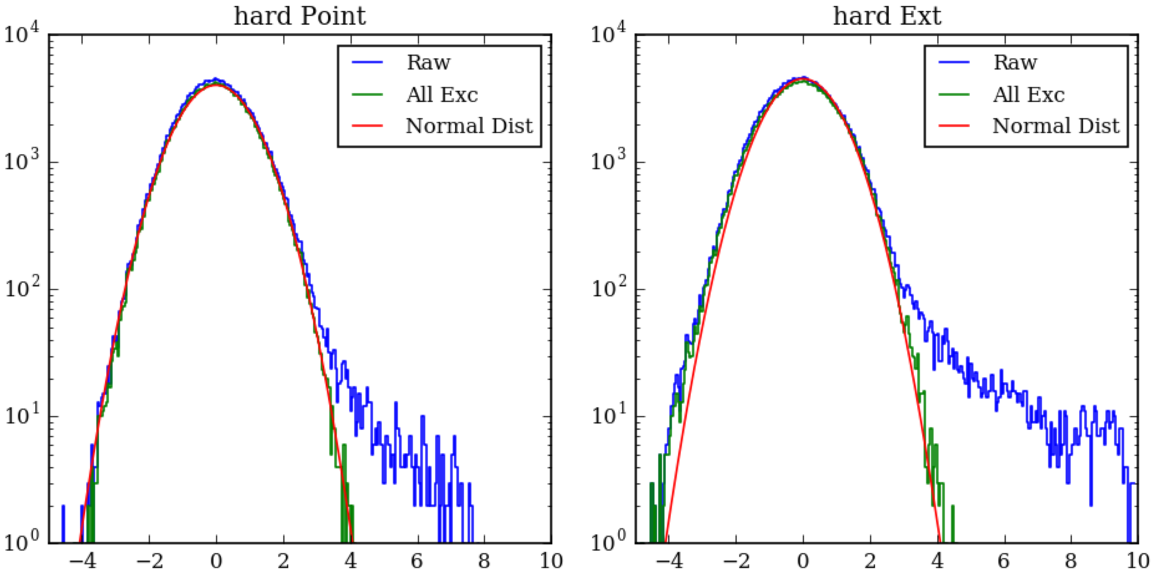

Figure 7.14: The significance distribution for the entire region hard-point source cuts (left) and hard-extended source cuts (right). The distributions in blue are for all bins and the distributions in green are with cuts for bright stars and known/measured sources; it can be seen that the distributions are consistent with normal distributions centered at 0 (red curves).

The results for the four detected sources are discussed in Section 7.6.3, and the chapter concludes with VERITAS upper limits on potential VHE sources in the region.

7.6.2 *Fermi*-LAT Sky Maps

The *Fermi*-LAT counts map for the Cygnus region is shown in Figure 7.15. In the region there are 25 3FGL catalog sources which overlap with the eight 1FHL sources and four 2FHL sources. Eight of the sources have firm associations in the catalog at other wavelengths and another two have potential source types in the catalog. 15 are associated with the Cygnus cocoon field and may reflect the poor modeling of the Cocoon diffuse emission rather than individual point sources. In particular the upper-left region of the Cygnus cocoon is poorly modeled. This can be seen in the residual map of the region after fitting the catalog and new sources (see Figure 7.16). The results for individual *Fermi*-LAT catalog sources are presented in Table 7.3. 29 new point sources in the region were identified in this analysis; these are presented in Table 7.4. Figure 7.17 shows the spectral energy distributions (SEDs) of the 3FGL catalog *Fermi*-LAT sources with TS $>$ 25 in the final fit. Figure 7.18 shows the SEDs for the newly detected sources with a TS $>$ 25 in the final fit. Also shown on the SEDs is the 10 %, 1% and 0.5% Crab Nebula flux at TeV energies. For sources not detected by VERITAS, the upper limit from Table 7.5 is shown. The sources are fit with one of three spectral types, a power law (PL, Equation (7.2)), a log parabola (LP, Equation (7.3)), also known as a curved power law, or (for pulsars only) a power law with exponential cutoff (PLEC, Equation (7.4)):

$$\frac{dN}{dE} = N_0 \left(\frac{E}{E_0}\right)^{-\alpha}, \tag{7.2}$$

$$\frac{dN}{dE} = N_0 \left(\frac{E}{E_b}\right)^{-\alpha-\beta\ln(E/E_b)}, \tag{7.3}$$

or

$$\frac{dN}{dE} = N_0 \left(\frac{E}{E_0}\right)^{-\alpha} \exp\left(\frac{-E}{E_c}\right). \tag{7.4}$$

Here, α the spectral index, N_0 the normalization, E_0 the energy normalization, E_b the energy of the spectral break for an LP spectrum, β is the modifier for that break, and E_c is the energy of the spectral cutoff for a PLEC spectrum.

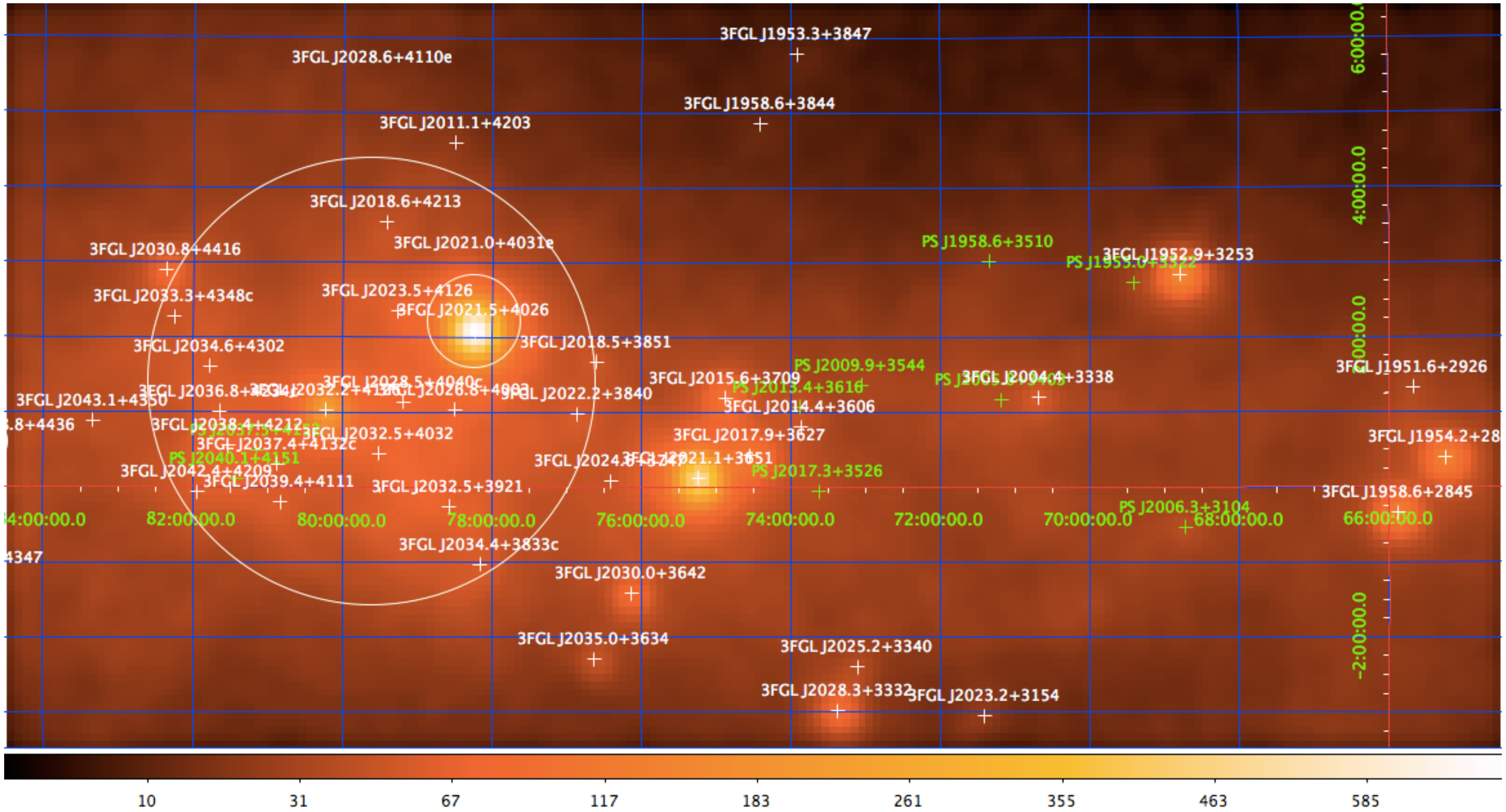

Figure 7.15: The *Fermi*-LAT counts map (square root of the number of photons) for photons > 1 GeV in the Cygnus region. The 3FGL catalog sources are labeled in green, with circles to represent the extended sources, such as the Cygnus cocoon, marked by the largest circle to the left. The new point sources are labeled in white.

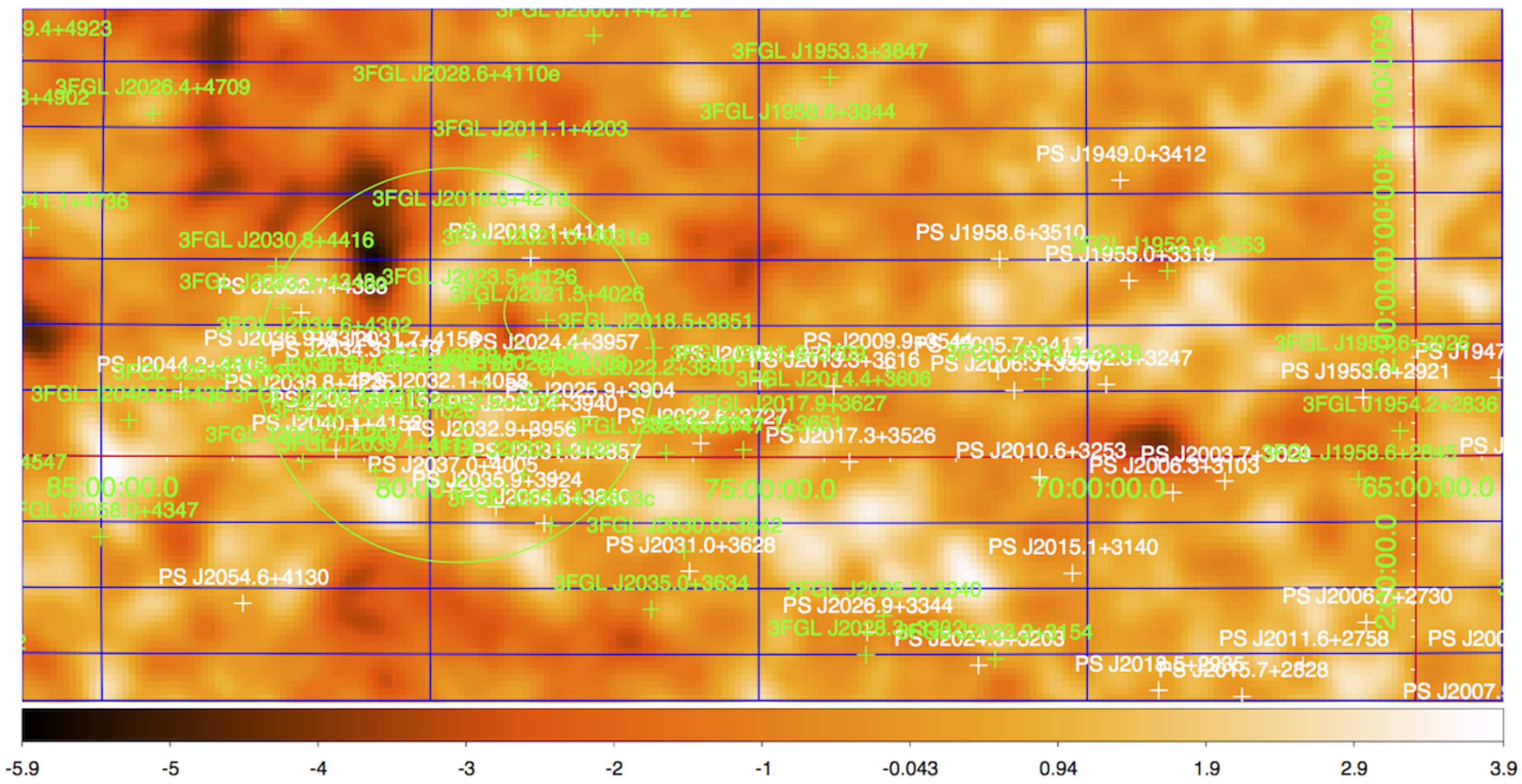

Figure 7.16: The residuals from a fit of the *Fermi*-LAT data in the Cygnus region. The 3FGL catalog sources are labeled in green, with circles to represent the extended sources. The new point sources are labeled in white. The scale (in photon counts) is from -6 to 4 meaning that the number of counts in a bin is fit fairly well. It is clear that with the large number of weak sources and the negative residual area in its upper left, the Cygnus cocoon region (marked by the largest circle to the left) is not the simple disk shape used by the model provided by the *Fermi*-LAT collaboration.

Table 7.3: The results for the > 1 GeV *Fermi*-LAT analysis for 3FGL sources that lie within the survey region. For each source, the Galactic coordinates for source are listed together with the corresponding TS value at this location. Associations as listed are from the 3FGL catalog. Source class definitions: PSR = pulsar, FSRQ = FSRQ type of blazar, BCU = active galaxy of uncertain type, SNR = supernova remnant, SRF = star-forming region. Sources marked with a * next to their name lie in the field of the Cygnus cocoon. The spectra were fit with a Power Law (PL), Log Parabola (LP), or a Power Law with Exponential Cutoff (PLEC) as defined in the text.

Source Name	l [°]	b [°]	Associations	Source Class	TS	Spectral Type	N_0 [GeV^{-1}cm^{-2}s^{-1}]	E_0/E_b [GeV]	α	β/E_c [GeV]
3FGL J1951.6+2926	65.670	1.318	None	Unknown	61.4	PL	5.93E-10 ± 8.28E-11	1.66	3.33 ± 0.26	N/A
3FGL J1952.9+3253	68.781	2.826	2FGL J1953.0+3253 PSR J1952+3252 1FHL J1953.3+3251	PSR	10959.5	PLEC	7.16E-8 ± 3.20E-9	0.67	2.05 ± 0.08	5.74 ± 0.77
3FGL J1958.6+2845	65.875	-0.352	2FGL J1958.6+2845 3EG J1958+2909 LAT PSR J1958+2846 1FHL J1958.6+2845	PSR	5378.1	PLEC	2.67E-8 ± 9.39E-10	1.02	2.22 ± 0.10	5.90 ± 1.10
3FGL J2004.4+3338	70.671	1.186	2FGL J2004.4+3339c 1FHL J2004.4+3339	Unknown	606.8	PL	4.87E-10 ± 2.63E-11	2.67	2.50 ± 0.07	N/A
3FGL J2015.6+3709[1]	74.893	1.200	VER J2016+371 1FHL J2015.8+3710 3EG J2016+3657 MG2 J201534+3710 2FGL J2015.6+3709	FSRQ	1964	LP	4.86E-9 ± 1.72E-10	1.52	2.63 ± 0.07	0.02 ± 0.04
3FGL J2017.9+3627	74.541	0.411	PSR J2017+3625 MGRO J2019+37 2FGL J2018.0+3626	PSR	1472.8	LP	4.74E-9 ± 1.83E-10	1.65	2.49 ± 0.11	0.66 ± 0.12

Continued on next page

---

[1] The values for 3FGL J2015.6+3709 quoted in this table are from the best fit location of (l, b) = (74.89°, 1.2°) ((RA, dec) = ($20^h15^m39.2^s$, 37°11'31.1")), for details of this analysis see Section 7.6.3.4.

Table 7.3 – continued from previous page

3FGL J2018.5+3851	76.593	1.664	2FGL J2018.2+3850c TXS 2016+386 1FHL J2018.3+3851	BCU	155.7	PL	7.49E-11 ± 7.77E-12	4.18	2.27 ± 0.10	N/A
3FGL J2018.6+4213*	79.402	3.531	None	Unknown	40.9	PL	5.43E-11 ± 9.77E-12	3.66	2.39 ± 0.19	N/A
3FGL J2021.0+4031e	78.241	2.197	VER J2019+407 1AGL J2022+4032 2FGL J2019.1+4040 Gamma Cygni 1FHL J2021.0+4031e	SNR	909.4	PL	2.50E-10 ± 9.92E-12	6.78	2.02 ± 0.03	N/A
3FGL J2021.1+3651	75.232	0.113	MGRO J2019+37 2FGL J2021.0+3651 1AGL J2021+3652 PSR J2021+3651 1FHL J2021.0+3651	PSR	42802.5	PLEC	1.63E-7 ± 2.76E-9	0.84	2.05 ± 0.05	5.10 ± 0.36
3FGL J2021.5+4026	78.231	2.083	2FGL J2021.5+4026 1AGL J2022+4032 LAT PSR J2021+4026	PSR	60641.2	PLEC	4.55E-7 ± 9.02E-9	0.66	2.00 ± 0.05	3.40 ± 0.20
3FGL J2022.2+3840	76.855	0.963	None	Unknown	108.4	PL	1.53E-9 ± 1.61E-10	1.45	3.73 ± 0.26	N/A
3FGL J2023.5+4126	79.253	2.342	None	Unknown	70	PL	1.66E-10 ± 2.25E-11	2.84	2.59 ± 0.16	N/A
3FGL J2025.2+3340	73.102	-2.413	None	Unknown	210.2	PL	5.45E-10 ± 4.51E-11	2.03	2.92 ± 0.12	N/A
3FGL J2026.8+4003	78.492	1.025	None	Unknown	25.4	PL	7.57E-10 ± 1.62E-10	1.39	2.75 ± 0.11	N/A
3FGL J2028.5+4040c*	79.185	1.130	None	Unknown	55.6	PL	7.69E-10 ± 1.10E-10	1.68	3.30 ± 0.27	N/A
3FGL J2028.6+4110e	79.601	1.396	MGRO J2031+41 Cygnus Cocoon 1FHL J2028.6+4110e	SFR	2233.1	PL	4.43E-9 ± 9.84E-11	3.63	2.13 ± 0.02	N/A
3FGL J2030.0+3642	76.132	-1.431	2FGL J2030.0+3640 PSR J2030+3641	PSR	1698.4	PLEC	8.77E-9 ± 1.29E-9	1.54	1.02 ± 0.27	1.90 ± 0.33
3FGL J2030.8+4416	82.349	2.890	2FGL J2030.7+4417 LAT PSR J2030+4415	PSR	1176.5	PLEC	7.75E-9 ± 2.16E-9	1.60	1.74 ± 0.39	1.92 ± 0.59

Continued on next page

Table 7.3 – continued from previous page

3FGL J2032.2+4126	80.218	1.019	TeV J2032+4130 2FGL J2032.2+4126 1AGL J2032+4102 LAT PSR J2032+4127 1FHL J2032.1+4125	PSR	7980.3	PLEC	1.26E-8 ± 4.19E-10	1.56	1.51 ± 0.08	5.36 ± 0.54
3FGL J2032.5+3921	78.573	-0.268	None	Unknown	38.8	PL	9.68E-11 ± 1.74E-11	3.13	2.53 ± 0.18	N/A
3FGL J2032.5+4032	79.513	0.438	None	Unknown	35.9	PL	9.07E-10 ± 1.59E-10	1.50	3.57 ± 0.35	N/A
3FGL J2034.4+3833c*	78.158	-1.043	None	Unknown	72.7	LP	4.32E-9 ± 0.00E+00	0.53	0.62 ± 0.00	1.10 ± 0.00
3FGL J2034.6+4302	81.767	1.604	None	Unknown	27.8	PL	3.34E-10 ± 6.68E-11	1.85	3.12 ± 0.31	N/A
3FGL J2035.0+3634	76.633	-2.315	2FGL J2034.9+3632	Unknown	448.4	LP	7.13E-10 ± 5.64E-11	2.13	1.52 ± 0.18	0.83 ± 0.15
3FGL J2036.8+4234c	81.633	0.997	None	Unknown	25.6	PL	4.29E-10 ± 8.88E-11	1.72	3.24 ± 0.32	N/A
3FGL J2038.4+4212*	81.527	0.543	None	Unknown	46.1	LP	5.68E-10 ± 1.20E-10	1.65	0.81 ± 0.20	1.57 ± 0.19
3FGL J2039.4+4111	80.829	-0.207	None	Unknown	106.6	PL	6.62E-10 ± 7.04E-11	1.87	3.02 ± 0.19	N/A
3FGL J2042.4+4209	81.932	-0.071	None	Unknown	93.8	PL	7.47E-10 ± 8.39E-11	1.75	3.18 ± 0.21	N/A

Table 7.4: > 1 GeV *Fermi*-LAT analysis results of newly identified sources. All sources were fit with a power law (as defined in the text) and showed no significant evidence of curvature. Sources marked with a * next to their name lie in the field of the Cygnus cocoon.

Source Name	l [°]	b [°]	Associations	Source Class	TS [GeV^{-1}cm^{-2}s^{-1}]	N_0 [GeV]	E_0	α [GeV]
PS J1949.0+3412	69.490	4.208	None	Unknown	38.5	6.86E-11 ± 1.28E-11	2.62	2.58 ± 0.21
PS J1953.6+2921	65.806	0.892	None	Unknown	36.1	3.34E-10 ± 5.98E-11	1.86	3.11 ± 0.27
PS J1955.0+3319	69.363	2.680	None	Unknown	53.2	1.86E-10 ± 2.86E-11	2.3	2.80 ± 0.20
PS J1958.6+3510	71.332	3.012	Cygnus X-1	HMXB	45.9	2.15E-11 ± 4.02E-12	4.78	2.29 ± 0.19
PS J2002.3+3247	69.714	1.102	G69.7+1.0	SNR	30.9	4.83E-11 ± 9.98E-12	3.46	2.49 ± 0.27
PS J2005.7+3417	71.360	1.304	None	Unknown	41.1	5.64E-10 ± 9.42E-11	1.61	3.35 ± 0.32
PS J2006.3+3103	68.703	-0.545	PSR J2006+3102	PSR	147.8	3.90E-10 ± 3.73E-11	2.16	2.87 ± 0.13
PS J2009.9+3544	73.044	1.359	None	Unknown	49.5	1.16E-11 ± 2.23E-12	6.75	2.10 ± 0.16
PS J2010.6+3253	70.727	-0.307	None	Unknown	25.7	3.31E-10 ± 6.90E-11	1.74	3.19 ± 0.38
PS J2013.3+3616	73.859	1.079	G73.9+0.9	SNR	151	5.02E-10 ± 4.65E-11	2.06	2.96 ± 0.14
PS J2015.1+3140	70.229	-1.771	None	Unknown	30.9	1.31E-9 ± 2.52E-10	1.22	4.46 ± 0.79
PS J2017.3+3526	73.619	-0.070	None	Unknown	43.4	5.89E-11 ± 1.06E-11	3.47	2.47 ± 0.19
PS J2018.1+4111*	78.470	3.029	None	Unknown	27.4	5.17E-10 ± 1.04E-10	1.62	3.44 ± 0.41
PS J2022.6+3727	75.880	0.212	None	Unknown	48.8	6.58E-10 ± 1.00E-10	1.74	3.31 ± 0.25
PS J2024.4+3957*	78.131	1.348	None	Unknown	38.9	4.88E-10 ± 8.27E-11	1.89	3.12 ± 0.25
PS J2025.9+3904	77.577	0.614	None	Unknown	34.4	1.52E-9 ± 3.01E-10	1.26	3.62 ± 0.49
PS J2029.4+3940*	78.462	0.407	None	Unknown	37.1	1.36E-9 ± 2.35E-10	1.34	3.99 ± 0.48
PS J2031.3+3857	78.098	-0.323	None	Unknown	57.1	5.88E-10 ± 8.29E-11	1.78	3.11 ± 0.24
PS J2032.1+4058*	79.815	0.753	Cygnus X-3	HMXB	40.8	3.15E-10 ± 5.30E-11	2.15	2.88 ± 0.22
PS J2032.7+4333	81.961	2.189	None	Unknown	44.4	6.64E-10 ± 1.06E-10	1.59	3.41 ± 0.39
PS J2032.9+3956*	79.077	0.027	None	Unknown	86.3	8.14E-10 ± 9.36E-11	1.77	3.20 ± 0.18
PS J2034.3+4219*	81.143	1.227	None	Unknown	46.5	4.18E-10 ± 6.57E-11	1.9	3.08 ± 0.29
PS J2035.9+3924	78.995	-0.756	None	Unknown	30	6.38E-10 ± 1.23E-10	1.57	3.45 ± 0.36
PS J2036.9+4314	82.159	1.395	None	Unknown	33.8	7.26E-10 ± 1.32E-10	1.51	3.57 ± 0.45
PS J2037.0+4005*	79.667	-0.526	None	Unknown	64.3	1.10E-9 ± 1.46E-10	1.49	3.60 ± 0.31

Continued on next page

Table 7.4 – continued from previous page

PS J2037.6+4152*	81.149	0.471	None	Unknown	90.2	4.27E-10 ± 4.90E-11	2.16	2.87 ± 0.18
PS J2038.8+4235	81.852	0.724	None	Unknown	52.4	1.79E-10 ± 2.70E-11	2.61	2.72 ± 0.19
PS J2040.1+4152	81.428	0.100	None	Unknown	114.9	2.37E-10 ± 2.54E-11	2.72	2.65 ± 0.13
PS J2054.6+4130	82.847	-2.234	None	Unknown	25.6	3.89E-10 ± 8.21E-11	1.58	3.41 ± 0.49

Sources associated with VERITAS detected sources are discussed in further detail below. Of the newly detected sources, a number have potential associations. PS J1958.6+3510 is coincident in location with Cygnus X-1. It has been previously reported at *Fermi*-LAT energies [45, 129]. PS J2002.3+3247 is 6.4" away from the center of the extended SNR G69.7+1.0. PS J2006.3+3101 is coincident with PSR J2006+3102, but we did not conduct a search for pulsations to confirm this association. PS J2013.3+3616 replaces 3FGL J2014.4+3606 in this analysis, and is associated with SNR G73.9+0.9. It is a marginally detected candidate in the *Fermi*-LAT SNR catalog [130]. Finally PS J2032.1+4058 is coincident with Cygnus X-3. The *Fermi*-LAT reports 1FGL and 2FGL, but not 3FGL sources at that location due to the variable nature of Cygnus X-3.

7.6.3 Known VERITAS Sources

7.6.3.1 TeV J2032+4130, VER J2031+415

VER J2031+415, associated with TeV J2032+4130, the first unidentified TeV source, is detected strongly with VERITAS, at a peak significance of 10.1σ (pre-trials). The VERITAS significance map is shown in Figure 7.3, with the Milagro contours overplotted. A source fitting has found that the source is an asymmetrical extended source centered at $(l,\ b)$ = $80.25^\circ \pm 0.01^\circ_{stat} \pm 0.01^\circ_{sys}$, $1.20^\circ \pm 0.01^\circ_{stat} \pm 0.01^\circ_{sys}$ ((RA, dec) = $20^h31^m33^s$, 41°34'48" (J2000)) with a semi-major axis of $0.19^\circ \pm 0.02^\circ_{stat} \pm 0.01^\circ_{sys}$ and a semi-minor axis of $0.08^\circ \pm 0.01^\circ_{stat} \pm 0.03^\circ_{sys}$. The ellipse is oriented to the northeast at an angle of $103.02^\circ \pm 3.80^\circ_{stat} \pm 1^\circ_{sys}$. The position of the centroid and the extension of the source are consistent with the already-published source VER J2031+415, whereas the orientation is slightly different than the published one.

The *Fermi*-LAT pulsar PSR J2032+4127 is well represented in the on-pulse data as a point source; when that point source is input into the total model, there is a strong residual excess in the *Fermi*-LAT data. That residual excess is shown in Figure 7.19, with the VERITAS and Milagro contours overplotted. It is detected at a TS of 194, and is measured to be an extended source of a 0.15° Gaussian radius. The centroid is consistent with the location of the pulsar.

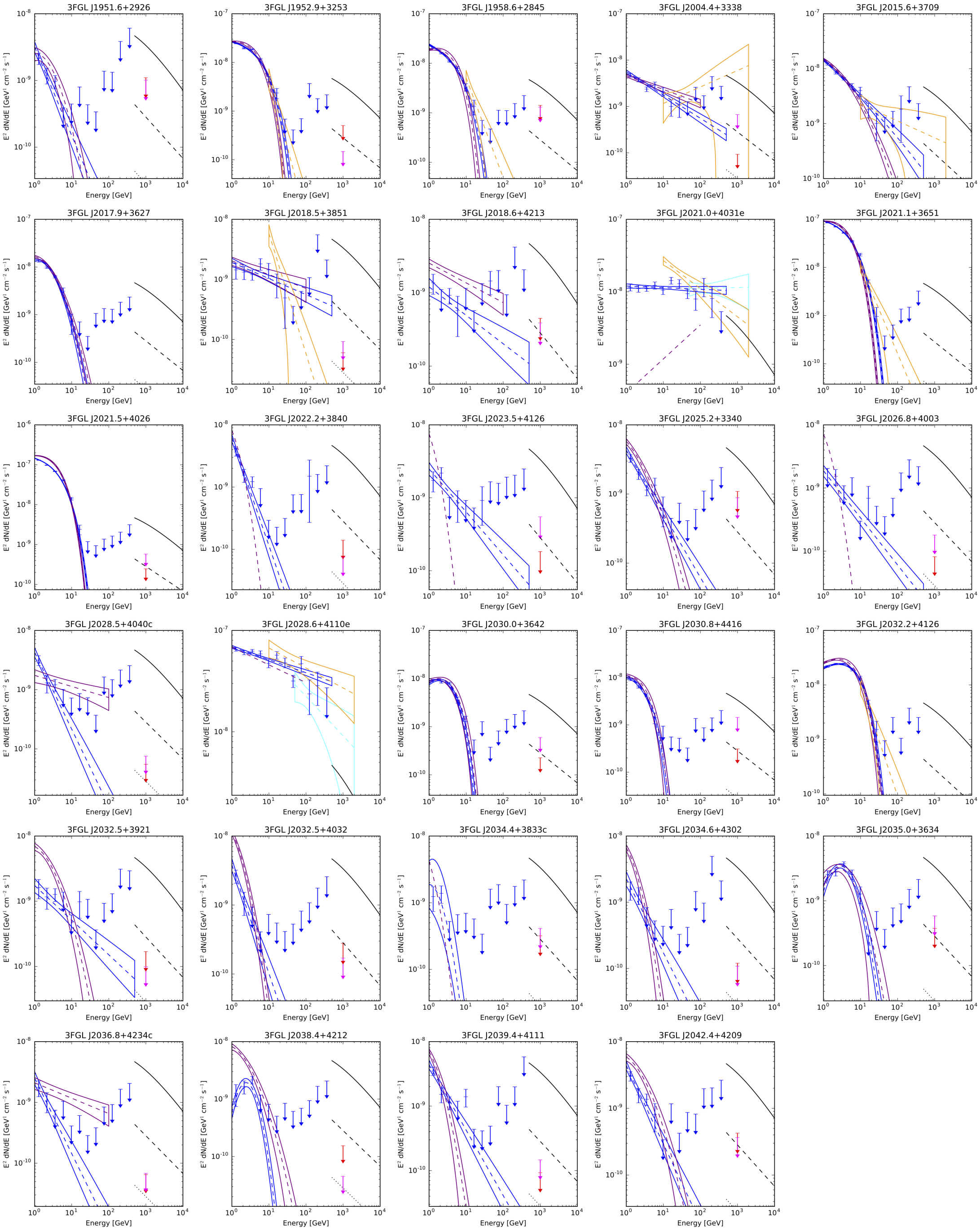
3FGL J1951.6+2926
3FGL J1952.9+3253
3FGL J1958.6+2845
3FGL J2004.4+3338
3FGL J2015.6+3709
3FGL J2017.9+3627
3FGL J2018.5+3851
3FGL J2018.6+4213
3FGL J2021.0+4031e
3FGL J2021.1+3651
3FGL J2021.5+4026
3FGL J2022.2+3840
3FGL J2023.5+4126
3FGL J2025.2+3340
3FGL J2026.8+4003
3FGL J2028.5+4040c
3FGL J2028.6+4110e
3FGL J2030.0+3642
3FGL J2030.8+4416
3FGL J2032.2+4126
3FGL J2032.5+3921
3FGL J2032.5+4032
3FGL J2034.4+3833c
3FGL J2034.6+4302
3FGL J2035.0+3634
3FGL J2036.8+4234c
3FGL J2038.4+4212
3FGL J2039.4+4111
3FGL J2042.4+4209

Figure 7.17: Spectra for all of the 3FGL catalog *Fermi*-LAT sources in the region, including sources that are identified as VERITAS sources and are discussed in detail in the next section. For all sources not detected by VERITAS, the 95% upper limits are displayed for the point source analysis in red and for the extended source analysis in magenta. The black lines represent the 10% (solid), 1% (dashed), and 0.1% (dotted) Crab Nebula spectrum, [128]. The purple butterfly is the 3FGL spectrum [59], yellow is the 1FHL [60], and cyan the 2FHL [61].

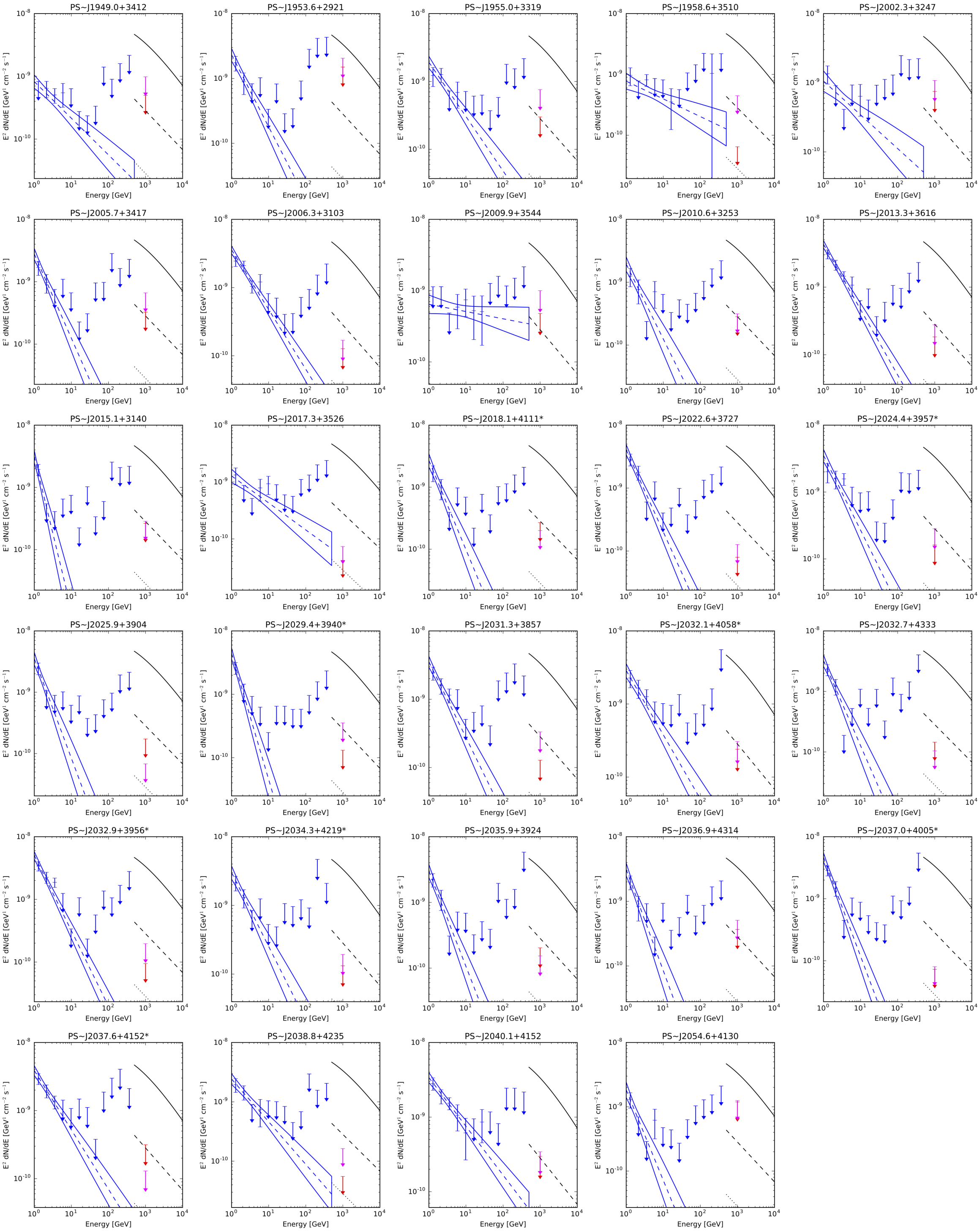

Figure 7.18: Spectra for all of the *Fermi*-LAT sources in the region, including sources that are identified as VERITAS sources and are discussed in detail in the next section. For all sources not detected by VERITAS, the 95% upper limits are displayed for the point source analysis in red and for the extended source analysis in magenta. The black lines represent the 10% (solid), 1% (dashed), and 0.1% (dotted) Crab Nebula spectrum, [128].

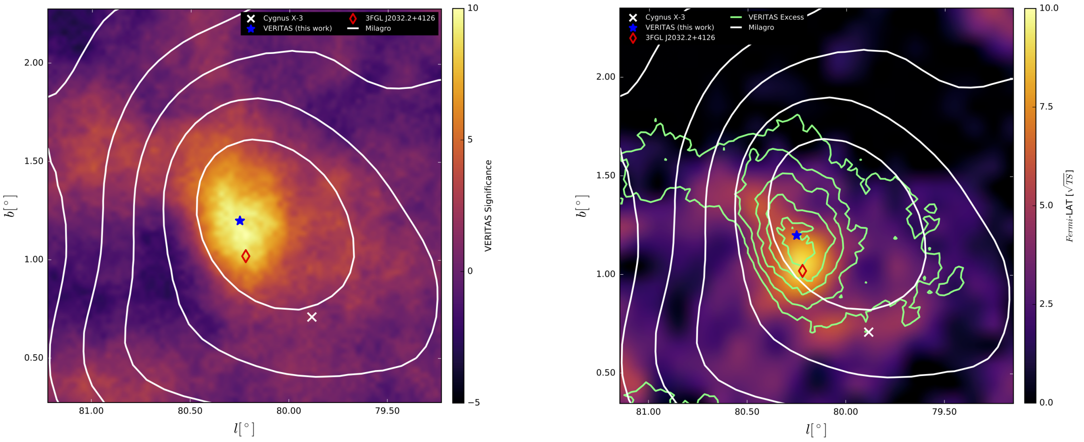

(a) VERITAS significance map

(b) *Fermi*-LAT TS map

Figure 7.19: (a) The significance map of VER J2031+415. The Milagro: 3, 4, 5, 6, and 7σ contours are plotted in white, along with the locations of other objects of interest. (b) The *Fermi*-LAT TS map of the residual source that results from the pulsed analysis, with the same Milagro contours, in white, and sources of interest, as well as the 50, 100, 150, 200, and 250 excess contours for the VERITAS source in green.

The VERITAS spectrum is well described as a power law with a normalization of $(6.92 \pm 1.48_{stat}) \times 10^{-13}\text{TeV}^{-1}\text{cm}^{-2}\text{s}^{-1}$ at 1 TeV, and an index of $-2.03 \pm 0.26_{stat}$. No evidence for a cutoff is found up to 30 TeV. The spectrum of the new *Fermi*-LAT source is described by a power law with a normalization of $1.132^{-11} \pm 2.768 \times 10^{-12}$ at 1 GeV, and an index of -2.562 ± 0.099. The spectra are shown in Figure 7.20.

7.6.3.2 γ-Cygni SNR, VER J2019+407

VER J2019+407 is detected by VERITAS at a peak significance of 7.6σ. It has previously been identified on the northwest rim of SNR G78.2+2.1, the supernova remnant associated with the γ-Cygni SNR [124]. The source morphology is determined by fitting the uncorrelated excess map with a two-dimensional, asymmetric Gaussian shape. The centroid is found to be at $(l,\, b) = (78.30^\circ{\pm}0.023^\circ_{stat}{\pm}0.01^\circ_{sys},\ 2.489^\circ{\pm}0.010^\circ_{stat}{\pm}0.01^\circ_{sys})$, ((RA, dec) = $20^h20^m04.8^s$, 40°45'36" (J2000)), with a semi-major axis of $0.287^\circ{\pm}0.023^\circ_{stat}{\pm}0.02^\circ_{sys}$ and a semi-minor axis of $0.193^\circ{\pm}0.010^\circ_{stat}{\pm}0.03^\circ_{sys}$, with the semi-major axis at an angle of $86.770^\circ{\pm}0.110^\circ_{stat}{\pm}2^\circ_{sys}$ west of north. The previously reported extent of the source is $0.23^\circ{\pm}0.03^\circ{}_{stat}$+0.04°-0.02°$_{sys}$

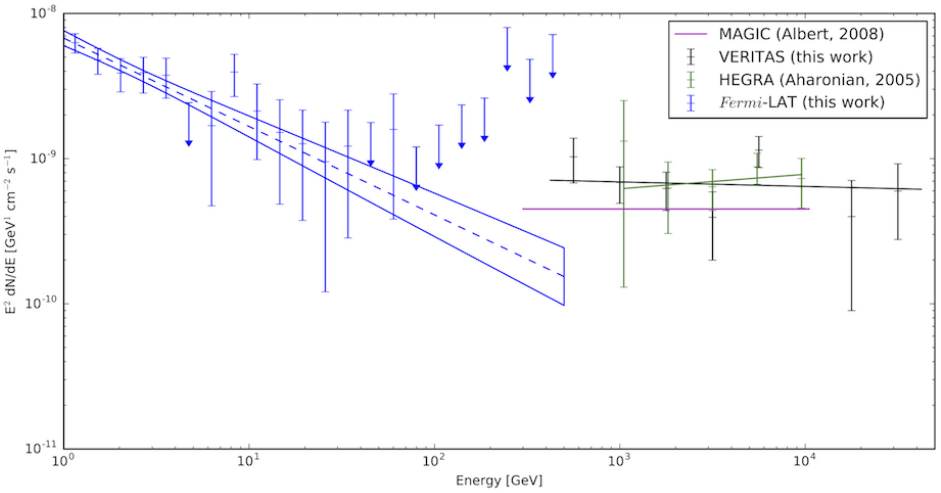

Figure 7.20: SEDs for VER J2031+415 (black) from the extended source analysis and the new *Fermi*-LAT source (blue) found from the off-pulse analysis. Also shown are the results from HEGRA [71] and MAGIC [131].

located at (RA, dec) = ($20^h20^m04.8^s$, +40°45'36" (J2000)). This position and extent are consistent with the previously published values. The contours of the VERITAS source are shown in Figure 7.21.

A recent paper has identified that, above 3 GeV, the *Fermi*-LAT emission originates from the same region as the VHE emission that was previously detected by VERITAS [133]. The *Fermi*-LAT analysis presented in this work confirms that result, as seen in the TS map (Figure 7.22) generated with the SNR source 3FGL J2021.0+4031e removed from the model and with the pulsar PSR J2021+4026 and point sources, left in the model, along with the diffuse emission components. The *Fermi*-LAT morphology is consistent with the VERITAS source location in the northern half of the remnant. The *Fermi*-LAT results also show good agreement across the whole remnant with the radio emission from the Canadian Galactic Plane Survey (CGPS), with the GeV gamma-ray emission stretching to the southern edge of the remnant as well. The origin of the differences between the VERITAS morphology and *Fermi*-LAT morphology at the southern edge is unclear. It is noted that the *Fermi*-LAT emission in the southern half of the remnant is weak and softer than in the northern part of the remnant and thus it may not be strong enough for detection by VERITAS.

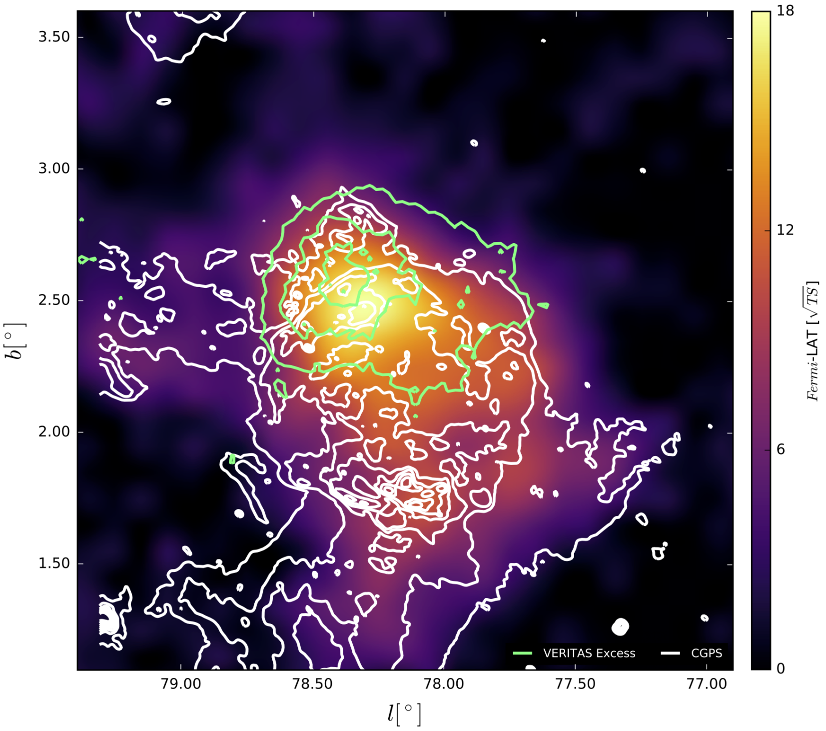

Figure 7.21: *Fermi*-LAT TS map (in color) of the region around VER J2019+407 with the pulsar source and nearby sources included in the model. The VERITAS excess contours are overlaid in green and the CGPS radio contours in white [132]. The *Fermi*-LAT and radio contours are well matched and are peaked with the VERITAS source.

Deeper observations, in particular with the lower energy threshold following the 2012 camera upgrade, may clarify this.

Figure 7.22 shows the spectrum for the entire remnant in the *Fermi*-LAT analysis (1-500 GeV) and for the portion of the remnant consistent with the VERITAS source location. The VERITAS spectrum is well described as a power law with a normalization of 1.38×10^{-15} cm^{-2} GeV^{-1} s^{-1} $\pm\, 2.17 \times 10^{-16}$ cm^{-2} GeV^{-1} s^{-1} at 1 TeV and an index of $-2.58 \pm 0.21_{stat}$. No evidence for a cutoff is found up to 30 TeV. The *Fermi*-LAT spectrum for the whole remnant is fit by a power law with prefactor $8.82 \times 10^{-12} \pm 4.26 \times 10^{-13}$ at 1 GeV and index -1.90 ± 0.03.

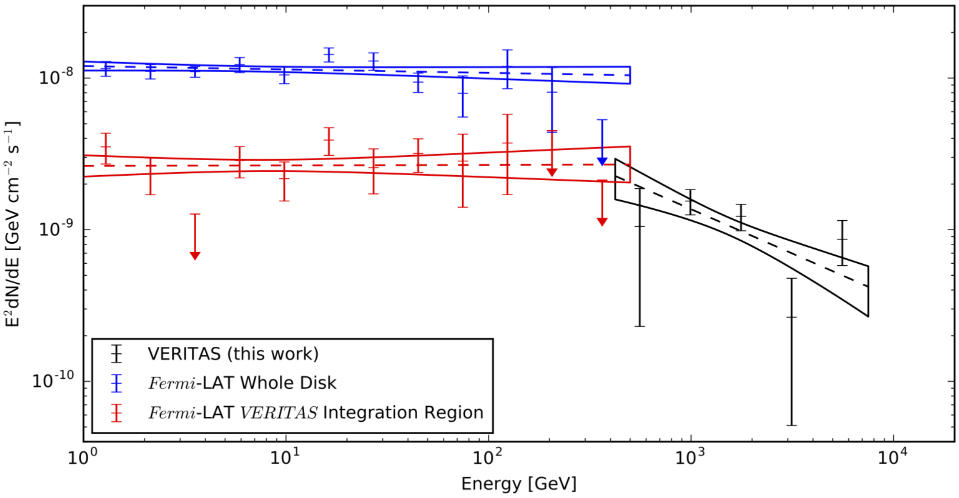

Figure 7.22: Spectra for VER J2019+407 (black), and for the various choices of *Fermi*-LAT extended source template: whole region in blue and VERITAS coincident region in red. The spectrum for the VERITAS coincident region of the *Fermi* source matches well with the VERITAS source.

7.6.3.3 Cisne, VER J2019+368

VER J2019+368, in the Cisne region, is detected at a peak significance (pre-trials) of 10.27σ using the extended analysis cuts. The source morphology is estimated by fitting with two-dimensional asymmetric Gaussian function; the best fit has its centroid at (l, b) = (74.97°± 0.02°, 0.35°± 0.01°)((RA,dec) = $20^h19^m23^s$, 36°46’44.4” (J2000)) with a 1σ angular exten-

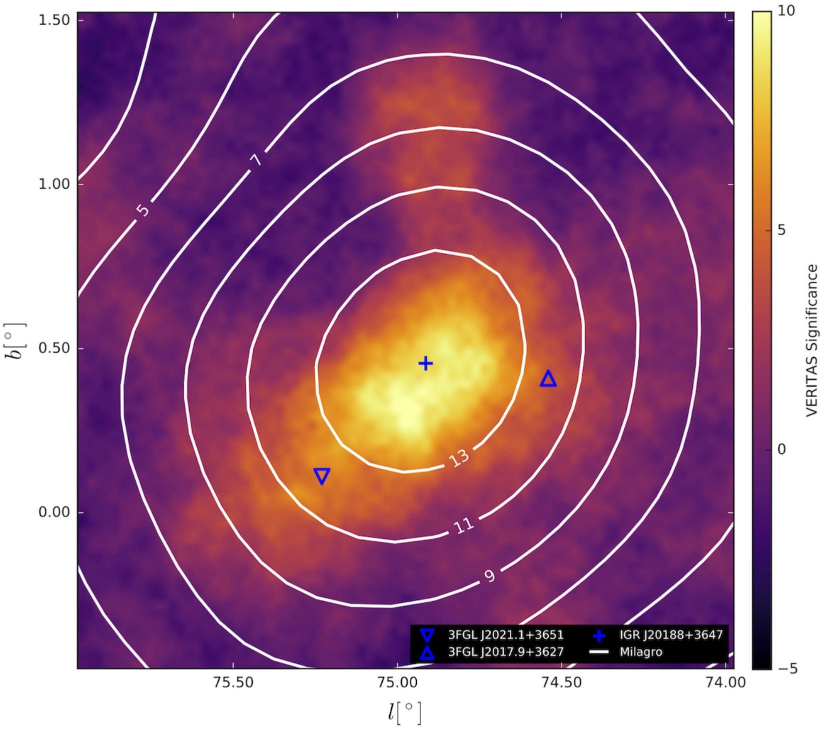

Figure 7.23: VERITAS significance sky map of the Cisne region (VER J2019+368). The Milagro contours for the region are over plotted in white, and the *Fermi*-LAT sources (and other sources of interest in the region) are labeled.

sion of 0.34°± 0.02°by 0.14°± 0.01° at an angle 54.0°± 2.6° west of Galactic north. The VERITAS source is shown in Figure 7.23.

The earlier VERITAS publication reported the potential of energy dependent morphology, with photons > 1 TeV somewhat more significant than photons < 1 TeV [126]. This is not apparent in this analysis. However, the overall emission occurs in two peaks within the whole source separated by a small dip in the significance between the two. In this analysis a two source model was not preferred over a single source. Further observations and/or improved analyses may be able to resolve this into two sources.

In the *Fermi*-LAT analysis of the region, a number of point sources are contained in the extension of VER J2019+368, and could contribute to the TeV emission in the region. These include the pulsars 3FGL J2021.1+3651 and 3FGL J2017.9+3627, the second of which was

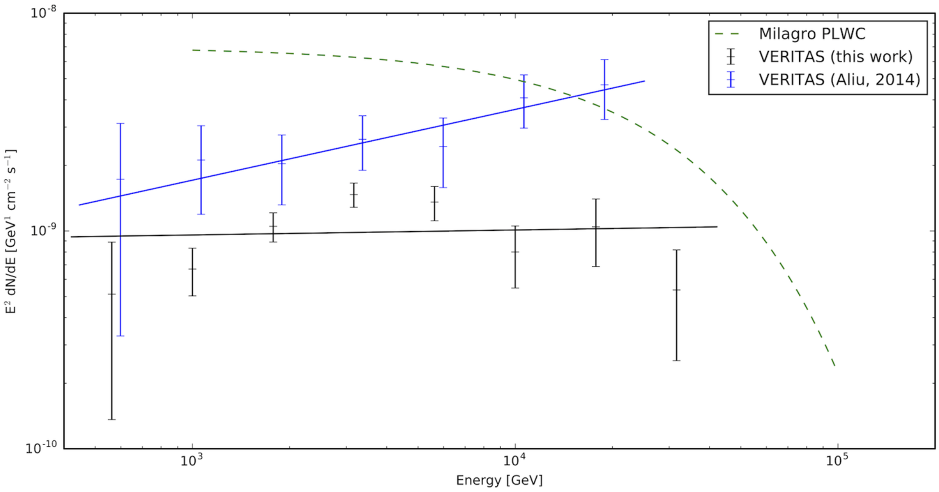

Figure 7.24: Spectrum of VER J2019+368 with VERITAS extended source analysis (0.23°) (black), also plotted are the spectrum with a 0.5° integration radius (blue) and the Milagro spectrum in green [80].

identified by Einstein@Home [134]. These could contribute to a pulsar wind nebula, but our analysis of the off-pulse emission shows that, 3FGL J2021.1+3651 does not have significant evidence of off-pulse emission. A non-detection does not rule out a weak nebula, or a pulsar wind nebula at other wavelengths, and further follow up in other wavelengths would be necessary to determine if a nebula contributes to VER J2019+368. For the second pulsar, the ephemeris was not publicly available, so the same off-pulse search was not undertaken. Also, both sources are not located near the centroid of the VERITAS emission, so we conclude the VERITAS emission could come from another source.

The spectrum measured in this analysis (Figure 7.24) is weaker and softer than that of [126], but it was determined using a different integration window (0.23° radius rather than 0.5°). There is no clear *Fermi*-LAT counterpart to this emission.

7.6.3.4 CTB 87, VER J2016+371

VER J2016+371, associated with CTB 87, is detected in this analysis at a level of 6.18σ at a location of (l,b) = (74.93°±0.01°, 1.16°±0.01°) ((RA,dec) = $20^h15^m57^s$, 37°10'24" (J2000)), see Figure 7.25. This location is just outside the statistical errors of the location quoted in our earlier paper [125] which gave a location of (RA, dec) = $20^h16^m2^s{\pm}3^s_{stat}$, 37°11'52"±40"$_{stat}$ (J2000) ((l,b) = 74.94 °, 1.14°). To determine the location and morphology of VER J2016+371, the excess map of the VER J2016+371 region was fit with a point source and with a single, symmetric Gaussian. Though the fit was slightly better with a single symmetric Gaussian, the extension is consistent with zero within statistical errors.

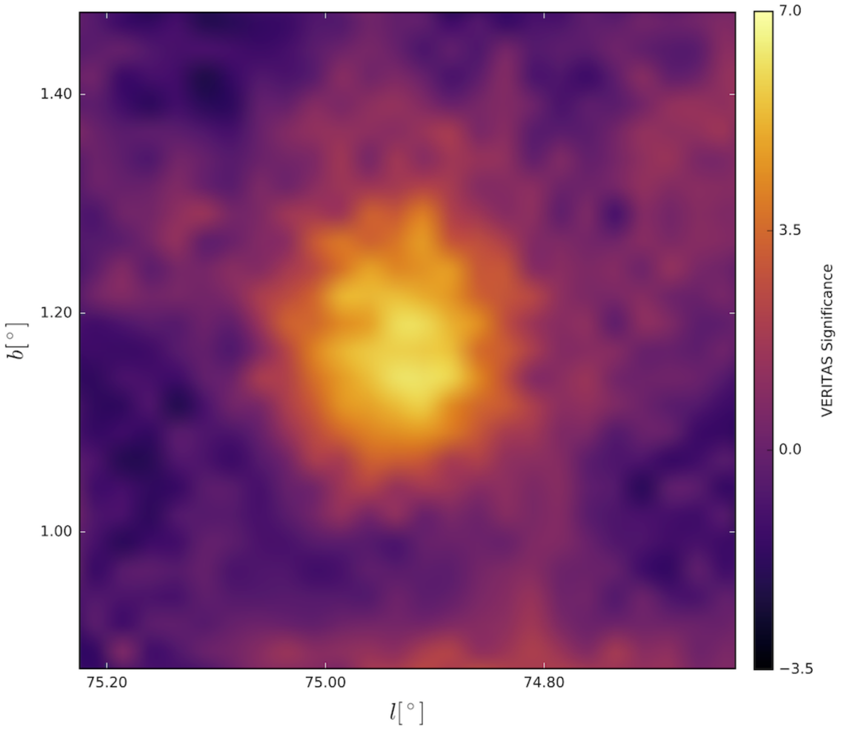

Figure 7.25: The VERITAS significance map for VER J2016+371(CTB 87) produced with hard point source cuts.

A spectral fit was conducted using all of the VERITAS data taken with four operational telescopes and a pointing offset of less than two degrees. This is a looser cut on pointing than used for the other sources, since the majority of the data were targeted at VER J2019+368 and thus have a larger offset. Figure 7.27 was produced using three logarithmically spaced bins per decade in energy and the point source integration region centered on the maximum significance location. The spectrum is best fit with a power law of normalization $(1.92{\pm}1.11){\times}10^{-09}$ TeV^{-1}cm^{-2}s^{-1} and index -2.12±0.52. This result is consistent with the previously published result (normalization = $(3.37\pm1.19)\times10^{-09}$ TeV^{-1}cm^{-2}s^{-1}, index = -2.43±0.46), given the large statistical errors associated with spectral parameters.

In the 3FGL catalog there is a source that is coincident with CTB 87 but is identified with the galaxy QSO J2015+371. In the higher energy catalogs (1FHL and 2FHL) the source shifts closer to CTB 87 and the spectrum hardens, leading to the conclusion that the two sources both contribute to the GeV gamma-ray image, but are confused due to the limited point spread function, see Figure 7.26. In the *Fermi*-LAT analysis here the source is best fit as a single point source at (l,b) = (74.89°±0.01°, 1.19°±0.01°) ((RA,dec) = $20^h15^m36^s$, 37°09'36" (J2000)) and does not have significant extension. In order to test the relative contribution of the two sources, a model was generated with point sources at the locations of CTB 87 and QSO J2015+371, and both sources were allowed to float in the likelihood fit. The TS value for the CTB 87 location is 101.84, and for the QSO J2015+371 position is 1087.37. While a two source model is not preferred over a one source model, the spectra for the two components differ, as shown in Figure 7.27. Furthermore, the component associated with CTB 87 has a spectral shape that better matches the spectrum measured by VERITAS.

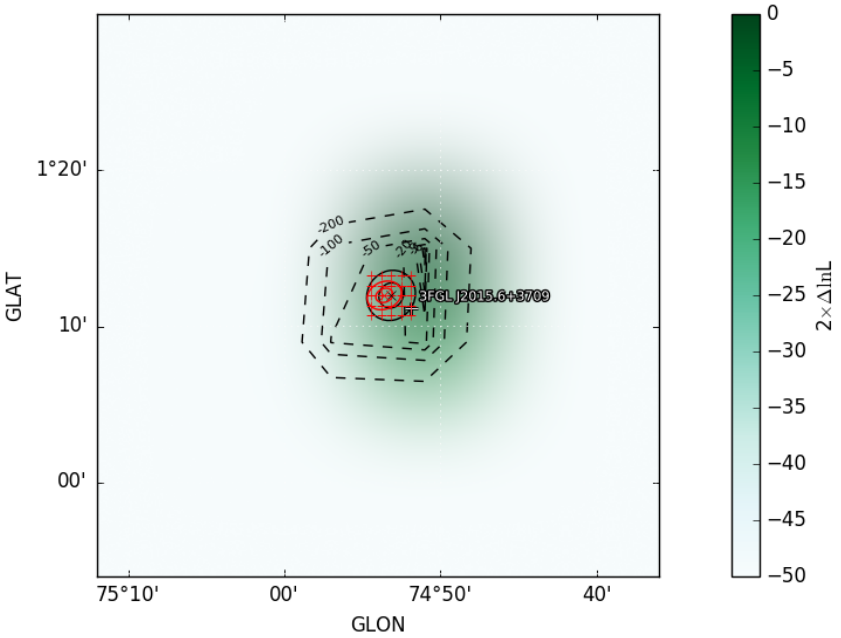

Figure 7.26: The *Fermi*-LAT TS map of 3FGL J2015.6+3709 (CTB 87). The counts contours are labeled. Marked is the 3FGL J2015.6+3709 source position and the best fit position, which is slightly offset toward CTB 87.

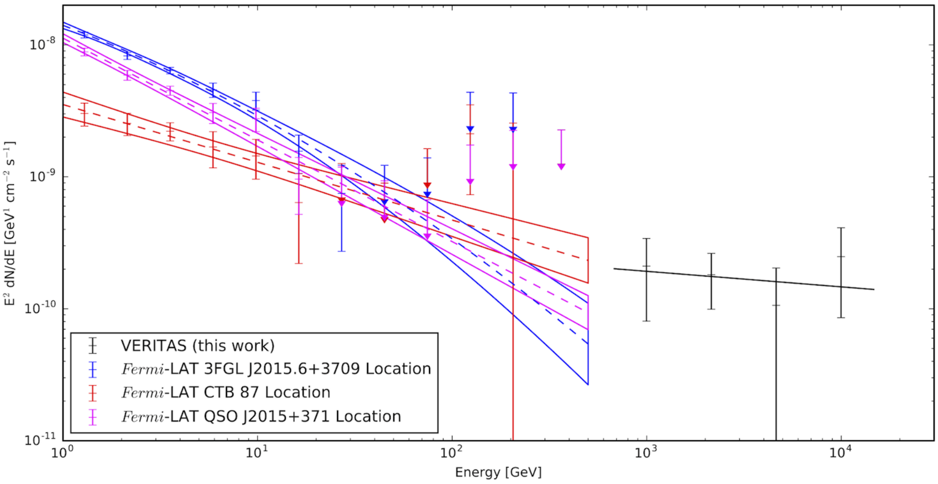

Figure 7.27: VER J2016+371 (CTB 87) spectra with *Fermi*-LAT (blue) and VERITAS (black). Also shown are the spectra for the two-source model in the *Fermi*-LAT analysis in red (CTB 87) and magenta (QSO J2015+371).

7.6.4 VERITAS Upper Limits

VERITAS upper limits were calculated for all other sources of interest in the region as defined in Chapter 3. This is not a complete list of possible sources in the region, but it covers the source classes that tend to contribute at gamma-ray energies. To review, these include: SNRs (from the Greens catalogs [41, 42]), high-mass x-ray binaries (from [50, 51]), other sources of interest, and the *Fermi*-LAT sources identified in this analysis. A table of these upper limits is presented in Table 7.5. For the *Fermi*-LAT sources, they are plotted on the SEDs in Figure 7.17.

Table 7.5: VERITAS flux upper limits on sources of inters in the Cygnus region. Both the integral and differential flux limits are calculated. The energy threshold is given in GeV, the integral upper limits are in units of $\text{cm}^{-2}\text{s}^{-1}$, the differential upper limits are in units of $\text{cm}^{-2}\text{s}^{-1}\text{GeV}^{-1}$. SNR = supernova remnant, HMXB = high mass X-ray binary, LMXB = low mass X-ray binary, CWB = particle-accelerating colliding-wind binary, BCU = active galaxy of uncertain type.

Source	$l[°]$	$b[°]$	Association	Source Class	Live	Hard Point				Hard Ext			
					Time [min]	Sig.	Energy Thresh.	Int. UL	Diff. UL	Sig.	Energy Thresh.	Int. UL	Diff. UL
3A 1954+319	68.39	1.93	4U 1954+31	LMXB	300	1.3	550	2.62E-12	1.6E-15	-0.4	550	1.83E-12	1.12E-15
3FGL J1951.6+2926	65.67	1.32	None	Unknown	323	0.2	790	1.03E-12	1.1E-15	-0.4	870	8.2E-13	1.01E-15
3FGL J1958.6+2845	65.88	-0.35	2FGL J1958.6+2845 3EG J1958+2909 LAT PSR J1958+2846 1FHL J1958.6+2845	PSR	438	1.1	660	1.75E-12	1.41E-15	0.1	660	1.61E-12	1.3E-15
3FGL J2004.4+3338	70.67	1.19	2FGL J2004.4+3339c 1FHL J2004.4+3339	Unknown	2035	-1.7	550	1.51E-13	9.32E-17	1.9	550	1.09E-12	6.68E-16
3FGL J2018.5+3851	76.59	1.66	2FGL J2018.2+3850c TXS 2016+386 1FHL J2018.3+3851	BCU	6816	-1.4	660	7.46E-14	6.03E-17	-1.3	660	1.15E-13	9.27E-17
3FGL J2018.6+4213	79.4	3.53	None	Unknown	4107	2	720	4.83E-13	4.48E-16	0.8	720	4.18E-13	3.87E-16
3FGL J2021.5+4026	78.23	2.08	2FGL J2021.5+4026 1AGL J2022+4032 LAT PSR J2021+4026	PSR	7686	1.6	660	3.04E-13	2.46E-16	3.2	660	7.16E-13	5.77E-16
3FGL J2023.5+4126	79.25	2.34	None	Unknown	8520	0.9	660	2.27E-13	1.83E-16	4.1	600	7.81E-13	5.49E-16
3FGL J2025.2+3340	73.1	-2.41	None	Unknown	423	0.5	720	1.16E-12	1.09E-15	-0.3	660	1.09E-12	8.82E-16
3FGL J2026.8+4003	78.49	1.03	None	Unknown	9450	-0.5	600	1.16E-13	8.16E-17	1.2	550	2.94E-13	1.8E-16
3FGL J2028.5+4040c	79.19	1.13	None	Unknown	10404	-0	550	9E-14	5.49E-17	1	550	1.23E-13	7.56E-17
3FGL J2030.0+3642	76.13	-1.43	2FGL J2030.0+3640 PSR J2030+3641	PSR	5852	0.9	600	3.22E-13	2.26E-16	3.1	600	8.46E-13	5.96E-16

Continued on next page

Table 7.5 – continued from previous page

3FGL J2030.8+4416	82.35	2.89	2FGL J2030.7+4417 LAT PSR J2030+4415	PSR	938	-1.2	660	3.83E-13	3.1E-16	1.2	550	2.36E-12	1.44E-15
3FGL J2032.5+3921	78.57	-0.27	None	Unknown	6492	0.1	550	2.76E-13	1.69E-16	-1.8	550	1.61E-13	9.88E-17
3FGL J2032.5+4032	79.51	0.44	None	Unknown	8280	3	550	4.55E-13	2.79E-16	0.5	550	2.78E-13	1.7E-16
3FGL J2034.4+3833c	78.16	-1.04	None	Unknown	712	-0.8	660	3.95E-13	3.19E-16	-1.1	660	5.07E-13	4.11E-16
3FGL J2034.6+4302	81.77	1.6	None	Unknown	6078	-0.4	600	1.7E-13	1.2E-16	-1.2	600	1.53E-13	1.08E-16
3FGL J2035.0+3634	76.63	-2.32	2FGL J2034.9+3632	Unknown	394	-1.7	720	4.04E-13	3.75E-16	-1.5	720	6.3E-13	5.85E-16
3FGL J2036.8+4234c	81.63	1	None	Unknown	6678	-1	600	9.17E-14	6.49E-17	-0.1	600	9.69E-14	6.82E-17
3FGL J2038.4+4212	81.53	0.54	None	Unknown	7170	1.2	600	2.19E-13	1.54E-16	-2.1	600	6.42E-14	4.52E-17
3FGL J2039.4+4111	80.83	-0.21	None	Unknown	7284	-0.3	550	1.51E-13	9.26E-17	1	550	2.39E-13	1.46E-16
3FGL J2042.4+4209	81.93	-0.07	None	Unknown	3977	1.7	720	4.58E-13	4.25E-16	0.6	660	4.5E-13	3.65E-16
Cygnus X-1	71.33	3.07	4U 1956+35 V1357 Cyg PS J1958.6+3510	HMXB	2228	-1.9	600	9.17E-14	6.47E-17	1.2	600	6.37E-13	4.47E-16
Cygnus X-3	79.85	0.7	4U 2030+407 V1521 Cyg PS J2032.1+4058	HMXB	8082	2.4	550	3.93E-13	2.4E-16	1.1	550	4.97E-13	3.05E-16
EXO 2030+375	77.15	-1.24	V2246 Cyg	HMXB	2535	0.3	600	3.96E-13	2.79E-16	2	600	1.14E-12	8.02E-16
G65.7+1.2	65.7	1.2	None	SNR	323	0.1	790	8.97E-13	9.56E-16	0.1	790	1.17E-12	1.24E-15
G65.8-0.5	65.8	-0.5	None	SNR	252	-0.6	660	1.04E-12	8.41E-16	-0.1	660	1.85E-12	1.5E-15
G66.0-0.0	66	-0	None	SNR	438	-1	720	5.38E-13	5E-16	-2.5	720	4.36E-13	4.06E-16
G67.6+0.9	67.6	0.9	None	SNR	1499	-0.2	660	3.08E-13	2.49E-16	-1.1	660	3.2E-13	2.58E-16
G67.7+1.8	67.7	1.8	None	SNR	1733	-0.4	660	2.47E-13	1.99E-16	-1.2	660	2.75E-13	2.22E-16
G67.8+0.5	67.8	0.5	None	SNR	1908	2.5	600	7.46E-13	5.24E-16	3.4	600	1.51E-12	1.06E-15
G68.6-1.2	68.6	-1.2	None	SNR	1251	-2.9	600	1.49E-13	1.05E-16	-3.4	600	2.08E-13	1.46E-16
G69.0+2.7	69	2.7	CTB 80	SNR	1880	0.6	550	5.25E-13	3.22E-16	1.2	550	1.01E-12	6.18E-16
G69.7+1.0	69.68	1.01	None	SNR	1750	5	550	1.69E-12	1.03E-15	3.1	550	1.71E-12	1.04E-15
G73.9+0.9	73.9	0.9	PS J2013.3+3616	SNR	8778	1.3	600	2.61E-13	1.84E-16	0.9	550	4.55E-13	2.78E-16

Continued on next page

Table 7.5 – continued from previous page

G76.9+1.0	76.89	0.97	3FGL J2022.2+3840	SNR	7926	0.4	600	1.98E-13	1.4E-16	-1.7	600	1.06E-13	7.46E-17
G83.0-0.3	83	-0.3	None	SNR	526	0.5	720	9.3E-13	8.67E-16	1.8	660	2.42E-12	1.96E-15
GS 2023+338	73.12	-2.09	None	LMXB	423	-0.7	600	5.64E-13	3.96E-16	0.3	600	1.3E-12	9.2E-16
HD 190603	69.49	0.39	BD+31 3925	CWB	339	1.7	660	2.23E-12	1.8E-15	-0.6	660	1.34E-12	1.08E-15
KS 1947+300	66.01	2.08	None	HMXB	441	-1.9	790	2.73E-13	2.91E-16	0.3	790	9.97E-13	1.06E-15
PS J1949.0+3412	69.49	4.21	None	Unknown	1384	1	790	4.66E-13	4.97E-16	1.6	660	1.21E-12	9.82E-16
PS J1953.6+2921	65.81	0.89	None	Unknown	505	1.6	790	1.4E-12	1.5E-15	1.6	790	1.93E-12	2.05E-15
PS J1955.0+3319	69.36	2.68	None	Unknown	2314	0.7	550	4.89E-13	3E-16	2.1	550	1.25E-12	7.59E-16
PS J2002.3+3247	69.71	1.1	G69.7+1.0	SNR	1991	3.5	550	1.22E-12	7.5E-16	3.6	550	1.76E-12	1.08E-15
PS J2005.7+3417	71.36	1.3	None	Unknown	2049	1.4	550	5.32E-13	3.26E-16	2	500	1.24E-12	6.63E-16
PS J2009.9+3544	73.04	1.36	None	Unknown	4298	3.1	550	7.81E-13	4.78E-16	4.4	550	1.65E-12	1E-15
PS J2010.6+3253	70.73	-0.31	None	Unknown	1532	0.6	550	4.62E-13	2.83E-16	-0.2	550	5.09E-13	3.14E-16
PS J2015.1+3140	70.23	-1.77	None	Unknown	899	-0.4	550	4.33E-13	2.65E-16	-1.1	550	4.68E-13	2.86E-16
PS J2017.3+3526	73.62	-0.07	None	Unknown	6660	-1.8	600	5.96E-14	4.19E-17	-1.8	550	1.19E-13	7.34E-17
PS J2018.1+4111	78.47	3.03	None	Unknown	4486	1.6	720	2.88E-13	2.68E-16	0.3	660	2.47E-13	1.99E-16
PS J2022.6+3727	75.88	0.21	None	Unknown	11004	0.4	550	1.3E-13	7.98E-17	0.9	550	2.07E-13	1.27E-16
PS J2024.4+3957	78.13	1.35	None	Unknown	8838	0.6	660	2.01E-13	1.62E-16	0.9	600	4E-13	2.82E-16
PS J2025.9+3904	77.58	0.61	None	Unknown	5596	0.1	660	2.14E-13	1.73E-16	-3.3	550	1.11E-13	6.79E-17
PS J2029.4+3940	78.46	0.41	None	Unknown	8892	-0	550	2.13E-13	1.31E-16	1.6	550	5.76E-13	3.54E-16
PS J2031.3+3857	78.1	-0.32	None	Unknown	2290	-1.2	550	2.09E-13	1.28E-16	0.3	550	5.42E-13	3.32E-16
PS J2032.7+4333	81.96	2.19	None	Unknown	1668	-1.9	600	2.06E-13	1.45E-16	-4.5	660	1.28E-13	1.04E-16
PS J2032.9+3956	79.08	0.03	None	Unknown	7422	-0.6	550	1.54E-13	9.45E-17	0	550	3.21E-13	1.96E-16
PS J2034.3+4219	81.14	1.23	None	Unknown	7560	1.2	550	2.16E-13	1.32E-16	1.5	550	3.14E-13	1.93E-16
PS J2035.9+3924	78.99	-0.76	None	Unknown	4310	0	550	3.32E-13	2.03E-16	-1.6	550	2.5E-13	1.53E-16
PS J2036.9+4314	82.16	1.39	None	Unknown	2126	0.3	660	4.56E-13	3.68E-16	0.7	660	6.3E-13	5.1E-16
PS J2037.0+4005	79.67	-0.53	None	Unknown	6714	-1.4	550	1.19E-13	7.28E-17	-2.5	550	1.31E-13	8.01E-17
PS J2037.6+4152	81.15	0.47	None	Unknown	7572	3.8	550	5.14E-13	3.15E-16	2	550	2.12E-13	1.3E-16
PS J2038.8+4235	81.85	0.72	None	Unknown	4466	-3	600	7.88E-14	5.54E-17	-0	600	2.31E-13	1.63E-16

Continued on next page

Table 7.5 – continued from previous page

PS J2040.1+4152	81.43	0.1	None	Unknown	6744	2.7	600	4.25E-13	2.98E-16	3.1	600	4.89E-13	3.43E-16
PS J2054.6+4130	82.85	-2.23	None	Unknown	237	-0.5	720	1.29E-12	1.19E-15	-0.9	720	1.35E-12	1.25E-15
PSR J1952+3252	68.76	2.82	3FGL J1952.9+3253	PSR	1933	1.9	550	8.25E-13	5.05E-16	-2.2	550	2.42E-13	1.48E-16
PSR J2006+3102	68.67	-0.53	PS J2006.3+3103	PSR	1777	-1.4	600	1.81E-13	1.27E-16	-2.1	550	2.75E-13	1.69E-16
WR 133	72.65	2.07	HD 190918	CWB	633	-1.3	600	4.56E-13	3.21E-16	-0.2	600	1.25E-12	8.78E-16
WR 137	74.33	1.09	HD 192641	CWB	6510	1.4	600	3.03E-13	2.14E-16	-0.5	600	2.45E-13	1.72E-16
WR 140	80.93	4.18	HD 193793	CWB	477	1.6	720	1.78E-12	1.65E-15	-0.3	660	1.31E-12	1.06E-15
WR 146	80.56	0.44	None	CWB	7782	2.4	550	2.53E-13	1.55E-16	2	550	3.45E-13	2.11E-16
WR 147	79.85	-0.31	None	CWB	7182	0.6	550	2.62E-13	1.61E-16	0.1	550	2.72E-13	1.67E-16
XTE J2012+381	75.39	2.25	None	LMXB	6582	0.4	660	2.04E-13	1.64E-16	-0.8	600	1.56E-13	1.09E-16

CHAPTER 8

Interpretations and Conclusions

A detailed study of the Cygnus region has been undertaken with VERITAS and *Fermi*-LAT data and it reveals clues to the nature of unidentified sources and the nature of high energy emission in the Galaxy. This chapter starts with a discussion of the findings on individual sources seen by VERITAS, followed by the conclusions that can be drawn on other sources of interest, and concludes with a discussion of the population studies that can be done with this work.

8.1 Sources

When an unidentified source is seen by both VERITAS and *Fermi*-LAT, there is more information with which to determine the nature of the source. Furthermore, for identified sources, studies of the spectra can reveal information about the acceleration processes in the source. Finally, for some of the sources that are seen by the *Fermi*-LAT and not by VERITAS, a VERITAS limit can constrain the nature of the acceleration process.

8.1.1 TeV J2032+4130, VER J2031+415

The nature of TeV J2032+4130 has been a mystery since its discovery by HEGRA [70, 71]. Numerous follow-up studies had difficulty finding potential counterparts until the *Fermi*-LAT identification of a pulsar at the location [63]. That pulsar has since been determined to be in a binary with a Be star [65]. The TeV source seems to be in a relative void in the Cygnus OB2 stellar association, lessening the likelihood that it is driven by stellar winds. The TeV emission is most likely related to a PWN associated with the *Fermi*-LAT pulsar

PSR J2032+4127, and this conclusion could be supported by the excess measured in our off-pulse analysis.

A recent paper determined that PSR J2032+4127 is in a wide orbit binary with a 15 $M_\odot$ Be star, MT91 213 [65]. The authors argue that this object probably cannot fully power the TeV emission. However, they note that if the TeV emission results from the proper motion of this long-period binary system with a massive companion star, then the increased age will lead to a smaller transverse velocity of <30 km s^{-1}, compared to 51 km s^{-1} as mentioned in [125]. The TeV emission would be expected to vary with orbital period if it were due to interactions between PSR J2032+4127 and its companion star. No evidence of variability at TeV energies with VERITAS using the Cygnus region data (from 2007-2012) was found. To investigate the nature of the VHE emission in more detail, further observations are planned during periastron in early 2018.

Multiwavelength images of TeV J2032+4130 and its vicinity are shown in Figure 8.1. The infrared images from *Spitzer* and *Herschel* are dominated by bright diffuse emission and show structures associated with star-forming activity in the Cygnus-X complex. In addition, as noted in [125], nearly all the TeV gamma-ray emission happens to be within a rare void. This is one reason that the VHE emission of TeV J2032+4130 is not thought to come from stellar wind interactions. Stellar winds from the OB stars in Cygnus OB2, a prime target for investigating stellar winds, could accelerate Galactic cosmic rays. The mechanical stellar wind energy should be enough to power the VHE emission seen in this region, but almost all of the massive stars are outside the TeV emission. It is plausible that a supernova exploded within Cygnus OB2 and its remnant expanded into the surrounding medium and cleared out the void. The size of the void would be reasonable for a remnant of the age and distance of TeV J2031+4130. The SNR has likely dissipated, and the TeV emission is related to the PWN. Furthermore, it is worth noticing that the majority of identified Galactic TeV gamma-ray sources are PWNe. The pulsar and a PWN are also seen in x-rays. Following [125], there should be a cutoff in the spectrum around 10 TeV for a PWN. However, no spectral cutoff is seen until 30 TeV, which weakens the argument for a PWN only scenario.

TeV J2032+4130 remains a complex mystery with a variety of scenarios for generating

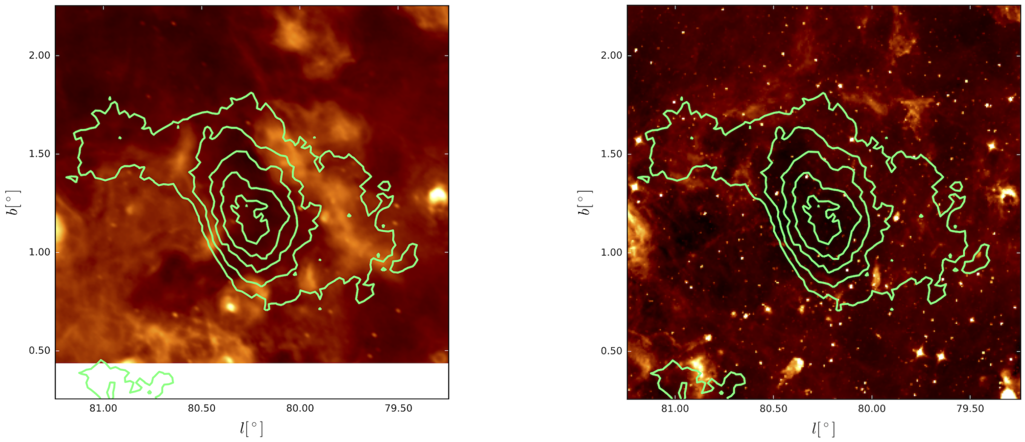

(a) 1420 MHz from CGPS

(b) Spitzer IRAC 5.8 μm

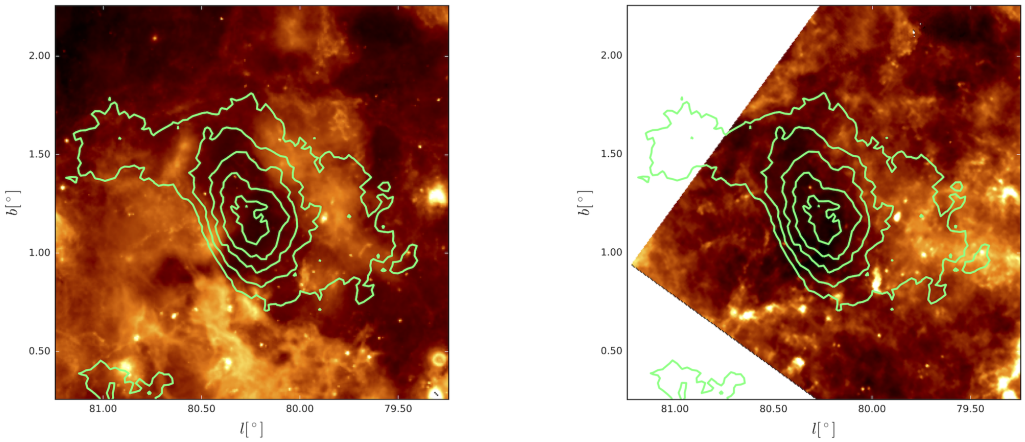

(c) Spitzer 5.8 μm from the MIPSGAL survey

(d) Herschel

Figure 8.1: The region around TeV J2032+4130 at various wavelengths, (a) radio, (b-d) infrared. It can be seen that TeV J2032+4130 is in a relative void in the region.

the TeV emission. The most promising is a PWN of the *Fermi*-LAT pulsar PSR J2032+4127, but with contributions from the other proposed scenarios to explain the spectrum extension to higher energies. The scenarios include possible contributions from either stellar winds in Cygnus OB2 or from accretion interactions as a binary with the Be star MT91 213. As a PWN it is expected to contribute to the Galactic cosmic-ray electron population.

8.1.2 γ-Cygni SNR, VER J2019+407

The association of VER J2019+407 is firmly associated with the γ-Cygni SNR, SNR G78.2+2.1. That association is consistent with the *Fermi*-LAT analysis. It is therefore not likely a PWN associated with the bright pulsar PSR J2021+4026 [133]. It has been suggested that SNRs power the Cygnus cocoon emission seen by *Fermi*-LAT; however, the emission is probably not driven by a single bright SNR like that in γ-Cygni. The results of this analysis are consistent with the previously published results of [133] who report that the gamma-ray spectrum could be fit by either leptonic (with a mix of bremsstrahlung and inverse Compton gamma-ray production) or hadronic (but with a requirement of a broken power law spectrum of cosmic-ray protons) production scenarios.

Interestingly the HE and VHE emissions are concentrated in the northern half of the remnant, where the gas is less dense. This also a region that has a lot of source confusion, so there could be other components to the emission.

2XMM J202131.0+402645 is a promising counterpart to the pulsar [135] likely born in the SNR explosion that created γ-Cygni. A projected kick velocity of a few hundred km/s is reasonable. The distance to the pulsar of 1 kpc and distance of the pulsar to the remnant center are consistent with pulsar proper motions. The adiabatic age of SNR, determined from its size (30') and its distance (1.5 kpc), is estimated to be 6.6kyr [136]. This is consistent with the optical age of the pulsar reported in [37]. The pulsar spin down age is 77 kyr, but pulsars can be younger than the spin down age would imply.

This work is in agreement with the previous studies and draws similar conclusions: that the γ-Cygni SNR and PSR J2021+4026 are from the same event and that the remnant is interacting with a large amount of material in a region of the Galaxy notable for freshly accelerated cosmic rays. The remnant is expected to be capable of accelerating protons, but greater spectral coverage is needed to measure the pion signature.

8.1.3 Cisne, VER J2019+368

The Cisne region has been a mystery since its discovery as a region of VHE emission by Milagro [18]. VERITAS resolved the point source CBT 87 discussed in the next section as separate from the rest of the region. The remainder of the emission detected by VERITAS is concentrated on the large, extended source VER J2019+368. The current study was not able to definitively determine that VER J2019+368 is more than one source. It is therefore harder to determine the most likely of the many possible counterparts.

The *Fermi*-LAT analysis undertaken in this work identifies the known pulsar sources, but does not find off-pulse emission and thus doesn't provide clues to the origin of VER J2019+368. The most likely scenario could be a source with contributions from PSR J2021+3651 and the H II region Sh2-104; with a potential contribution from PSR J2017+3625. The multiwavelength view of the region is shown in Figure 8.2. The *XMM* view from [126] sees a bright point source associated with a PWN around PSR J2021+3651. Furthermore, a recent paper reports a bright point source seen by NuSTAR associated with SH2-104 this region is also bright in the CGPS [137]. These studies have been unable to determine a clear counterpart to VER J2019+368.

8.1.4 CTB 87, VER J2016+371

The VERITAS source VER J2016+371 is associated with CTB 87, but is also positionally consistent with QSO J2015+371. There is a 3FGL source associated with the active galaxy, but at higher energies (in the 1FHL and 2FHL catalogs) the source is associated with CTB 87, a PWN. The *Fermi*-LAT analysis in this region can break down into the two sources based on the radio positions, as shown in Figure 7.27. Figure 8.3 shows the XMM view of the region with the radio excesses of CTB 87 and QSO J2015+371 from the CGPS 1420

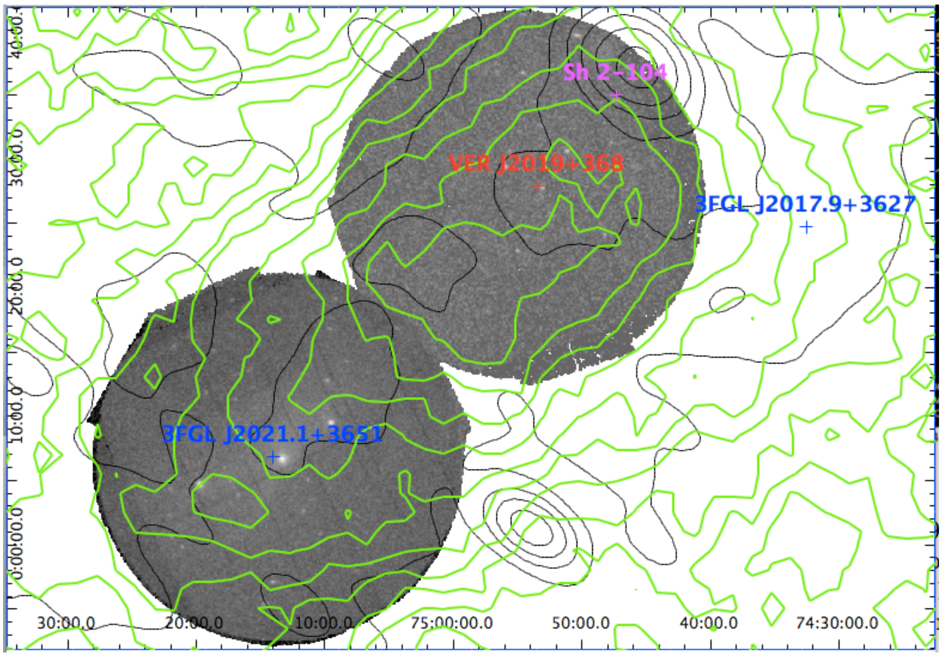

Figure 8.2: The multiwavelength picture around VER J2019+368. The VERITAS excess contours are shown in green, and the CGPS 408 MHz contours are in white. The XMM pointings are in grayscale, with a bright point source at the location of PSR J2021+3651. The NuSTAR observations reveal a number of point sources, marked in orange.

MHz view. There are also x-ray sources associated with both CTB 87 and QSO J2015+371, as well as weaker sources of non-thermal radiation in the region.

Our examination of CTB 87, and the *Fermi*-LAT source 3FGL J2015.6+3709 confirm that the VHE is consistent with the PWN. Furthermore we showed that 3FGL J2015.6+3709 is likely made up of two overlapping components; one associated with the QSO J2015+371, and one associated with CTB 87. We were then able to see that the spectrum of the CTB 87 component matches will the VERITAS spectrum; see Figure 7.27.

8.1.5 Other Sources of Interest

This work has detected *Fermi*-LAT sources associated with other sources of interest and has set VERITAS upper limits on those sources. The *Fermi*-LAT extrapolations identify that a few of the 3FGL or new point sources in the region could be seen at the few percent Crab Nebula flux level in deeper observations by VERITAS. The microquasars Cygnus X-1 and Cygnus X-3 have now been detected as steady sources, and ongoing study is required to

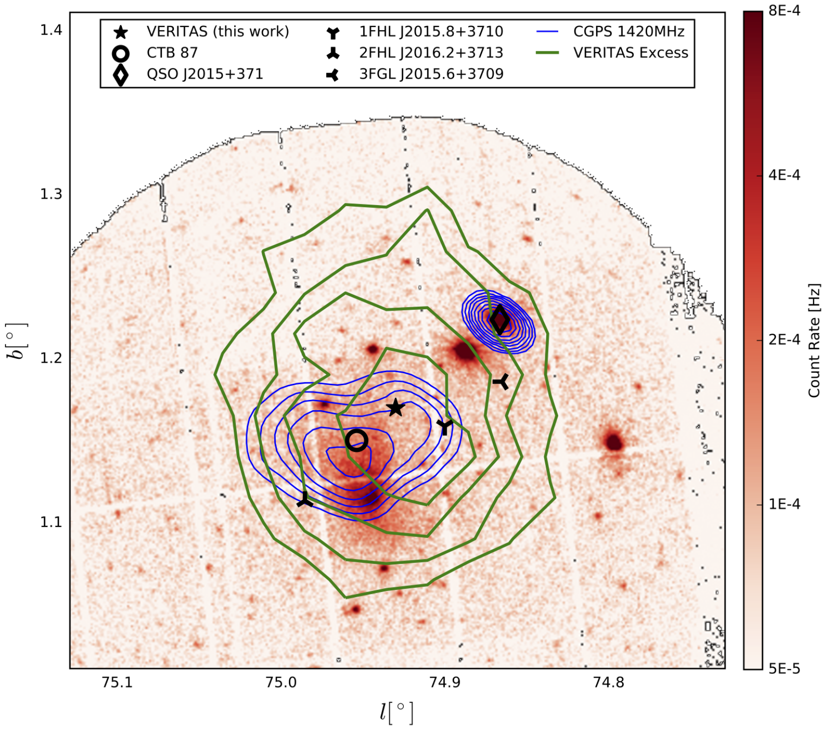

Figure 8.3: The XMM (observation id. 0744640101) counts view of the region around CTB 87 (VER J2016+371). The VERITAS contours are in green, and the radio contours from the CGPS 1420 MHz observations are in blue. The locations of relevant sources of interest are marked.

determine if their flaring states could produce VHE emission. Overall the VERITAS upper limits have an average value that is higher than expected for photons drawn from a normally distributed background. This either hints at excess VHE gamma rays in the region, but it could also be related to systematic uncertainties.

The new *Fermi*-LAT sources PS J2002.3+3247 and PS J2013.3+3616 are associated with SNRs G69.7+1.0 and G73.9+0.9 respectively. There is a probability that new and/or weak sources in the *Fermi*-LAT analysis could be substructure of the Cygnus cocoon, or related to an incomplete understanding of the Galactic diffuse emission.

8.1.6 Source populations in the Cygnus Region

The Cygnus region is bright in gamma rays and is a possible close analog to the inner regions of the Galaxy. The region contains four sources detected in VHE gamma rays. There are 37 *Fermi*-LAT catalog sources in the region, and a further 36 new sources identified in this analysis. The 3FGL sources include: nine pulsars, one SNR, one star-forming region, three special type sources (likely SNR or PWN), and 13 unidentified sources. The new sources include possible associations with the Cygnus X-1 binary and SNR G73.9+0.9. The following comparisons are made only considering *Fermi*-LAT sources in the 3FGL, 1FHL, and 2FHL catalogs.

In order to compare the Cygnus region to the inner Galaxy, it is useful to consider the sources detected by the H.E.S.S. Galactic plane survey. In the region surveyed by H.E.S.S. (from 250° to 65° in Galactic longitude and from -3.5° to 3.5° in Galactic latitude) they detected 56 sources [84]. An up-to-date list of sources is maintained at the H.E.S.S. source catalog [88], of which a large fraction are still unidentified. The average sensitivity for their survey is approximately 2% Crab Nebula flux, and it varies over the region. In the *Fermi*-LAT 3FGL catalog there are 339 total sources in the region covered by H.E.S.S.: 3 binaries, 49 pulsars, 9 PWN, 15 SNRs, 31 special type sources, 12 extragalactic sources, 2 associated with globular clusters and 218 unidentified.

As a back-of-the-envelope check, we can estimate whether the fraction *Fermi*-LAT sources detected in the Cygnus region roughly matches the fraction detected in the H.E.S.S. survey region, 339. The fraction of *Fermi*-LAT sources that are detected as VHE sources in the inner Galaxy is estimated to be $\frac{56}{339} \approx 16.5\%$. Then the number of VHE in Cygnus region would be expected to be 16.5% of 37, or about six VHE sources. There are a number of caveats to this simple approach that uses the H.E.S.S. region as an analog for the Cygnus region. In particular, it does not take into account the depth of the surveys relative to each other, the actual fraction of VHE sources detected by *Fermi*-LAT, or the distance to the sources of interest in the regions.

Another possible check would be to use the populations of *Fermi*-LAT sources in the 1FHL and 2FHL catalogs. In the Cygnus region in the 1FHL catalog there are 9 detected sources: 4 pulsars, 1 star forming region (the Cygnus Cocoon), 1 SNR (the γ-Cygni SNR), 1 unidentified source, and 2 associated with extragalactic objects (one of which is the source positionally coincident with CTB 87). In the H.E.S.S. region there are 53 detected sources: 8 SNRs, 6 PWNe, 5 special type sources (as above), 13 pulsars, 1 luminous blue variable star (Eta Carinae), 7 sources with extragalactic associations, and 13 unidentified sources. Following the estimation from the previous paragraph, we can estimate the fraction detected at VHE energies to be $\frac{56}{53} \approx 100\%$. Therefore, with the same caveats as above, the number of VHE sources in the Cygnus region is estimated to be 9. There are only 3 sources detected in the Cygnus region in the 2FHL catalog: 1 associated with Cygnus Cocoon emission, 1 associated with the γ-Cygni SNR, and 1 associated with CTB 87 (and positionally coincident with the lower energy source associated with QSO J2015+371). In the inner Galaxy (H.E.S.S.) region there are 40 sources in the 2FHL catalog: 10 SNRs, 11 PWNe, 4 special type source (as above), 10 unidentified sources, 2 binaries, 2 extragalactic sources, and 1 pulsar. In this case, our procedure's estimate matches the number of VHE sources detected in the Cygnus region, expecting $3 \cdot \frac{56}{40} \approx 4$. It is interesting that even without accounting for source type, the ratio arguments give reasonable values. In particular the high energy 2FHL catalog gives the right number of sources. This hints at similarities in VHE sources between the Cygnus region and the inner Galaxy when accounting for the sources seen at high energies by the *Fermi*-LAT.

The spatial distribution of HE and VHE sources in the Galaxy is shown in Figure 8.4 and Figure 8.5. The Cygnus region sources are consistent with the source types commonly seen in the HGPS, that is largely SNRs and PWNe. The view of the sources at their relative positions in the Galaxy are shown in Figure 8.6.

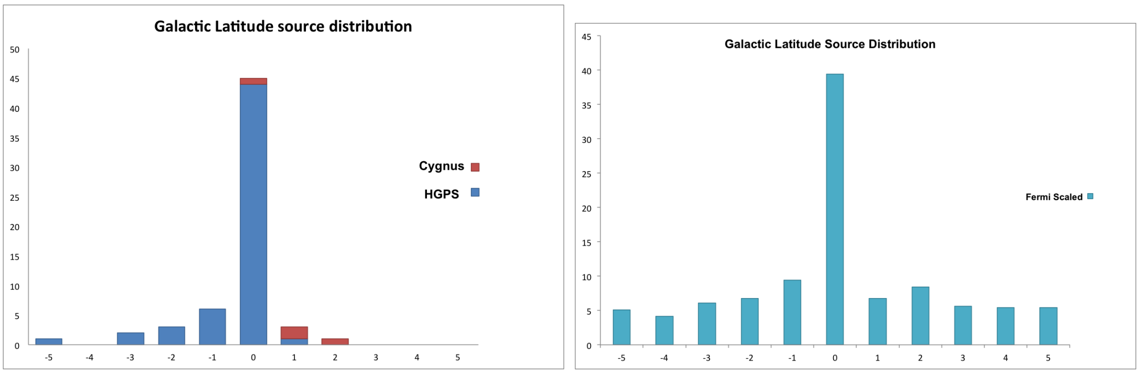

(a) Galactic Latitude Source Distribution for VHE Sources

(b) Galactic Latitude Source Distribution for *Fermi*-LAT sources

Figure 8.4: The distribution of VHE and HE sources in Galactic latitude. The Fermi source distribution is from the 3FGL catalog and is scaled by 16.5% as described in the text for the ratio of HE sources from the 3FGL catalog to VHE sources.

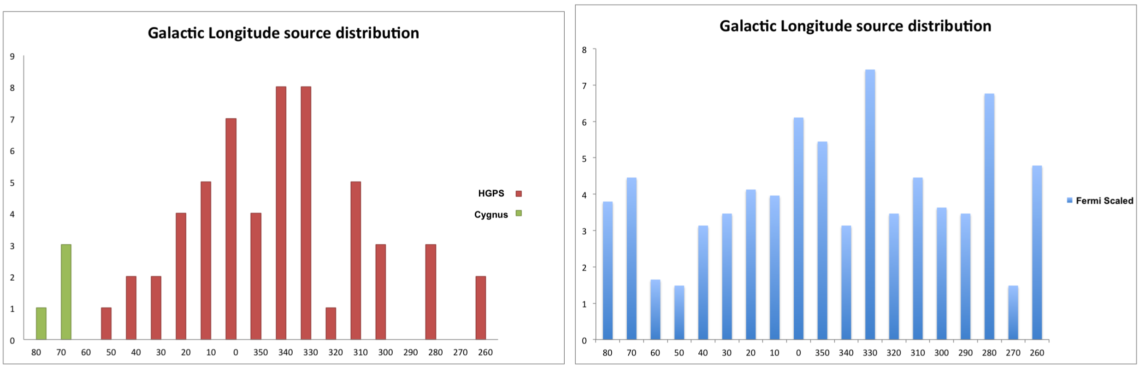

(a) Galactic Longitude Source Distribution for VHE Sources

(b) Galactic Longitude Source Distribution for *Fermi*-LAT sources

Figure 8.5: The distribution of VHE and HE sources in Galactic longitude. The Fermi source distribution is from the 3FGL catalog and is scaled by 16.5% as described in the text.

A log(N>S)-logS plot can be used to evaluate the cumulative number of sources detected for a given telescope sensitivity. In the case of a uniformly distributed source population the expected relationship is $N(>S) \propto S^{-3/2}$, where $-3/2$ is the index. The plot for the HGPS is shown in Figure 8.7. It shows that their measured index 1.2. this can give us an idea of

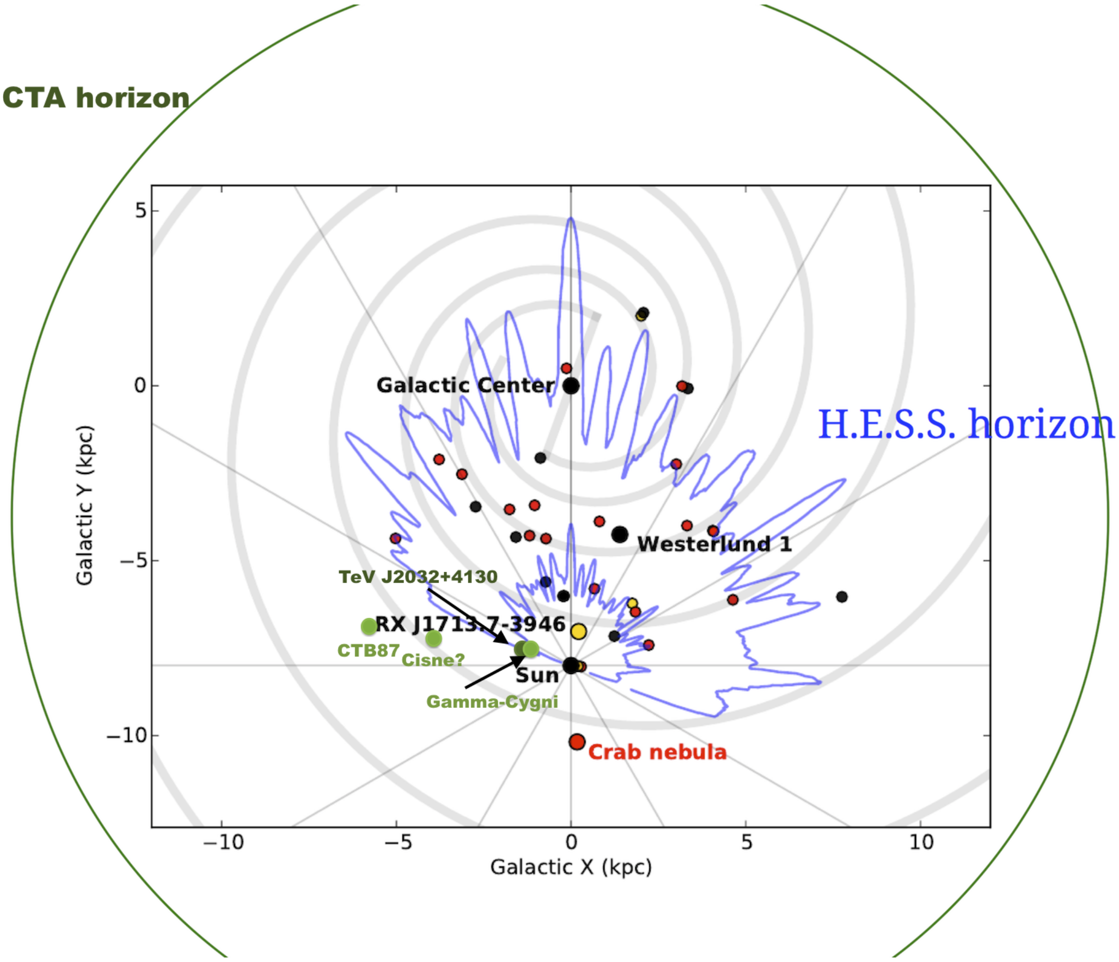

Figure 8.6: Overhead view of the Galaxy with VERITAS (green) and H.E.S.S. (other colors) source positions overlaid. Adapted from [138].

the source distribution in the Galaxy and can be used to estimate the number of expected sources from a deeper Cygnus region survey.

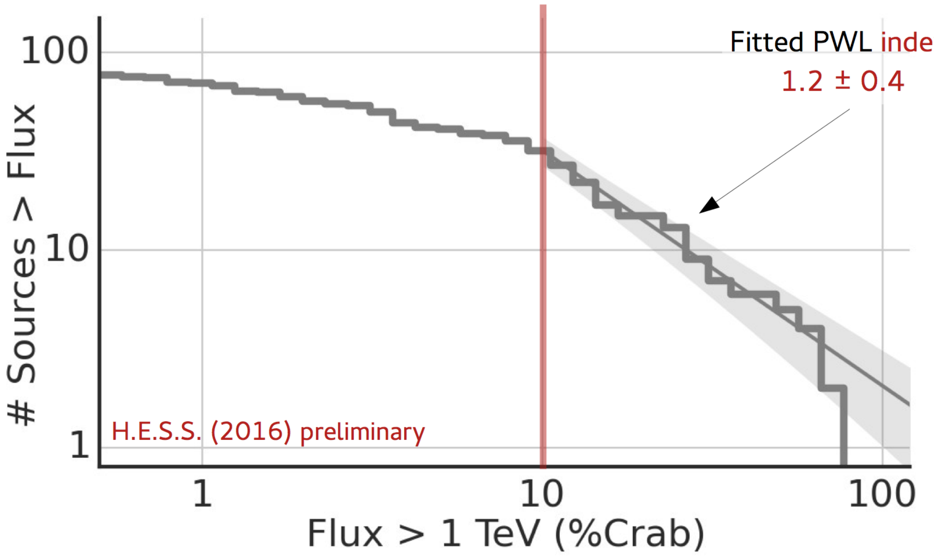

Figure 8.7: The log(N>S)-logS plot from the HGPS [139].

Once the flux (F) and distance (d) of an astrophysical source is known it is possible to compute the luminosity (L) of the source, or energy emitted per unit of time. Under the simple assumption that the source radiates equally in all directions, the relationship is:

$$L = F4\pi d^2. \tag{8.1}$$

This is a way to consider the inherent brightness of the astrophysical source, and compare with similar sources. At this time the luminosity results for the HGPS are not available for direct comparison. The fluxes and luminosities of the Cygnus region sources are presented in Table 8.1. As a comparison the Crab Nebula is one of the brightest TeV sources with a luminosity of $\approx 10^{38}$ erg/s at TeV energies.

A key distinction between the observations undertaken by *Fermi*-LAT and IACTs (VERITAS and H.E.S.S.), is the differing field-of-view. Currently IACTs are limited in being able to resolve sources larger than their field-of-view. The *Fermi*-LAT is able to see a large fraction of the sky at a time, and it is therefore capable of measuring very extended sources and large scale Galactic emission. In the case of the Cygnus cocoon, the size of the source (3°) is

Table 8.1: Summary of fluxes of the Cygnus region sources with know distance and luminosity. The integral flux is calculated in the range from the energy threshold of the data used to determine the spectrum to infinity.

Name	Integral Flux [photons cm^{-2}s^{-1}]	Flux in % Crab Nebula Flux	Distance [kpc] if known	Luminosity [erg/s]
VER J2031+415	1.63×10^{-12}	2	1.8	1.47×10^{34}
VER J2019+407	3.38×10^{-12}	4	1.7	2.15×10^{33}
VER J2019+368	2.29×10^{-12}	3	*	*
VER J2016+371	2.69×10^{-13}	0.7	6.1	1.45×10^{34}

the same size as the field-of-view of VERITAS, and therefore our standard analysis cannot resolve this source.

8.2 Conclusions

Further VERITAS observations of the Cygnus region are ongoing, and have the capability to expand our knowledge of sources in the region, by either detecting weak sources or setting limits on *Fermi*-LAT sources. Furthermore, current and future experiments bring the capabilities for expanded studies of the region. The HAWC experiment continuously surveys the northern sky and has been gathering data in the region since 2015. It is expected to have the capability to detect hard spectrum, extended sources in the coming years. VERITAS would then be capable of doing pointed follow-up observations on new sources at lower energies to connect to *Fermi*-LAT energies. Furthermore advanced analysis techniques such as boosted decision trees for gamma-hadron separation and better image fitting can be applied, further more the data set can be expanded to include data collected since 2012. In the future CTA, currently in the pre-construction stage, will undertake survey observations of the Galactic plane from both the northern and southern hemisphere with greatly improved sensitivity and improved angular resolution.

From the perspective of other techniques, such as Laser Interferometer Gravitational-Wave Observatory (LIGO) and IceCube offer views of astrophysical objects in cutting edge multi-messenger approaches. LIGO is a gravitational-wave detector with two laser interferometers – one in Haverford, WA and one in Livingston, LA. IceCube is a neutrino observatory made up of one cubic kilometer of instrumented ice at the South Pole. With current limits for the IceCube array it is not expected that it will be able to detect neutrinos from sources in the Cygnus region soon [140], but the continued operation and proposed upgrade of IceCube could result in the detection of Galactic sources in neutrinos in the near future. Neutrino emission would give a signal of hadron acceleration in the astrophysical source. The first observations of gravitational waves by LIGO [141], have opened the door to future gravitational wave studies. Neutron star binaries in the Cygnus region could be promising targets for sensitive gravitational wave studies.

The VERITAS Cygnus survey reanalysis has confirmed the four previously detected sources in the region and has set limits on a large number of sources of interest in the region. A complete *Fermi*-LAT analysis has also been undertaken in order to study those sources at lower energies and find new HE sources. Off-pulse emission was found at the location of TeV J2032+4130 in the *Fermi*-LAT analysis which strengthens the PWN interpretation of the source. VHE emission stronger than expected from a pure PWN hints at contributions to the emission from the pulsar's binary interactions. The work presented here confirms the HE-VHE connection of the γ-Cygni SNR and its likely role as a local cosmic-ray proton acceleration source. The *Fermi*-LAT source associated with VER J2016+371 (CTB 87) has been determined to have two components with different spectral parameters. The Cisne region remains a mysterious region of active TeV emission from a large source. Because of its extent there is considerable source conclusion, but it is also likely to be a Galactic source. Furthermore many new HE sources have been identified in the *Fermi*-LAT data and will be further studied for their connections to potential cosmic-ray acceleration sources. Studies of Galactic gamma rays allow us to probe sources of extreme particle acceleration in our universe and resolve the mystery of cosmic-ray production.

APPENDIX A

Analysis Exclusion Regions

Table A.1 defines the exclusion regions for the measured VHE sources. The excluded stars list is presented in Table A.2. Figure A.1 maps these exclusion regions over the Cygnus region.

Table A.1: VERITAS previously detected source shapes used to define exclusion regions in the analysis of the Cygnus region.

Name	RA (deg)	dec (deg)	Extent (deg)	Orientation (rotation E–>N, deg.)
VER J2019+407 (γ-Cygni SNR)	304.92°	40.7°	0.5°x 0.4°	52°
TeV J2032+4130	307.85°	41.58°	0.62°x 0.38°	115°
VER J2016+371 (CTB 87)	303.98 °	37.2°	0.3°	
VER J2019+378 (Cisne)	304.86°	36.75°	0.65°x 0.4°	19°

Table A.2: List of bright stars used as exclusion regions for the VERITAS analysis of the Cygnus region.

RA (J2000) deg	dec (J2000) deg	HIP mag	Vmag	B-V mag
294.844	30.1533	96683	4.68	0.971
295.686	32.4267	96977	5.93	0.118
296.069	37.3544	97118	4.89	0.948
296.607	33.7276	97295	5	0.476
296.866	38.4076	97376	5.83	-0.087
297.642	38.7224	97630	5.18	1.665
298.701	36.9957	97985	5.79	0.773
298.966	38.4867	98068	4.95	-0.086
299.077	35.0834	98110	3.89	1.019
299.308	40.3678	98194	5.46	-0.09
299.658	30.9837	98325	5.51	-0.06
299.98	37.0429	98425	5.15	-0.133
300.275	27.7536	98543	4.66	0.184
300.906	29.8968	98767	5.73	0.749
301.151	32.2186	98863	5.62	0.76
301.591	35.9725	99031	5.38	0.85
302.357	36.8396	99303	4.93	-0.139
303.561	28.6948	99738	5.19	0.191
303.633	36.8063	99770	4.93	0.151
303.849	33.7291	99841	5.7	0.926
304.23	40.3651	99968	5.27	1.65
304.447	38.0329	100044	4.77	0.377
304.529	40.7321	100069	5.83	0.073
304.619	36.9998	100108	5.58	0.056
304.663	34.9828	100122	5.14	0.66
305.522	45.795	100437	5.58	1.077
305.557	40.2567	100453	2.23	0.673
305.689	41.026	100501	5.95	1.632
305.935	37.4764	100574	5.87	-0.173
305.965	32.1902	100587	4.43	1.331
306.893	38.4403	100907	5.63	0.072
307.335	36.4547	101067	5.9	0.407
308.476	35.2509	101474	4.61	1.593
310.013	43.4589	101986	5.97	1.186
310.358	45.2803	102098	1.25	0.092
310.485	41.7169	102155	5.68	-0.107
312.521	44.0593	102843	5.06	0.198
314.293	41.1671	103413	3.94	0.027

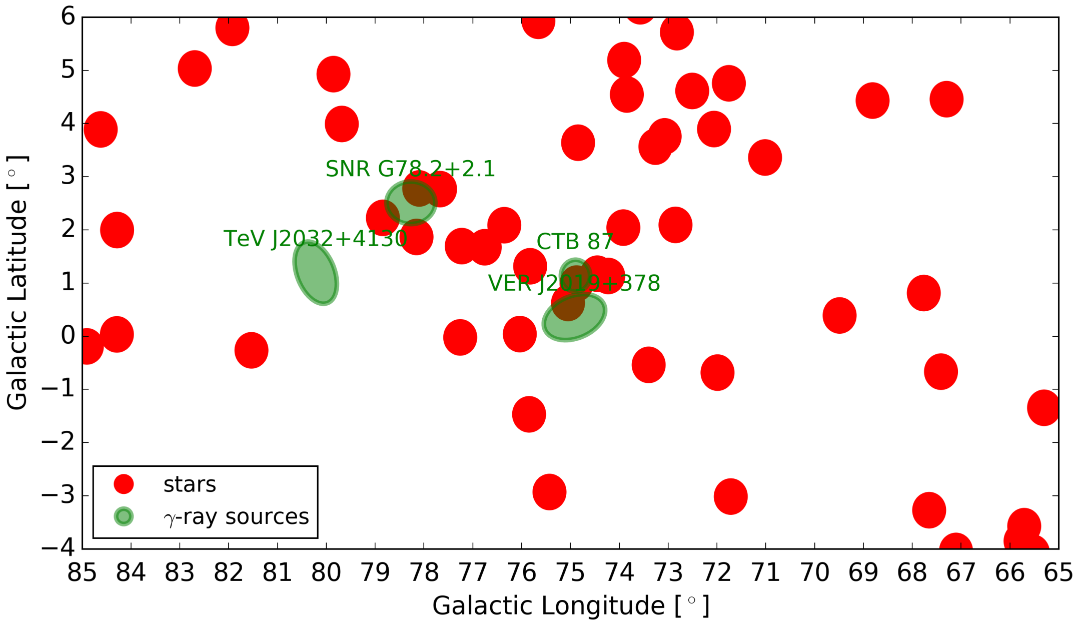

Figure A.1: The exclusion regions defined for the VERITAS analysis of the Cygnus region.

APPENDIX B

Fermi-LAT Analysis Details

The details of the *Fermi*-LAT data selection are presented in Table B.1.

Table B.1: Criteria for selecting *Fermi*-LAT photons for the analysis.

Start time	2008-08-04 15:43:37
End time	
Energy range (GeV)	1 to 500
Region Center (l,b)	74.5°,1.5°
Data Radius	30°
Data Type	Pass 8
IRF	P8R2_SOURCE_V6
Event class	128
Event type	2
Zenith angle	90°
Quality Cuts	(DATA_QUAL>0)&&(LAT_CONFIG==1)
Bin Size	0.1°

Sources with a TS $<$ 25 were removed from the *Fermi*-LAT analysis model, and then the region was refit. See Table B.2

The *Fermi*-LAT analysis also identified new sources outside the region of interest defined by the Cygnus region survey. Table B.3

Table B.2: List of sources removed from *Fermi*-LAT for TS< 25

3FGL J1848.9+4247
3FGL J1922.2+2313
3FGL J2107.1+2248
3FGL J2133.6+2821
3FGL J1838.1+3827
3FGL J2144.2+3132
3FGL J2104.7+2113
3FGL J2059.9+2029
3FGL J2147.2+4730c
3FGL J2131.5+2605
3FGL J2114.9+5448
3FGL J2014.9+1623
3FGL J1857.9+5549
3FGL J2209.0+3652
3FGL J2026.3+1430
3FGL J2055.6+1609
3FGL J1934.2+6002
3FGL J1829.2+2731
3FGL J1927.7+6118
3FGL J2031.8+1223
3FGL J1813.6+3143
3FGL J2039.7+1237
3FGL J1926.8+6154
3FGL J2034.3+1155
3FGL J1813.6+2820
3FGL J2035.3+1055
3FGL J1809.7+2909
3FGL J2033.3+4348c
3FGL J2102.3+4547
3FGL J1836.3+3137
3FGL J2011.1+4203
3FGL J2043.1+4350
3FGL J2058.3+3729
3FGL J2026.4+4709
3FGL J2110.3+3540
3FGL J2116.2+4422
3FGL J2014.5+5246
3FGL J2106.1+2505
3FGL J2139.5+3919
3FGL J2108.1+5202
3FGL J2114.0+5239
3FGL J2140.0+4715
3FGL J1852.4+4856
3FGL J2151.6+4154
3FGL J1849.5+2751
3FGL J1841.2+2910
3FGL J2202.7+4217
3FGL J2043.2+1711
3FGL J1842.2+2742
3FGL J1903.2+5541
3FGL J2157.5+3126
3FGL J1829.2+3229

Table B.3: List of new point sources found in the *Fermi*-LAT analysis, but that are outside the Cygnus region and were therefore not studied in detail

PS J1848.6+3248
PS J1910.9+4116
PS J1933.8+2550
PS J1938.0+2446
PS J1941.4+2559
PS J1941.9+2451
PS J1942.2+4012
PS J1943.7+2502
PS J1945.2+2610
PS J1946.5+2349
PS J1946.5+2434
PS J1947.4+2507
PS J1947.7+2743
PS J1950.8+2525
PS J1951.7+2624
PS J1954.6+2420
PS J1955.3+5132
PS J2003.9+2517
PS J2007.9+2511
PS J2011.6+2758
PS J2015.7+2828
PS J2016.2+4953
PS J2018.5+2935
PS J2019.8+2301
PS J2020.5+2430
PS J2021.3+2702
PS J2024.0+2048
PS J2024.3+3203
PS J2030.6+2234
PS J2031.5+3137
PS J2039.1+3210
PS J2039.3+2145
PS J2043.9+2050
PS J2045.4+5006
PS J2048.8+3118
PS J2049.8+3202
PS J2051.6+5049
PS J2056.5+3143
PS J2058.3+3339
PS J2101.6+3842
PS J2102.3+4702
PS J2109.8+3954
PS J2115.9+3702
PS J2142.5+3700

APPENDIX C

Fermi-LAT Pulsar Analysis Plots

Pulsar phaseograms made using the timing solutions from [123][1] using tempo2 [122]. MET stands for mission elapsed time for the *Fermi*-LAT satellite. Also plotted is the H-Test test significance (TS) as a function of time. This was developed to asses if the time series is periodic with a specified period [142].

C.1 PSR J1952.9+3253

Pulsar position:

RA: 19:52:58.206 (298.2425°), dec: 32:52:40.5 (32.8779°)

Time range for phase analysis:

START: 54686.1595856 (239860190 MET), FINISH: 56583.1570129 (403760768 MET)

Off-pulse phase: [0,0.1][0.3,0.5][0.7,1]

C.2 PSR J2021.1+3651

Pulsar position:

RA: 20:21:05.43 (305.2426°), dec: 36:57:04.63 (36.9513°)

Time range for phase analysis:

START: 54686.1596215 (239860193 MET), FINISH: 56583.1578036 (403760837 MET)

Off-pulse phase:[0.7,1] Bridge-pulse phase (part of on-pulse): [0.2,0.4]

---

[1] available at: http://www.slac.stanford.edu/ kerrm/fermi_pulsar_timing/

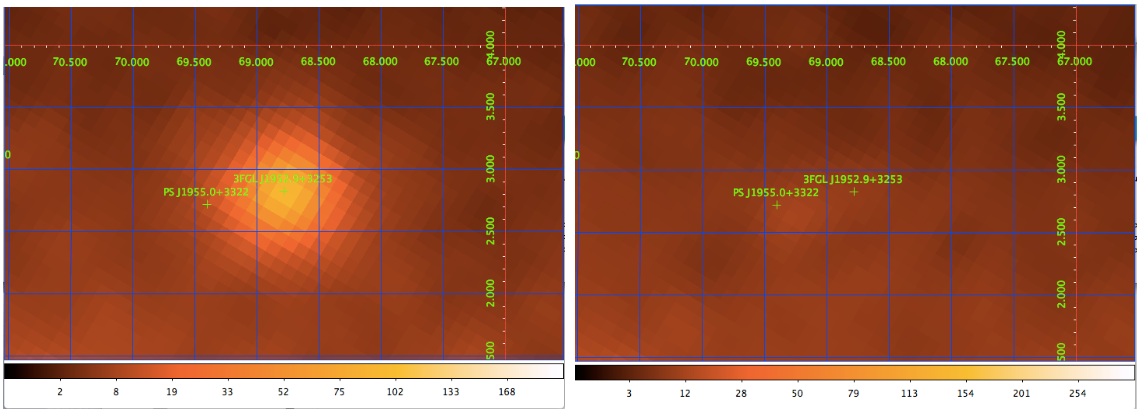

(a) ON (b) OFF

Figure C.1: Zoomed in counts map of PSR 1952+3253 region (square root scale, smoothed by 3 pixels). On the left is the counts in the on phase and on the right is the counts in the off phase.

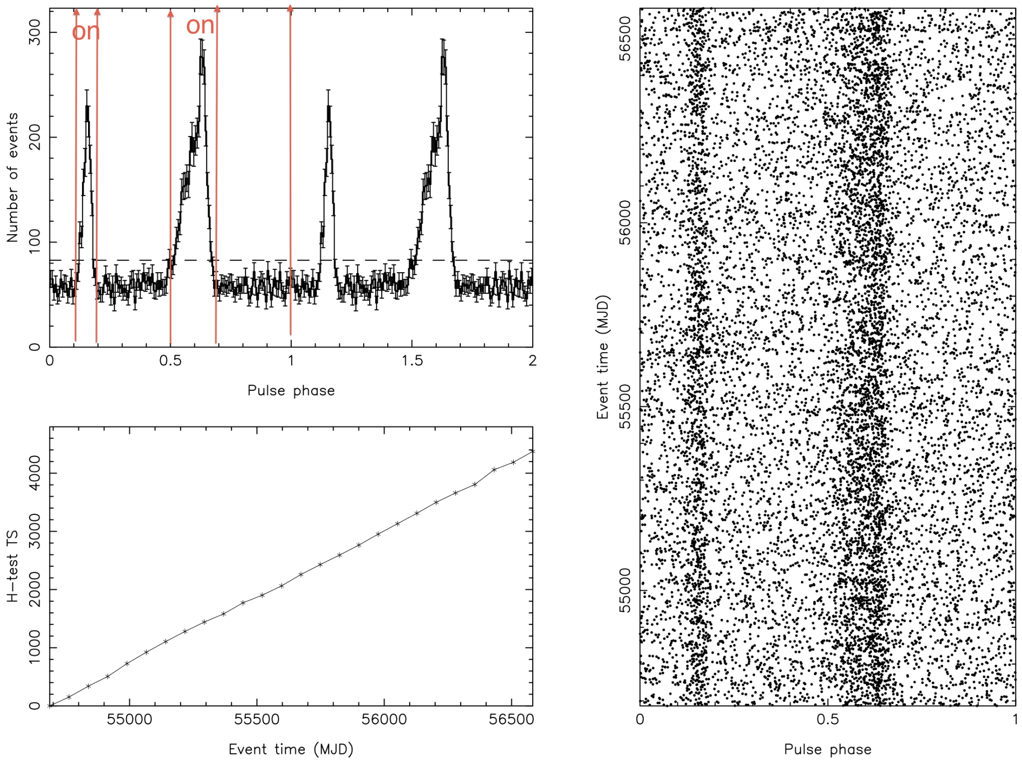

Figure C.2: Tempo2 phase outputs for PSR J1952.9+3253. The top left shows the number of events per phase, the bottom left shows the significance growing with observation time, and the right shows the phased events.

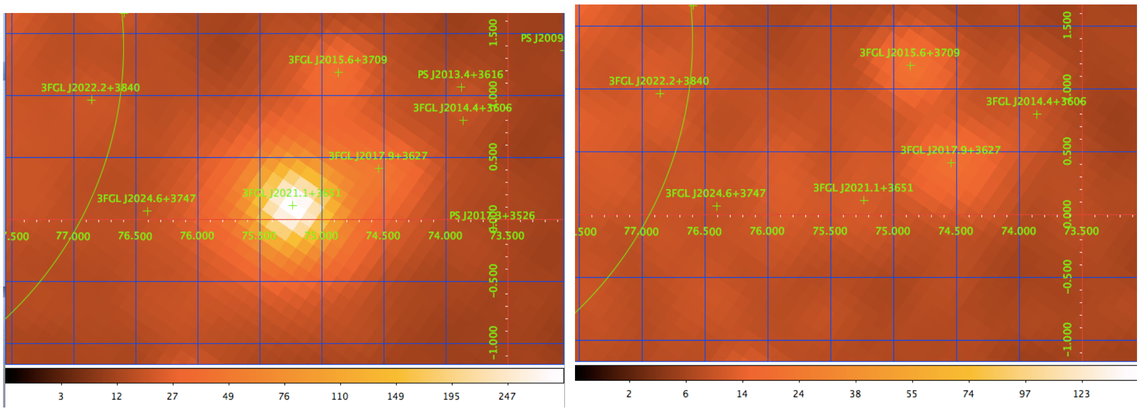

(a) ON

(b) OFF

Figure C.3: Zoomed in counts map of PSR J2021.1+3651 region (square root scale, smoothed by 3 pixels). On the left is the counts in the on phase and on the right is the counts in the off phase.

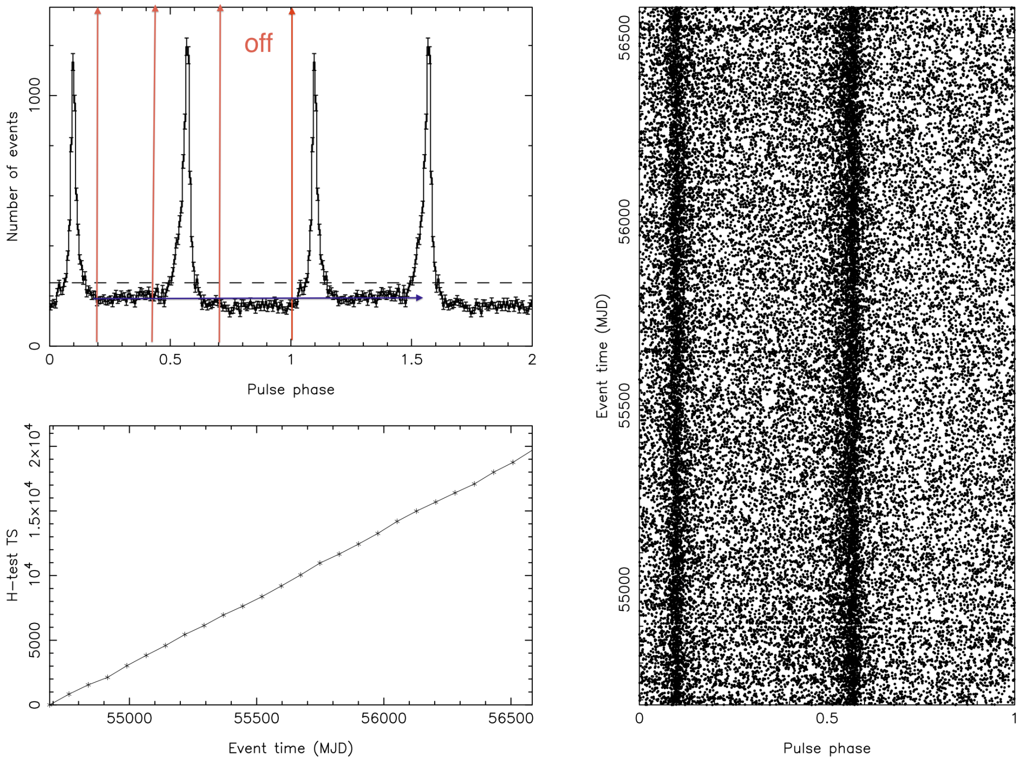

Figure C.4: Tempo2 phase outputs for PSR J2021.1+3651. The top left shows the number of events per phase, the bottom left shows the significance growing with observation time, and the right shows the phased events.

C.3 PSR J2021.5+4026

Pulsar near the γ-Cygni SNR

Pulsar position:

RA: 20:21:30.733 (305.378°), dec: 40:26:42.04 (40.445°)

Time range for phase analysis:

START: 54686.1591735 (240162554MET), FINISH: 56579.6577627 (403458433 MET)

Off-pulse phase: [0.16,0.36]

Due to the large flux variations in the source, an off-pulse analysis was not undertaken for PSR J2021.5+4026.

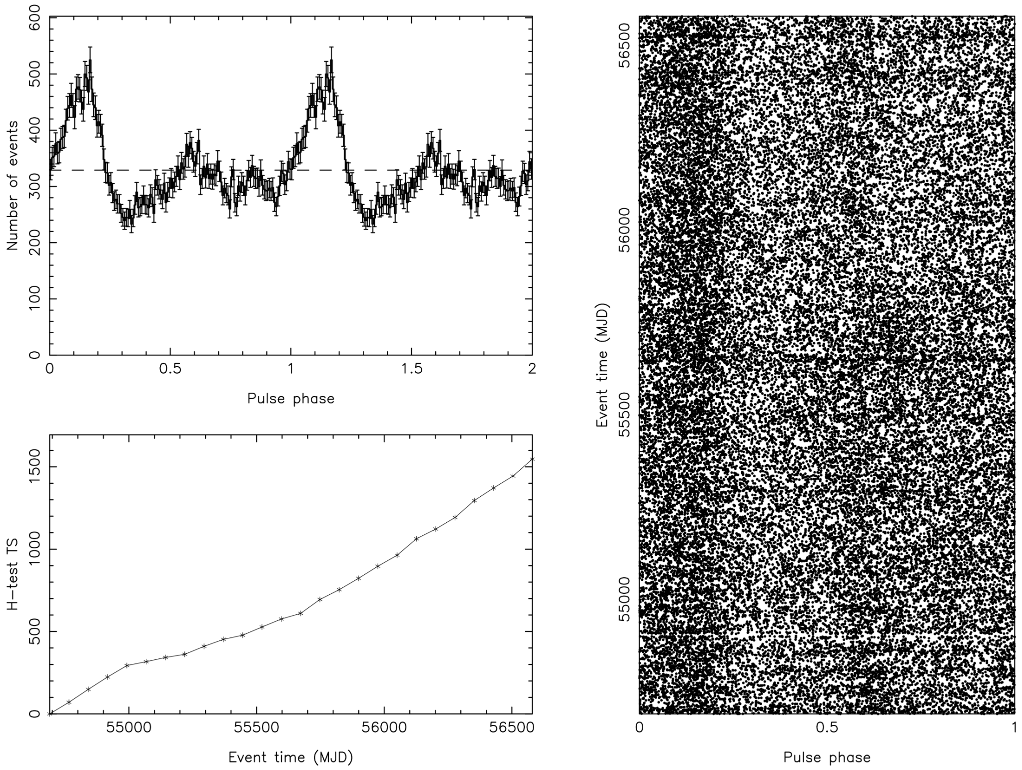

Figure C.5: Tempo2 phase outputs for PSR J2021.5+4026. The top left shows the number of events per phase, the bottom left shows the significance growing with observation time, and the right shows the phased events.

C.4 PSR J2032.2+4126

Pulsar position:

RA: 20:32:13.143 (308.055°), dec: 41:27:24.54 (41.457°)

Time range for phase analysis:

START: 54686.1591065 (239860148 MET), FINISH: 56583.1477928 (403759972 MET)

Off-pulse phase: [0.1,0.4][0.5,0.9]

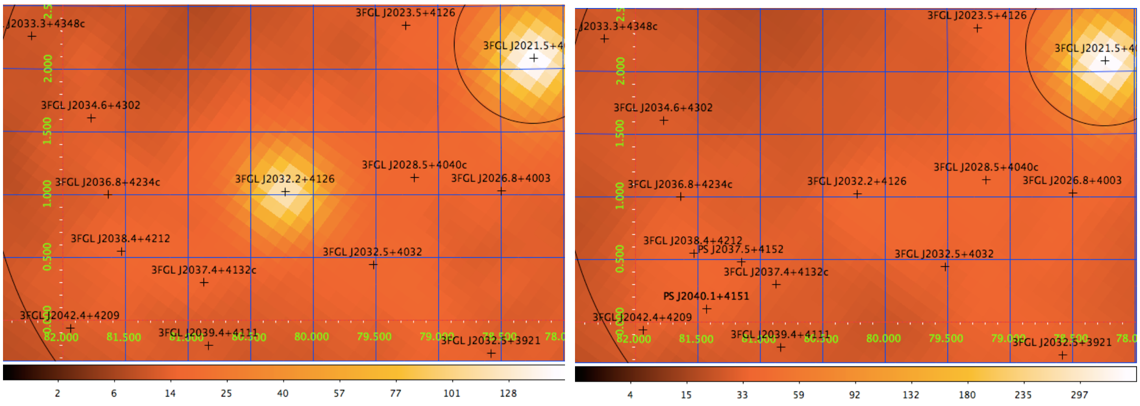

(a) ON

(b) OFF

Figure C.6: Zoomed in counts map of PSR J2032.2+4126 region (square root scale, smoothed by 3 pixels). On the left is the counts in the on phase and on the right is the counts in the off phase.

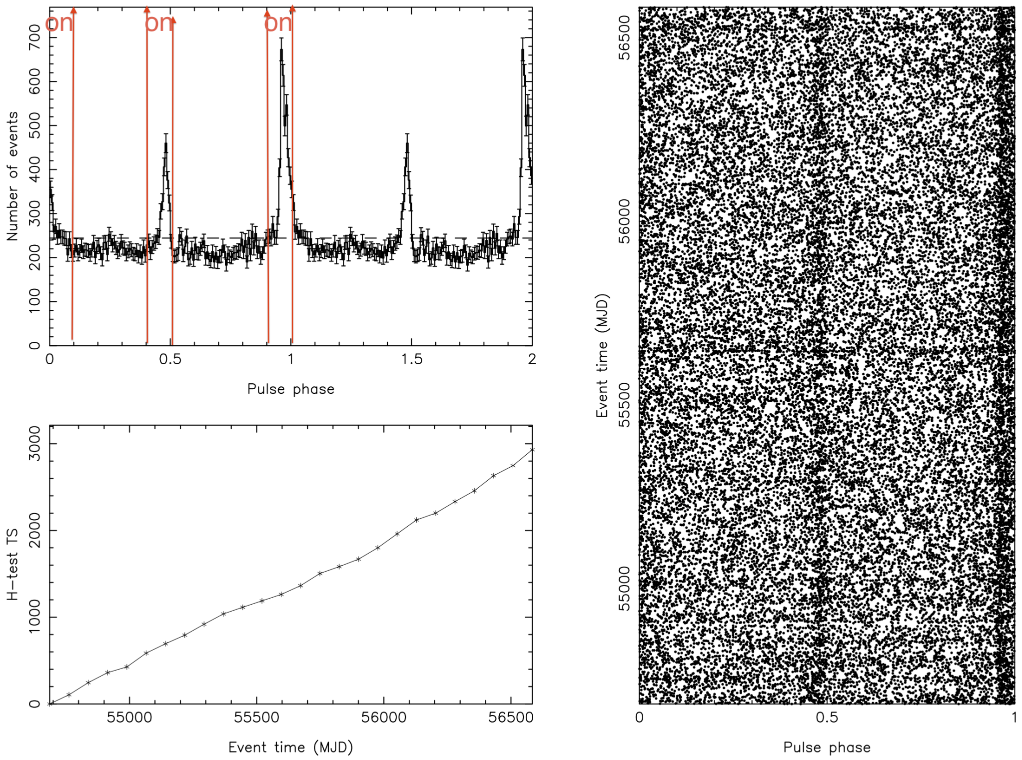

Figure C.7: Tempo2 phase outputs for PSR J2032.2+4126. The top left shows the number of events per phase, the bottom left shows the significance growing with observation time, and the right shows the phased events.

Bibliography

1. F. Hess, V. Über Beobachtungen der durchdringenden Strahlung bei sieben Freiballonfahrten. *Physikalische Zeitschrift* **13,** 1084–1091 (Nov. 1912).
2. Cronin, J. W., Gaisser, T. K. & Swordy, S. P. Cosmic Rays at the Energy Frontier. *Scientific American* **276,** 44–49. ISSN: 0036-8733 (Jan. 1997).
3. The Fermi-LAT Collaboration *et al.* Detection of the Characteristic Pion-Decay Signature in Supernova Remnants. *Science* **339,** 807–811. ISSN: 0036-8075, 1095-9203 (Feb. 2013).
4. Longair, M. S. *High Energy Astrophysics* <`http://adsabs.harvard.edu/abs/2011hea..book.....L`> (Feb. 2011).
5. Schmidt, F. *CORSIKA Shower Images* <`http://www.ast.leeds.ac.uk/~fs/showerimages.html`>.
6. Heck, D., Knapp, J., Capdevielle, J. N., Schatz, G. & Thouw, T. *CORSIKA: a Monte Carlo code to simulate extensive air showers.* <`http://adsabs.harvard.edu/abs/1998cmcc.book.....H`> (Feb. 1998).
7. Bennett, K. COS-B: The highlights. *Nuclear Physics B Proceedings Supplements* **14,** 23–34. ISSN: 0920-5632 (Apr. 1990).
8. Hartman, R. C. *et al.* The Third EGRET Catalog of High-Energy Gamma-Ray Sources. *The Astrophysical Journal Supplement Series* **123,** 79–202. ISSN: 0067-0049 (July 1999).
9. Atwood, W. B. *et al.* The Large Area Telescope on the Fermi Gamma-Ray Space Telescope Mission. *The Astrophysical Journal* **697,** 1071. ISSN: 0004-637X (2009).
10. Kohnle, A. *et al.* Stereoscopic imaging of air showers with the first two HEGRA Cherenkov telescopes. *Astroparticle Physics* **5,** 119–131. ISSN: 0927-6505 (Aug. 1996).

11. Weekes, T. C. *et al.* Observation of TeV gamma rays from the Crab nebula using the atmospheric Cerenkov imaging technique. *The Astrophysical Journal* **342,** 379–395. ISSN: 0004-637X (July 1989).

12. Holder, J. *et al.* VERITAS: Status and Highlights. *arXiv:1111.1225 [astro-ph].* <`http://arxiv.org/abs/1111.1225`> (Nov. 2011).

13. Albert, J. *et al.* VHE γ-Ray Observation of the Crab Nebula and its Pulsar with the MAGIC Telescope. *The Astrophysical Journal* **674,** 1037–1055. ISSN: 0004-637X (Feb. 2008).

14. Hinton, J. A. & the HESS Collaboration. The status of the HESS project. *New Astronomy Reviews* **48,** 331–337. ISSN: 1387-6473 (Apr. 2004).

15. *Welcome to TeVCat, an Online Gamma-Ray Catalog!* <`http://tevcat.uchicago.edu/`>.

16. Acharya, B. S. *et al.* Introducing the CTA concept. *Astroparticle Physics. Seeing the High-Energy Universe with the Cherenkov Telescope Array - The Science Explored with the CTA* **43,** 3–18. ISSN: 0927-6505 (Mar. 2013).

17. ARGO-YBJ Collaboration *et al.* Results from the ARGO-YBJ test experiment. *Astroparticle Physics* **17,** 151–165. ISSN: 0927-6505 (May 2002).

18. Atkins, R. *et al.* TeV Gamma-Ray Survey of the Northern Hemisphere Sky Using the Milagro Observatory. *The Astrophysical Journal* **608,** 680. ISSN: 0004-637X (2004).

19. Westerhoff, S. HAWC: A next-generation all-sky gamma-ray telescope. *Advances in Space Research. Cosmic Ray Origins: Viktor Hess Centennial Anniversary* **53,** 1492–1498. ISSN: 0273-1177 (May 2014).

20. Greisen, K. End to the Cosmic-Ray Spectrum? *Phys. Rev. Lett.* **16,** 748–750 (Apr. 1966).

21. Olive, K. A. *et al.* Review of Particle Physics. *Chin. Phys.* **C38,** 090001 (2014).

22. Lund, N. Cosmic-ray elemental abundances. *Advances in Space Research* **4,** 5–14. ISSN: 0273-1177 (1984).

23. Fermi, E. On the Origin of the Cosmic Radiation. *Phys. Rev.* **75,** 1169–1174 (Apr. 1949).

24. Bell, A. R. The acceleration of cosmic rays in shock fronts. I. *Monthly Notices of the Royal Astronomical Society* **182,** 147–156. ISSN: 0035-8711 (Jan. 1978).

25. Ellison, D. C., Patnaude, D. J., Slane, P., Blasi, P. & Gabici, S. Particle Acceleration in Supernova Remnants and the Production of Thermal and Nonthermal Radiation. *The Astrophysical Journal* **661.** arXiv: astro-ph/0702674, 879–891. ISSN: 0004-637X, 1538-4357 (June 2007).

26. Jackson, J. D. *Classical Electrodynamics Third Edition* ISBN: 978-0-471-30932-1 (Wiley, New York, Aug. 1998).

27. Acciari, V. A. *et al.* Discovery of TeV Gamma-ray Emission from Tycho's Supernova Remnant. *The Astrophysical Journal* **730,** L20. ISSN: 2041-8205 (2011).

28. Kennel, C. F. & Coroniti, F. V. Magnetohydrodynamic model of Crab nebula radiation. *The Astrophysical Journal* **283,** 710–730. ISSN: 0004-637X (Aug. 1984).

29. De Jager, O. C. & Harding, A. K. The expected high-energy to ultra-high-energy gamma-ray spectrum of the Crab Nebula. *The Astrophysical Journal* **396,** 161–172 (Sept. 1992).

30. Piddington, J. H. & Minnett, H. C. Radio-Frequency Radiation from the Constellation of Cygnus. *Australian Journal of Scientific Research A Physical Sciences* **5,** 17 (Mar. 1952).

31. Higgs, L. A. 10-GHz survey of the Cygnus X region. *The Astronomical Journal* **82,** 329–336. ISSN: 0004-6256 (May 1977).

32. Weiler, K. W. & Shaver, P. A. Total Intensity and Polarization Structure of the Supernova Remnant G 74.9 + 1.2 at XX6,21, and 49 Centimeters. *Astronomy and Astrophysics* **70,** 389. ISSN: 0004-6361 (Nov. 1978).

33. Cash, W. *et al.* The X-ray superbubble in Cygnus. *The Astrophysical Journal Letters* **238,** L71–L76. ISSN: 0004-637X (June 1980).

34. Higgs, L. A., Landecker, T. L. & Seward, F. D. *The X-ray structure of the supernova remnant G78.2 + 2.1* in. **101** (1983), 281–286. <`http://adsabs.harvard.edu/abs/1983IAUS..101..281H`>.

35. Bochkarev, N. G. & Sitnik, T. G. Structure and origin of the Cygnus superbubble. *Astrophysics and Space Science* **108,** 237–302. ISSN: 0004-640X (Jan. 1985).

36. Uchiyama, Y., Takahashi, T., Aharonian, F. & Mattox, J. ASCA View of the Supernova Remnant Gamma Cygni (G78.2+2.1): Bremsstrahlung X-ray Spectrum from Loss-flattened Electron Distribution. *The Astrophysical Journal* **571,** 866–875. ISSN: 0004-637X, 1538-4357 (June 2002).

37. Mavromatakis, F. Deep optical observations of the supernova remnant G 78.2+2.1. *Astronomy and Astrophysics* **408,** 237–243. ISSN: 0004-6361 (Sept. 2003).

38. Ladouceur, Y. & Pineault, S. New perspectives on the supernova remnant G78.2+2.1. *Astronomy and Astrophysics* **490,** 197–211. ISSN: 0004-6361 (Oct. 2008).

39. Matheson, H., Safi-Harb, S. & Kothes, R. X-Ray Observations of the Supernova Remnant CTB 87 (G74.9+1.2): An Evolved Pulsar Wind Nebula. *The Astrophysical Journal* **774,** 33. ISSN: 0004-637X (Sept. 2013).

40. Kothes, R., Reich, W., Foster, T. & Byun, D.-Y. The Distance to the Supernova Remnant CTB 87 and the Radial Velocity of the Perseus Arm toward l=75°, Derived from H I and CO Observations. *The Astrophysical Journal* **588,** 852–861. ISSN: 0004-637X (May 2003).

41. Green, D. A. A catalogue of 294 Galactic supernova remnants. *Bulletin of the Astronomical Society of India* **42,** 47–58. ISSN: 0304-9523 (June 2014).

42. Green, D. A. A revised Galactic supernova remnant catalogue. *Bulletin of the Astronomical Society of India* **37,** 45–61. ISSN: 0304-9523 (Mar. 2009).

43. Green, D. A. Galactic supernova remnants: an updated catalogue and some statistics. *Bulletin of the Astronomical Society of India* **32,** 335–370. ISSN: 0304-9523 (Dec. 2004).

44. Leahy, D. A. & Ranasinghe, S. Radio observations of CTB80: detection of the snowplough in an old supernova remnant. *Monthly Notices of the Royal Astronomical Society* **423,** 718–724. ISSN: 0035-8711 (June 2012).

45. Zdziarski, A. A. *et al.* The high-energy gamma-ray detection of G73.9+0.9, a supernova remnant interacting with a molecular cloud. *Monthly Notices of the Royal Astronomical Society* **455,** 1451–1458. ISSN: 0035-8711 (Jan. 2016).

46. Ferrand, G. & Safi-Harb, S. A Census of High-Energy Observations of Galactic Supernova Remnants. *Advances in Space Research* **49,** 1313–1319. ISSN: 02731177 (May 2012).

47. Arzoumanian, Z. *et al.* Discovery of an Energetic Pulsar Associated with SNR G76.9+1.0. *The Astrophysical Journal* **739,** 39. ISSN: 0004-637X (Sept. 2011).

48. Van Etten, A., Romani, R. W. & Ng, C.-Y. Rings and Jets around PSR J2021+3651: The "Dragonfly Nebula". *The Astrophysical Journal* **680,** 1417–1425. ISSN: 0004-637X (June 2008).

49. Manchester, R. N., Hobbs, G. B., Teoh, A. & Hobbs, M. The Australia Telescope National Facility Pulsar Catalogue. *The Astronomical Journal* **129,** 1993. ISSN: 1538-3881 (2005).

50. Liu, Q. Z., Paradijs, J. v. & Heuvel, E. P. J. v. d. Catalogue of high-mass X-ray binaries in the Galaxy (4th edition). *Astronomy and Astrophysics* **455,** 4 (2006).

51. Liu, Q. Z., van Paradijs, J. & van den Heuvel, E. P. J. A catalogue of low-mass X-ray binaries in the Galaxy, LMC, and SMC (Fourth edition). *Astronomy and Astrophysics* **469,** 807–810. ISSN: 0004-6361 (July 2007).

52. Albert, J. *et al.* Very High Energy Gamma-Ray Radiation from the Stellar Mass Black Hole Binary Cygnus X-1. *The Astrophysical Journal* **665,** L51. ISSN: 1538-4357 (2007).

53. Archambault, S. *et al.* VERITAS Observations of the Microquasar Cygnus X-3. *The Astrophysical Journal* **779,** 150. ISSN: 0004-637X (2013).

54. Lamb, R. C. & Macomb, D. J. Point Sources of GeV Gamma Rays. *The Astrophysical Journal* **488,** 872. ISSN: 0004-637X (1997).

55. Hunter, S. D. *et al.* EGRET Observations of the Diffuse Gamma-Ray Emission from the Galactic Plane. *The Astrophysical Journal* **481,** 205–240 (May 1997).

56. Brazier, K. T. S., Kanbach, G., Carramiñana, A., Guichard, J. & Merck, M. The nature of the γ-ray source 2EG J2020+4026 (2CG 078+2). *Monthly Notices of the Royal Astronomical Society* **281,** 1033–1037. ISSN: 0035-8711 (Aug. 1996).

57. The Fermi-LAT Collaboration. Fermi Large Area Telescope First Source Catalog. *arXiv:1002.2280v1.* <`http://arxiv.org/abs/1002.2280v1`> (Feb. 2010).

58. The Fermi-LAT Collaboration. Fermi Large Area Telescope Second Source Catalog. *arXiv:1108.1435v1.* <`http://arxiv.org/abs/1108.1435v1`> (Aug. 2011).

59. The Fermi-LAT Collaboration. Fermi Large Area Telescope Third Source Catalog. *arXiv:1501.02003 [astro-ph].* <`http://arxiv.org/abs/1501.02003`> (Jan. 2015).

60. The Fermi-LAT Collaboration. The First Fermi-LAT Catalog of Sources Above 10 GeV. *arXiv:1306.6772v1.* <`http://arxiv.org/abs/1306.6772v1`> (June 2013).

61. The Fermi-LAT Collaboration. 2FHL: The Second Catalog of Hard Fermi-LAT Sources. *arXiv:1508.04449 [astro-ph].* <`http://arxiv.org/abs/1508.04449`> (Aug. 2015).

62. The Fermi-LAT Collaboration. PSR J2021+4026 in the Gamma Cygni region: the first variable gamma-ray pulsar seen by the Fermi LAT. *The Astrophysical Journal* **777,** L2. ISSN: 2041-8205, 2041-8213 (Nov. 2013).

63. Abdo, A. A. *et al.* Detection of 16 Gamma-Ray Pulsars Through Blind Frequency Searches Using the Fermi LAT. *Science* **325,** 840–844. ISSN: 0036-8075, 1095-9203 (Aug. 2009).

64. Camilo, F. *et al.* Radio Detection of LAT PSRs J1741-2054 and J2032+4127: No Longer Just Gamma-Ray Pulsars. *The Astrophysical Journal* **705,** 1–13 (Oct. 2009).

65. Lyne, A. *et al.* The Binary Nature of PSR J2032+4127. *arXiv:1502.01465 [astro-ph].* <`http://arxiv.org/abs/1502.01465`> (Feb. 2015).

66. Abdo, A. A. *et al.* Fermi Large Area Telescope Observations of Gamma-ray Pulsars PSR J1057-5226, J1709-4429, and J1952+3252. *The Astrophysical Journal* **720,** 26. ISSN: 0004-637X (2010).

67. The Fermi-LAT Collaboration. Modulated High-Energy Gamma-Ray Emission from the Microquasar Cygnus X-3. *Science* **326,** 1512–1516. ISSN: 0036-8075, 1095-9203 (Dec. 2009).

68. Ackermann, M. *et al.* A Cocoon of Freshly Accelerated Cosmic Rays Detected by Fermi in the Cygnus Superbubble. *Science* **334,** 1103–1107. ISSN: 0036-8075, 1095-9203 (Nov. 2011).

69. Mizuno, T. *et al.* Suzaku Observation of the Fermi Cygnus Cocoon: The Search for a Signature of Young Cosmic-Ray Electrons. *The Astrophysical Journal* **803,** 74. ISSN: 0004-637X (Apr. 2015).

70. Aharonian, F. *et al.* An unidentified TeV source in the vicinity of Cygnus OB2. *Astronomy and Astrophysics* **393,** L37–L40 (Oct. 2002).

71. Aharonian, F. *et al.* The unidentified TeV source (TeV J2032+4130) and surrounding field: Final HEGRA IACT-System results. *Astronomy and Astrophysics* **431,** 197–202 (Feb. 2005).

72. Lang, M. J. *et al.* Evidence for TeV gamma ray emission from TeV J2032+4130 in Whipple archival data. *Astronomy and Astrophysics* **423,** 415–419 (Aug. 2004).

73. Lang, M. J. *et al.* A new TeV source confirmed in Whipple archival data: TeV J2032+41. *Astrophysics and Space Science* **297,** 345–351 (Jan. 2005).

74. Butt, Y. M. *et al.* Chandra/Very Large Array Follow-Up of TeV J2032+4131, the Only Unidentified TeV Gamma-Ray Source. *The Astrophysical Journal* **597,** 494–512 (2003).

75. Knödlseder, J. Cygnus OB2 - a young globular cluster in the Milky Way. *Astronomy and Astrophysics* **360,** 539–548. ISSN: 0004-6361 (Aug. 2000).

76. Butt, Y. M., Schneider, N., Dame, T. M. & Brunt, C. The Molecular Environment of the Gamma-Ray Source TeV J2032+4130. *The Astrophysical Journal Letters* **676,** L123. ISSN: 0004-637X (Apr. 2008).

77. Abdo, A. A. *et al.* Discovery of TeV Gamma-Ray Emission from the Cygnus Region of the Galaxy. *The Astrophysical Journal Letters* **658,** L33–L36. ISSN: 0004-637X (Mar. 2007).

78. Study on TeV gammaRay Emission from Cygnus Region Using the Tibet Air Shower Array. <`http://indico.nucleares.unam.mx/getFile.py/access?contribId=548&sessionId=103&resId=0&materialId=paper&confId=4`> (2007).

79. Abdo, A. A. *et al.* TeV Gamma-Ray Sources from a Survey of the Galactic Plane with Milagro. *arXiv:0705.0707v1.* doi:`10.1086/520717`. <`http://arxiv.org/abs/0705.0707v1`> (May 2007).

80. Abdo, A. A. *et al.* Spectrum and Morphology of the Two Brightest Milagro Sources in the Cygnus Region: MGRO J2019+37 and MGRO J2031+41. *The Astrophysical Journal* **753,** 159. ISSN: 0004-637X (July 2012).

81. Abdo, A. A. *et al.* Milagro Observations of Potential TeV Emitters. *arXiv:1403.0161v1.* <`http://arxiv.org/abs/1403.0161v1`> (Mar. 2014).

82. Strong, A. W. & Moskalenko, I. V. Models for galactic cosmic-ray propagation. *Advances in Space Research* **27,** 717–726. ISSN: 0273-1177 (2001).

83. Abdo, A. A. *et al.* A Measurement of the Spatial Distribution of Diffuse TeV Gamma Ray Emission from the Galactic Plane with Milagro. *arXiv:0805.0417v2.* doi:`10.1086/592213`. <`http://iopscience.iop.org/0004-637X/688/2/1078`> (May 2008).

84. Carrigan, S. *et al.* The H.E.S.S. Galactic Plane Survey - maps, source catalog and source population. *arXiv:1307.4690 [astro-ph].* <`http://arxiv.org/abs/1307.4690`> (July 2013).

85. Fernandez, D., Hahn, J., Marandon, V., Renaud, M. & for the H.E.S.S. Collaboration, A. V. Study of the Very High Energy emission from Supernova Remnants with H.E.S.S. *arXiv:1307.6347 [astro-ph].* <`http://arxiv.org/abs/1307.6347`> (July 2013).

86. Klepser, S. *et al.* A Population of Teraelectronvolt Pulsar Wind Nebulae in the H.E.S.S. Galactic Plane Survey. *arXiv:1307.7905 [astro-ph].* <`http://arxiv.org/abs/1307.7905`> (July 2013).

87. Egberts, K. *et al.* Diffuse TeV Gamma-Ray Emission in the H.E.S.S. Galactic Plane Survey. *arXiv:1308.0161 [astro-ph].* <`http://arxiv.org/abs/1308.0161`> (Aug. 2013).

88. The H.E.S.S. Collaboration. *The H.E.S.S. Source Catalog* 2016. <`https://www.mpi-hd.mpg.de/hfm/HESS/pages/home/sources/`>.

89. Rossi, B. & Greisen, K. Cosmic-Ray Theory. *Rev. Mod. Phys.* **13,** 240–309 (4 Oct. 1941).

90. Weekes, T. *Very High Energy Gamma-Ray Astronomy* in. **11** (Apr. 2003). doi:`10.1201/9781420033199`. <`http://adsabs.harvard.edu/abs/2003WSAA...11.....W`>.

91. Galbraith, W. & Jelley, J. V. Light Pulses from the Night Sky associated with Cosmic Rays. *Nature* **171,** 349–350. ISSN: 0028-0836 (Feb. 1953).

92. Weekes, T. C. The Atmospheric Cherenkov Technique in Very High Energy Gamma-Ray Astronomy. *Space Science Reviews* **75,** 1–15. ISSN: 0038-6308 (Jan. 1996).

93. Weekes, T. C. VERITAS: the Very Energetic Radiation Imaging Telescope Array System. *Astroparticle Physics* **17,** 221–243. ISSN: 09276505 (May 2002).

94. Holder, J. Atmospheric Cherenkov Gamma-ray Telescopes. *arXiv:1510.05675 [astro-ph].* <`http://arxiv.org/abs/1510.05675`> (Oct. 2015).

95. Hillas, A. M. *et al.* The Spectrum of TeV Gamma Rays from the Crab Nebula. *The Astrophysical Journal* **503,** 744. ISSN: 0004-637X (1998).

96. Hinton, J. A. & Hofmann, W. Teraelectronvolt Astronomy. *Annual Review of Astronomy and Astrophysics* **47,** 523–565. ISSN: 0066-4146, 1545-4282 (Sept. 2009).

97. Park, N. & for the VERITAS Collaboration. Performance of the VERITAS experiment. *arXiv:1508.07070 [astro-ph].* <`http://arxiv.org/abs/1508.07070`> (Aug. 2015).

98. Atwood, W. *et al.* Pass 8: Toward the Full Realization of the Fermi-LAT Scientific Potential. *arXiv:1303.3514 [astro-ph].* <`http://arxiv.org/abs/1303.3514`> (Mar. 2013).

99. Perkins, J. S., Maier, G. & The VERITAS Collaboration. VERITAS Telescope 1 Relocation: Details and Improvements. *arXiv:0912.3841 [astro-ph].* <`http://arxiv.org/abs/0912.3841`> (Dec. 2009).

100. D. B. Kieda for the VERITAS Collaboration. The Gamma Ray Detection sensitivity of the upgraded VERITAS Observatory. *arXiv:1308.4849* **1308.** <`http://adsabs.harvard.edu/abs/2013arXiv1308.4849D`> (Aug. 2013).

101. Davies, J. M. & Cotton, E. S. Design of the quartermaster solar furnace. *Solar Energy. The Proceedings of the Solar Furnace Symposium* **1,** 16–22. ISSN: 0038-092X (Apr. 1957).

102. Roache, E. *et al.* Mirror Facets for the VERITAS Telescopes. *International Cosmic Ray Conference* **3,** 1397–1400 (2008).

103. McCann, A., Hanna, D. & McCutcheon, M. An Alignment System for Imaging Atmospheric Cherenkov Telescopes. *arXiv:0907.4975* **0907.** <`http://adsabs.harvard.edu/abs/2009arXiv0907.4975M`> (July 2009).

104. Weinstein, A. & for the VERITAS Collaboration. The VERITAS Trigger System. *arXiv:0709.4438 [astro-ph].* <`http://arxiv.org/abs/0709.4438`> (Sept. 2007).

105. The VERITAS Collaboration and Hays, E. VERITAS Data Acquisition. *arXiv:0710.2288 [astro-ph].* <`http://arxiv.org/abs/0710.2288`> (Oct. 2007).

106. Park, N. for the VERITAS Collaboration. Highlights from VERITAS studies of TeV astroparticle physics. <`https://www.icrr.u-tokyo.ac.jp/indico/contributionDisplay.py?contribId=130&sessionId=7&confId=23`> (Oct. 2015).

107. Hanna, D., McCann, A., McCutcheon, M. & Nikkinen, L. An LED-based Flasher System for VERITAS. *Nuclear Instruments and Methods in Physics Research Section A: Accelerators, Spectrometers, Detectors and Associated Equipment* **612,** 278–287. ISSN: 01689002 (Jan. 2010).

108. Otte, A. N. & for the VERITAS Collaboration. The Upgrade of VERITAS with High Efficiency Photomultipliers. *arXiv:1110.4702 [astro-ph].* <`http://arxiv.org/abs/1110.4702`> (Oct. 2011).

109. Daniel, M. K. *The VERITAS standard data analysis* in *arXiv.org* (2008), 1325–1328. <`http://arxiv.org/abs/0709.4006`>.

110. Duke, C. & LeBohec, S. *GrISU* 2013. <`http://www.physics.utah.edu/gammaray/GrISU/`>.

111. Hillas, A. M. Cerenkov light images of EAS produced by primary gamma. *International Cosmic Ray Conference* **3,** 445–448 (Aug. 1985).

112. Fegan, D. J. Gamma/hadron separation at TeV energies. *Journal of Physics G: Nuclear and Particle Physics* **23,** 1013–1060 (Jan. 1999).

113. Hofmann, W. Comparison of techniques to reconstruct VHE gamma-ray showers from multiple stereoscopic Cherenkov images. *Astroparticle Physics* **12,** 135–143 (Nov. 1999).

114. Berge, D., Funk, S. & Hinton, J. Background modelling in very-high-energy γ-ray astronomy. *Astronomy and Astrophysics* **466,** 1219–1229. ISSN: 0004-6361 (May 2007).

115. Li, T.-P. & Ma, Y.-Q. Analysis methods for results in gamma-ray astronomy. *The Astrophysical Journal* **272,** 317–324. ISSN: 0004-637X (Sept. 1983).

116. Helene, O. Upper limit of peak area. *Nuclear Instruments and Methods in Physics Research* **212,** 319–322 (July 1983).

117. Rolke, W. A., López, A. M. & Conrad, J. Limits and confidence intervals in the presence of nuisance parameters. *Nuclear Instruments and Methods in Physics Research Section A: Accelerators, Spectrometers, Detectors and Associated Equipment* **551,** 493–503. ISSN: 0168-9002 (Oct. 2005).

118. Feldman, G. J. & Cousins, R. D. Unified approach to the classical statistical analysis of small signals. *Physical Review D* **57,** 3873–3889. ISSN: 0556-2821 (Apr. 1998).

119. The Fermi-LAT Collaboration. *Installing the Fermi Science Tools* 2016. <`http://fermi.gsfc.nasa.gov/ssc/data/analysis/software/`>.

120. Fermipy Developers. *Welcome to Fermipy's documentation!* 2016. <`http://fermipy.readthedocs.io/en/latest/`>.

121. Abdo, A. A. *et al.* Fermi/Large Area Telescope Bright Gamma-Ray Source List. *The Astrophysical Journal Supplement Series* **183,** 46–66. ISSN: 0067-0049 (July 2009).

122. Hobbs, G. B., Edwards, R. T. & Manchester, R. N. TEMPO2, a new pulsar-timing package - I. An overview. *Monthly Notices of the Royal Astronomical Society* **369,** 655–672. ISSN: 0035-8711 (June 2006).

123. Kerr, M., Ray, P., Johnston, S., Shannon, R. & Camilo, F. Timing Gamma-ray Pulsars with the Fermi Large Area Telescope: Timing Noise and Astrometry. *The Astrophysical Journal* **814,** 128. ISSN: 1538-4357 (Nov. 2015).

124. Aliu, E. *et al.* Discovery of TeV Gamma-Ray Emission toward Supernova Remnant SNR G78.2+2.1. *The Astrophysical Journal* **770,** 93. ISSN: 0004-637X (June 2013).

125. Aliu, E. *et al.* Observations of the Unidentified Gamma-Ray Source TeV J2032+4130 by VERITAS. *The Astrophysical Journal* **783,** 16. ISSN: 0004-637X (Mar. 2014).

126. Aliu, E. *et al.* Spatially Resolving the Very High Energy Emission from MGRO J2019+37 with VERITAS. *The Astrophysical Journal* **788,** 78. ISSN: 0004-637X (June 2014).

127. Aliu, E. *et al.* Investigating the TeV Morphology of MGRO J1908+06 with VERITAS. *The Astrophysical Journal* **787,** 166. ISSN: 0004-637X (2014).

128. Aharonian, F. & The HEGRA Collaboration. The Energy Spectrum of TeV Gamma-Rays from the Crab Nebula as measured by the HEGRA system of imaging air Cherenkov telescopes. *The Astrophysical Journal* **539,** 317–324. ISSN: 0004-637X, 1538-4357 (Aug. 2000).

129. Zanin, R. *et al.* Gamma rays detected from Cygnus X-1 with likely jet origin. *Astronomy and Astrophysics* **596,** A55. ISSN: 0004-6361 (Nov. 2016).

130. Acero, F. *et al.* The 1st Fermi Lat Supernova Remnant Catalog. *arXiv:1511.06778 [astro-ph].* <`http://arxiv.org/abs/1511.06778`> (Nov. 2015).

131. Albert, J. & for the MAGIC Collaboration. MAGIC observations of the unidentified TeV gamma-ray source TeV J2032+4130. *arXiv:0801.2391v2.* doi:`10.1086/529520`. <`http://arxiv.org/abs/0804.0410`> (Jan. 2008).

132. Taylor, A. R. *et al.* The Canadian Galactic Plane Survey. *Astronomical Journal* **125,** 3145–3164 (June 2003).

133. Fraija, N. & Araya, M. The GeV counterpart of VER J2019+407 in the northern shell of the supernova remnant G78.2+2.1 (γ Cygni). *arXiv:1605.00571 [astro-ph].* <`http://arxiv.org/abs/1605.00571`> (May 2016).

134. Clark, C. J. *Einstein@Home Gamma-ray Pulsar Discoveries in Fermi-LAT Data* 2016. <`https://einsteinathome.org/gammaraypulsar/FGRP1_discoveries.html`>.

135. Trepl, L. *et al.* Multiwavelength properties of a new Geminga-like pulsar: PSR J2021+4026. *Monthly Notices of the Royal Astronomical Society.* ISSN: 00358711, 13652966. doi:`10.1111/j.1365-2966.2010.16555.x`. <`http://arxiv.org/abs/1008.4313`> (Apr. 2010).

136. Landecker, T. L., Roger, R. S. & Higgs, L. A. Atomic hydrogen in a field in Cygnus X containing the supernova remnant G78.2+2.1. *Astronomy and Astrophysics Supplement Series* **39,** 133–151. ISSN: 0365-0138 (Feb. 1980).

137. Gotthelf, E. V. *et al.* Hard X-ray Emission from Sh2-104: A NuSTAR search for Gamma-ray Counterparts. *arXiv:1605.03641 [astro-ph].* <`http://arxiv.org/abs/1605.03641`> (May 2016).

138. Chaves, R. *Galactic VHE gamma-ray astrophysics with H.E.S.S.* in (2015). <`https://www.icrr.u-tokyo.ac.jp/indico/contributionDisplay.py?contribId=151&sessionId=7&confId=23`>.

139. Donath, A. *The Milky-Way observed in TeV gamma-rays with H.E.S.S.* in (2016). <`https://indico.cern.ch/event/469963/contributions/2269479/`>.

140. Halzen, F., Kheirandish, A. & Niro, V. Prospects for Detecting Galactic Sources of Cosmic Neutrinos with IceCube: An Update. *arXiv:1609.03072 [astro-ph, physics:hep-ph].* <`http://arxiv.org/abs/1609.03072`> (Sept. 2016).

141. LIGO Scientific Collaboration and Virgo Collaboration *et al.* Observation of Gravitational Waves from a Binary Black Hole Merger. *Phys. Rev. Lett.* **116,** 061102 (Feb. 2016).

142. De Jager, O. C., Swanepoel, J. W. H. & Raubenheimer, B. C. A powerful test for weak periodic signals with unknown light curve shape in sparse data. *Astronomy and Astrophysics* **221.** <`http://adsabs.harvard.edu/abs/1989A%26A...221..180D`> (Aug. 1989).